OPTICAL, ELECTRICAL AND MORPHOLOGICAL STUDIES OF CONDUCTING ION DOPED METAL OXIDE THIN FILMS

Thesis submitted to the University of Calicut for the partial fulfillment of the requirements for the award of the degree of

Doctor of Philosophy

in

Physics

Under the Faculty of Science

by

JAYA T. P.

Supervisor

Prof. (Dr.) P. P. Pradyumnan

DEPARTMENT OF PHYSICS
UNIVERSITY OF CALICUT
KERALA 673635 - INDIA

July 2017

OPTICAL, ELECTRICAL AND MORPHOLOGICAL STUDIES OF CONDUCTING ION DOPED METAL OXIDE THIN FILMS

Ph. D. thesis in Physics

Author:

Jaya T. P.
Material Science Laboratory
Department of Physics
University of Calicut
Calicut University (P. O.) - 673635, Kerala, India.
Email: jayarijil@gmail.com

Under the guidance of:

Dr. P. P. Pradyumnan
Professor and Head
Department of Physics
University of Calicut
Calicut University (P. O.) - 673635, Kerala, India.
Email : drpradyumnan@gmail.com
: ppp@uoc.ac.in

July 2017

DEPARTMENT OF PHYSICS
UNIVERSITY OF CALICUT
KERALA 673635- INDIA

Prof. (Dr.) P. P. PRADYUMNAN
Professor and Head

Grams: UNICAL
91-0494- 2401144,415,416
Fax- (0494) 2400 269
Mobile: 9895961751
e-mail: drpradyumnan@gmail.com
Kerala, India. 673 635

01st January 2018

CERTIFICATION OF SUPERVISOR

This is to certify that all the corrections/suggestions from the adjudicators have been incorporated in this thesis.

Calicut University **Dr. P. P. Pradyumnan**

DEPARTMENT OF PHYSICS
UNIVERSITY OF CALICUT
KERALA 673635- INDIA

Grams: UNICAL
91-0494- 2401144,415,416
Fax- (0494) 2400 269
Mobile: 9895961751
e-mail: drpradyumnan@gmail.com
Kerala, India. 673 635

Prof. (Dr.) P. P. PRADYUMNAN
Professor and Head

20th July 2017

CERTIFICATE

*Certified that the work presented in this thesis entitled "**Optical, electrical and morphological studies of conducting ion doped metal oxide thin films**" is based on the authentic record of research carried out by **Ms. Jaya T. P.** under my guidance in the Department of Physics, University of Calicut, Calicut University P.O, Kerala – 673635. This work has not been included in any other thesis submitted previously for the award of any degree and has undergone plagiarism check using URKUND Software at CHMK Library, University of Calicut.*

Calicut University **Dr. P. P. Pradyumnan**

Declaration

*Certified that the work presented in this thesis entitled "**Optical, electrical and morphological studies of conducting ion doped metal oxide thin films**" is based on the original research work done by me under the guidance of Dr. P. P. Pradyumnan, Professor and Head, Department of Physics, University of Calicut, Kerala - 673635 and has not been included in any other thesis submitted previously for the award of any degree.*

Calicut University *Jaya T. P.*
20th July 2017

Dedicated to my family......

Acknowledgements

During the tenure of PhD research, I have experienced and learnt quite a lot of things that have really formed me as an individual and helped me expand my scientific knowledge. I would take this opportunity to express my gratitude to all individuals who have contributed to complete this thesis.

First of all, I offer my sincere gratitude to my supervisor and guide, Prof. (Dr.) P. P. Pradyumnan, for his guidance, inspiration and immense moral support during the course of my research. The academic insights and patience, he possesses are invaluable for which I am extremely grateful. I would also wish to thank former heads of the Department of Physics, Prof. George Varghese, Dr. Antony Joseph and Dr. M. M. Musthafa for their help and support during these years. I would also express my gratitude to other faculty members of our department Prof. Vishnu Mayya Bannur, Prof. A M Vinodkumar, Dr. C D Ravikumar, Dr. Shahin Thayyil and Dr. Libu Alexander for their support. Dr. P A Subha, my former teacher and mentor needs special mention for her triggering advices and moral support she had provided during the various phases of my research work. A big thanks also goes to the non-teaching staff of our department for the technical support they have provided.

I express my sincere gratitude to the Head of the Department of Chemistry, University of Calicut for allowing me to perform the analytical characterisations and Mr. Satheesh for carrying out the measurements for my research work. I also thank the Art and photography unit of University of Calicut. I gratefully remember Dr. Renuka of the Department of Chemistry for her suggestions.

The seniors from our lab Dr. T. Ramachandran, Dr. Binitha M.P and Dr. Jayaram P. need special mention. You all have made these years enjoyable and memorable with the conversations and "scientific discussions". Many thanks to some of my other seniors like Dr. Satheesh. B, Dr. A. K. Abdul Gafoor and Dr. Simji P for their support and friendship. My lab mates Mohammed Sabeer and Anju Paulson offered great helps in conducting experiments and supporting me immensely during the time, which I needed the most. Many thanks to my friends and other lab mates Divya, Soumya and Jumana for their personal support.

I would acknowledge UGC-SAP, FIST 2 (DST, Govt. of India) and DST-SERB for the research facilities at the department of Physics, University of Calicut. My sincere thanks to KSCSTE, Women Scientist Division for providing me the project (1015/2013/KSCSTE) and funding for research works, under the Back to Lab scheme. Also,

special thanks to the Indian National Users Program(INUP) at Centre for Nano Science and Engineering (CeNSE), Indian Institute of Science (IISc), Bangalore for the characterisation facilities provided. Mr. Sangeeth and Dr. Smitha Nair needs special mention for their helping nature.

Words fail to express my gratitude to my Amma and Achan for the immense support throughout my life. In spite all their physical inabilities, they have always provided me the path and encouragement to make my endeavour fruitful. I also thank my in-laws for the understanding and support they have shown. My sister, Priya has always been my pillar of strength and offered me all helps whenever I was in need of.

Above all, a special and warm thanks to my husband Dr. Rijil for the immense love, patience, and personal support throughout my research. Without his encouragement and understanding, my dream of a doctorate degree would not have been fulfilled. I owe special love and thanks to my sweet kids Rohan and Raghav, for their patience when I was mostly pre-occupied with research works and thesis writing.

Above all I would like to thank God Almighty for paving the right path and leading me to success after taking up the challenge.

PREFACE

Solar energy, one of the largest sources of energy has the potential to replace all other sources and the main principle behind it is photo voltaics. As a result of concentrated research in this field, silicon and semiconductor based photovoltaic cells have been developed. The optically transparent and simultaneously electrically conducting nature of transparent conductors make them significant components in solar cells. They are also applied in other contemporary devices such as smart windows, LCD displays, heat reflecting mirrors, anti-static coatings and electromagnetic shields, to name a few.

The fabrication and application of transparent conducting oxides (TCOs) in the field of optoelectronics has become increasingly significant over the past few years due to the highly specific functional properties they possess. Significant transparency together with a reduction in resistivity can be accomplished in thin metallic films. By introducing electron degeneracy in wide band gap materials ($E_g > 3eV$ or more) these properties can be enhanced. This can be done by controllably incorporating non-stoichiometry in the crystal lattice. A large number of techniques are used for fabricating TCO thin films and optimizing film growth features. The thermodynamic parameters have crucial influence on growth features and slight variations can result in films with different physical properties. Thermodynamic parameters include substrate temperature, distance of reacting species from the substrate, oxygen partial pressures inside the chamber during growth of these films, sputter power, nature of target etc.

The number of materials belonging to the category of TCO phase space is mounting up very fast. Earlier only *n*-type materials were in use, but recent research has resulted in *p*-type TCOs with good performance as well. This has led to the practical realization of circuits that are optically transparent, simultaneously maintaining electrical conductivity. This investigation covers the fabrication, characterization and property studies of *n*-type and *p*-type transparent conducting oxides - tin oxide and copper oxide respectively, in the TCO phase space. The

incorporation of III group element indium into these materials and their property variations have been investigated in detail. Optimisation of the fabrication conditions of these materials using radio frequency magnetron sputtering method have been discussed in detail. This thesis consists of seven chapters - a brief sketch of the contents is as follows.

Chapter 1 contains a detailed discussion of prior literatures available on TCOs and a general introduction to this field, along with the unique opto-electronic properties of TCOs. The various kinds of TCOs in use and their major applications are included, along with the specific objectives of this work. The various thin film deposition techniques and the reason for selecting a sole method of fabrication suitable for a definite application are explained in Chapter 2. The functional details and thermodynamic parameters of radio frequency magnetron sputtering, used in this investigation are discussed thoroughly.

Chapter 3 comprises of thin film properties and characterisation tools used for the studies of the grown films. Various conventional and advanced techniques were utilised for the structural, optical, electrical and morphological investigations of the films. A brief discussion of the equipments used is also given. The working chapters with a report of the original investigation and its outcome commences with chapter 4. This includes the fabrication and studies on *n*-type SnO_2 thin films in the first section and indium tin oxide (ITO) in the second. The influence of various parameters like sputter power, nature of target and substrate, target to substrate distance and substrate temperature on the growth and yield of sputtering have been investigated.

The production and investigation of *p*-type conducting TCOs – copper (II) oxide and copper indium oxide are specified in Chapter 5. Structural studies were conducted based on XRD and XPS results. Surface morphological analysis of the films was conducted using SEM, AFM and optical profilometry. From the UV-Visible spectral studies, the electronic transitions were determined and the band gap of materials computed. TEM images give a clear illustration of the morphology of the grains. The concentration of charge carriers, their mobility and resistivity values

of the films were found using Vander Paw method from Hall measurements of the films. The influence of sputter power and substrate temperature on the electrical, optical and morphological properties of the *p*-type TCOs are examined in this chapter. To study the effect of target nature on the growth of CuO thin films, two different targets were used: one using copper metal target under oxygen ambience and another using CuO powder target under non-oxygen environment.

Chapter 6 illustrates the fabrication of all transparent *p-n* hetero junction diodes at various sputter powers and substrate temperatures and optimisation of their growth parameters. The current-voltage characteristics obtained using DC probe station under visible light showed a low turn-on voltage of the hetero junction diodes, less than one volt. The diodes exhibited rectifying nature and a high value for ideality factors was obtained. Finally, chapter 7 provides a general conclusion of the whole research along with recommendations for further works on this topic.

List of Publications

1. Jaya T. P., P. P. Pradyumnan, "Surface features and optical properties of RF sputtered and reactively sputtered CuO thin films", *Thin solid films* (Under review).
2. Jaya T. P., P. P. Pradyumnan, "Plasma vapour deposited Ag/n-ITO/p-CIO hetero junctions for optoelectronic device applications", *Japanese Journal of Applied Physics*, 56 (2017) 125502.
3. Jaya T. P., P. P. Pradyumnan, "High transmittance hetero junctions based on n-ITO/*p*-CuO bilayer thin films", *Materials Research Express,* (IOP), 6 (2016) 126401.
4. Jaya T. P., P. P. Pradyumnan, "Micro structural and dielectric property analysis on hydrothermally grown gadolinium doped SnO_2 crystals", *Materials Research Express,* (IOP), 6 (2016) 095905.
5. Jaya T. P., Divya N. K., P. P. Pradyumnan, "Effect of surfactants on the morphological and optical properties of ZTO ceramics", *Journal of Nanoscience and Nanotechnology*, 2 (2014) 442-444.
6. Divya N. K., Jaya T. P., P. P. Pradyumnan, "Variation in morphology and crystallinity of ZTO ceramics", *Research Journal of Recent Sciences*, 3 (2014) 71-74.
7. Divya N. K., Jaya T. P., P. P. Pradyumnan, "UV attenuation characteristics of tin and titanium doped ZnO ceramics", *Journal of Nanoscience and Nanotechnology*, 2 (2014) 445-447.
8. Jaya T. P., P. P. Pradyumnan, "Phase Investigation of Micro Crystals of ZTO", *International Journal of Chem. Tech. Research*, 6 (2014) 3259-3261.
9. Jayaram P, Jaya T. P., S. Z. Karazhanov, P. P. Pradyumnan, "Structural and Physical Property Analysis of $ZnO–SnO_2–In_2O_3–Ga_2O_3$ quaternary Transparent Conducting Oxide System", *Journal of Materials Science and Technology,* 29, 5(2013) 419-422.
10. Jayaram P, Jaya T. P., P. P. Pradyumnan, " Bulk Synthesis and Structural Determination of High Mobility Multication Transparent Conducting Oxides", *Solid State Phenomena*, 194 (2013) 124-128.

Papers presented in International/ National Conferences

1. *Solution based synthesis and comparative study of pure and doped ZnO nano crystals,* Workshop on Research in Advanced Material Synthesis held at Payyannur College, Kannur during 24-25 June 2013.
2. *Inverse Spinel Grown Zn_2SnO_4 Based Multication Transparent Conducting oxides by PLD,* International Conference on Nanomaterials for Frontier Applications and Indo-Norwegian Workshop on Advanced Materials for Solar Cell Applications, ICNFA-2013 at Coimbatore Institute of Technology, Coimbatore.
3. *Studies on the dense grown crystalline ternary cubic spinel In^{3+} substituted n-type Zn_2SnO_4 TCO thin films,* INDO-US Workshop on Nano-Structure Electronic Materials, IUSWNM- 2013, at Thrissur, India.
4. *UV absorption of Zinc stannate ceramics: Variation with reaction media,* International Science Congress, Karunya University, Coimbatore during 8-9th December 2013.
5. *Impact of pH on the morphology and crystalline nature of zinc stannate nano particles,* Kerala Science Congress at Vythiri, Wynad during 28th to 31st January 2014.
6. *Effect of surfactant on the morphological and optical properties of ZTO ceramics,* International Conference on Nano Electronic Science and Technology, ICNEST 2014 held during 14-15th February 2014 at Sri Vasavi Institutions, Erode, Tamil Nadu.
7. *Phase Investigation of Micro Crystals of ZTO,* International Conference on Materials and Characterisation techniques, ICMCT 2014 held during 10-12th March 2014 at Vellore Institute of Technology, Vellore.
8. *Conducting Transparent Casseterite thin films by RFM Sputtering for Smart Window Applications,* International Conference on Sustainable Energy Technologies, ICSET 2014 held during 11-13th December 2014 at PSG Tech Institution, Coimbatore.

9. *Radio frequency magnetron sputtered casseterite thin films : Surface studies for display applications,* 9th International Conference on Computational Physics, ICCP9, held during 7-11th January 2015 at National University of Singapore, Kent Ridge, **Singapore.**

10. *Transparent p-n hetero junctions for opto electronic applications,* 8th International Conference on Materials for Advanced Technologies of the Materials Research Society of Singapore, ICMAT2015 & IUMRS-ICA2015, 28 June to 03 July, 2015 in **Singapore** held at Suntec Singapore Convention Centre.
11. *Transparent optoelectronic materials*, National Conference on Materials Science held at Govt. Pookoya Thangal memorial college, Perinthalmanna on 12th and 13th October 2015.
12. *Variation of UV absorption of Sn:ZnO ceramics with reaction media,* UGC Sponsored National Conference on Modern Optics & Material Science (NCMOMS-2015) during December 17-18, 2015 at Post Graduate Department of Physics & Research Center Farook College, Kozhikode.
13. *Theoretical prediction of optical constants: Comparison with experimental values of sputtered ITO thin films,* 28th Kerala Science Congress held during January 2016 at University of Calicut, Kerala.
14. *Structural and optical property variations of ZTO ceramics with medium of crystal growth*, International Conference on Materials Science & Technology ICM Tech 2016 during 1-4th March 2016 at University of Delhi.
15. *Core-level XPS spectra and elemental analysis on sputter deposited CuO and In:CuO thin films,* 2017 EMN Optoelectronics Meeting, At Victoria BC, Canada during April 2017.

Achievements / Recognitions

1. KSCSTE awarded a research project (1015/2013/KSCSTE) entitled "Studies on multi component transparent conducting oxide thin films for device applications" for a total amount of 15.96 Lakhs. The project was successfully completed on 11-12-2016.

Contents

Chapter 1. An introduction to Transparent Conducting Oxides

1.1 Introduction........ 2
1.2 Electrical Conductivity........ 4
1.3 Optical Transparency........ 6
1.4 Simultaneous occurrence of electrical conductivity and optical transparency........ 7
1.5 Other characteristics of TCOs........ 10
1.6 Different types of TCOs........ 10
1.7 Applications of TCOs........ 12
1.8 Specific objectives of this work........ 15
References........ 17

Chapter 2. Thin film deposition techniques

2.1 Introduction 24
2.2 Chemical methods of thin film deposition........ 24
2.2.1 Spray Pyrolysis........ 25
2.2.2 Dip coating........ 25
2.2.3 Spin coating........ 26
2.2.4 Chemical Vapour Deposition........ 27
2.3 Physical methods of thin film deposition........ 27
2.3.1 Vacuum Evaporation........ 27
2.3.2 Electron beam evaporation........ 28
2.3.3 Molecular beam epitaxy........ 28
2.3.4 Pulsed laser deposition........ 29
2.3.5 Sputtering........ 29
2.3.5.1 DC sputtering........ 30
2.3.5.2 RF sputtering........ 31
2.3.5.3 Reactive sputtering........ 32

2.3.5.4 Yield of sputter deposition.. 32
2.4 Criteria for selection of a particular deposition technique.......................... 33
References.. 36

Chapter 3. Characterisation techniques

3.1 Structural analysis... 40
3.1.1 X-ray diffraction... 40
3.1.2 Transmission Electron Microscopy... 42
3.2 Spectroscopic analysis.. 44
3.2.1 X-ray photoelectron spectroscopy.. 44
3.2.2 UV-Visible spectroscopy... 46
3.2.3 Energy dispersive spectroscopy... 49
3.3 Surface morphology analysis.. 51
3.3.1 Scanning electron microscopy... 51
3.3.2 Atomic force microscopy.. 53
3.3.3 Optical profilometry.. 55
3.4 Electrical property analysis.. 56
3.4.1 Hall effect.. 56
3.4.2 I-V characteristics... 59
References.. 62

Chapter 4. Studies on n-type transparent conducting oxides

4.1 Introduction.. 65
4.2 Fabrication of thin films by radio frequency magnetron sputtering.......... 65
4.3 Growth kinetics... 66
4.3.1 Effect of sputter power... 66
4.3.2 Effect of substrates... 66
4.3.3 Effect of nature of target.. 67
4.3.4 Effect of substrate to target distance... 68
4.3.5 Effect of substrate temperature during sputtering....................... 69

4.4 Tin (IV) oxide.. 69

4.4.1 Electronic structure and transparent conducting properties......... 70

4.5 Results and discussion.. 71

4.5.1 X-ray diffraction... 72

4.5.2 Scanning electron microscopy.. 76

4.5.3 Energy dispersive spectra... 78

4.5.4 Atomic force microscopy.. 79

4.5.5 Transmission electron microscopy... 83

4.5.6 Optical profilometry.. 84

4.5.7 Hall measurements.. 85

4.5.8 UV-Visible spectroscopy.. 87

4.5.9 X-ray photoelectron spectroscopy.. 92

4.5.10 Optical transparency of the film... 96

4.6 Indium tin oxide (ITO) 96

4.6.1 Electronic structure and transparent conducting properties......... 97

4.7 Results and discussions.. 98

4.7.1 X-ray diffraction... 99

4.7.2 Scanning electron microscopy.. 101

4.7.3 Energy dispersive spectra... 102

4.7.4 Atomic force microscopy.. 103

4.7.5 Transmission electron microscopy... 105

4.7.6 Optical profilometry.. 106

4.7.7 Hall measurements.. 107

4.7.8 UV-Visible spectroscopy.. 108

4.7.9 X-ray photoelectron spectroscopy.. 110

4.7.10 Optical transparency of the film... 113

4.8 Conclusions.................................... 114

References.................................... 115

Chapter 5. Studies on p-type transparent conducting oxides

5.1 Introduction.................................... 118

5.2 Copper oxide.. 119
5.2.1 Electronic structure and transparent conducting properties......... 120
5.3 Results and discussion.. 121
5.3.1 X-ray diffraction.. 122
5.3.2 Scanning electron microscopy.. 124
5.3.3 Energy dispersive spectra.. 126
5.3.4 Atomic force microscopy... 127
5.3.5 Transmission electron microscopy... 130
5.3.6 Optical profilometry.. 131
5.3.7 Hall measurements... 133
5.3.8 UV-Visible spectroscopy... 137
5.3.9 X-ray photoelectron spectroscopy.. 139
5.3.10 Optical transparency of the film.. 142
5.4 Copper Indium oxide (CIO) 143
5.4.1 Electronic structure and transparent conducting properties........... 143
5.5 Results and discussion 145
5.5.1 X-ray diffraction.. 146
5.5.2 Scanning electron microscopy.. 146
5.5.3 Atomic force microscopy... 148
5.5.4 Optical profilometry.. 149
5.5.5 Hall measurements... 150
5.5.6 UV-Visible spectroscopy... 152
5.5.7 X-ray photoelectron spectroscopy.. 153
5.5.8 Optical transparency of the film.. 155
5.6 Conclusions.................................... 156
References..................................... 157

Chapter 6. Fabrication of thin film hetero junctions

6.1 Introduction.................................... 160
6.2 Growth of *p-n* junctions by RFM sputtering... 161

6.3 Transparent *n*-ITO/ *p*-CuO hetero junctions... 162

6.3.1 I - V Characteristics... 162

6.3.2 Ideality factor..................................... 165

6.4 Transparent *n*-ITO/ *p*-CIO hetero junctions.. 166

6.4.1 I - V Characteristics... 166

6.4.2 Ideality factor... 167

6.5 Conclusions..................................... 169

References..................................... 170

Chapter 7. Summary and Conclusions

7.1 Summary and Conclusions.. 172

7.1.1 Investigation of processing parameters on electrical, optical, micro structural and structural properties of *n*-type and *p*-type materials.. 172

7.1.2 Fabrication of transparent *p-n* hetero junctions based on these films and investigation of their physical properties for device applications.. 173

7.2 Scope for future studies.. 174

References..................................... 175

List of Figures

1.1 Energy band diagram showing the Burstein-Moss shift in semiconductors 6

1.2 Spectral dependence of TCOs 7

1.3 Schematic diagram showing valence and conduction band in TCOs 8

1.4 Schematic diagram of the assembly of a smart window 12

1.5 Schematic of a touch sensor 14

1.6 Schematic of an LCD display unit 14

2.1 Schematic diagram of RF magnetron sputtering system 31

2.2 Radio frequency magnetron sputtering set up. 35

3.1 (a) Schematic illustration of diffraction process and (b) Internal view of the X-ray diffractometer 41

3.2 Schematic diagram of the electron path in a TEM 43

3.3 Schematic diagram of the photo electron emission process 45

3.4 Schematic diagram of UV-Visible spectrophotometer 47

3.5 Schematic of Energy Dispersive Spectrometer 50

3.6 Schematic diagram of the electron path in a scanning electron microscope 52

3.7 (a) Schematic diagram of atomic force microscope unit and (b) Photograph of AFM equipment........ 54

3.8 Schematic representation of a non-contact optical profilometer 55

3.9 Van der Pauw Hall measurement sample 57

3.10 Schematic diagram of Hall measurement set up........ 58

3.11 Schematic energy diagram of *p*-type and *n*-type semiconductors before junction formation (left) and of the *p–n* junction (right) 60

3.12 Schematic of thin film *p-n* junction diode........ 61

4.1 Crystal structure of SnO_2 70

4.2 Yield of sputtering of SnO_2 thin films 72

4.3 XRD pattern of SnO_2 films sputtered at substrate temperature of 150^0C . 73

4.4 XRD pattern of SnO_2 films sputtered at 120W 74

4.5 Crystallite size variations with substrate temperature and sputter power of SnO_2 thin films 76

4.6 SEM images of SnO_2 films sputtered at substrate temperature of 150^0C and sputter power (a) 60 W, (b) 100 W, (c) 120 W, (d) 140 W and (e) 200 W.................... 77

4.7 SEM images of SnO_2 films sputtered at sputter power of 120 W and substrate temperature of (a) 25^0C, (b) 100^0C, (c) 150^0C, (d) 200^0C. 77

4.8 EDS spectra of the samples 78

4.9 2D and 3D AFM images of SnO_2 films at sputter powers of (a) 60 W, (b) 100 W, (c) 120 W, (d) 140 W and (e) 200 W 80

4.10 2D and 3D AFM images of SnO_2 films at substrate temperature of (a) 25^0C, (b) 100^0C, (c) 150^0C, (d) 200^0C 81

4.11 TEM images at (a) low resolution, (b) high resolution and (c) SAED pattern of SnO_2 films sputtered at 150^0C and 120W 83

4.12 Optical profile of the SnO_2 film sputtered at 150^0C and 120W.................... 84

4.13 Variation of carrier concentration with (a) sputter power and (b) substrate temperature 86

4.14 Variation of charge carrier mobility with (a) sputter power and (b) substrate temperature 86

4.15 Variation of thin film resistivity with (a) sputter power and (b) substrate temperature 87

4.16 Optical transmission spectra of SnO_2 films at different sputter powers ... 88

4.17 Optical transmission spectra of SnO_2 films at different substrate temperatures 88

4.18 a Tauc plot of SnO_2 films at different sputter powers 89

b Tauc plot of SnO_2 films at different substrate temperatures.................. 90

4.19 Correlation of charge carrier density and optical band gap with (a) sputter power and (b) substrate temperature 91

4.20 Carbon 1s spectra for XPS calibration of SnO_2 spectra 93

4.21 Narrow scan analysis of tin in sputtered SnO_2 films 94

4.22 Narrow scan analysis of oxygen in sputtered SnO_2 films 95

4.23 Survey scan spectrum of SnO_2 films 95

4.24 Actual photograph of SnO_2 films sputtered at 150^0C and 120W 96

4.25 Crystal structure of ITO 98

4.26 Yield of sputtering of ITO thin films 99

4.27 XRD pattern of ITO films 100

4.28 SEM images of ITO films sputtered at powers (a) 60W, (b) 100W, (c) 120W, (d) 140W and (e) 200W 101

4.29 EDS spectra of ITO film grown at 100^0C and 120W 102

4.30 2D and 3D AFM images of ITO films at sputtered at (a) 60 W, (b) 100 W, (c) 120 W, (d) 140 W and (e) 200 W 103

4.31 TEM images at (a) low resolution, (b) high resolution and (c) SAED pattern of ITO films sputtered at 100^0C and 120 W 105

4.32 (a) 2D Optical profile, (b) 3D Optical profile and (c) line profile of the ITO film sputtered at 100^0C and 120 W 106

4.33 Variation of resistivity and carrier concentration with sputter power 108

4.34 Optical transmission spectra of ITO films at different sputter powers 108

4.35 Tauc plot of ITO films at different sputter powers 110

4.36 Carbon 1s spectra for XPS calibration of ITO spectra 111

4.37 Narrow scan analysis of indium in sputtered ITO films 111

4.38 Narrow scan analysis of tin in sputtered ITO films 112

4.39 Narrow scan analysis of oxygen in sputtered ITO films 112

4.40 Survey scan spectrum of ITO films 113

4.41 Actual photograph of ITO films sputtered at 100^0C and 120W 113

5.1 Crystal structure of CuO and Cu_2O 119

5.2 Yield of sputtering of CuO thin films... 121

5.3 XRD pattern of CuO films with varying (a) sputter power and (b) substrate temperature using oxide target 122

5.4 XRD pattern of CuO films with varying (a) sputter power and (b)substrate temperature using metallic target 123

5.5 SEM images of CuO films sputtered using oxide target at powers (a) 60W, (b) 100W, (c) 140W and (d) 200W.. 124

5.6 SEM images of CuO films sputtered using oxide target at substrate temperatures (a) 25^0C (b) 100^0C (c) 150^0C and (d) 200^0C 125

5.7 SEM images of CuO films sputtered using metallic target at powers (a) 60W, (b) 100W, (c) 140W and (d) 200W 125

5.8 SEM images of CuO films sputtered using metallic target at substrate temperatures (a) 25^0C (b) 100^0C (c) 150^0C and (d) 200^0C 126

5.9 EDS spectra of the thin films sputtered using (a) oxide target and (b) metallic target 127

5.10 2D and 3D AFM images of CuO films using oxide target at powers (a) 60W, (b) 100W, (c) 140W and (d) 200W 128

5.11 2D and 3D AFM images of CuO films using metallic target at (a) 60W, (b) 100W, (c) 140W and (d) 200W 129

5.12 TEM images at (a) low resolution, (b) and (c) high resolution and (d) SAED pattern of CuO films 131

5.13 (a) 2D Optical profile, (b) 3D Optical profile and (c) line profile of CuO film sputtered at 150^0C and 140W using metallic target 132

5.14	(a) 2D Optical profile, (b) 3D Optical profile and (c) line profile of CuO film sputtered at 150^0C and 140W using oxide target	132
5.15	Variation of (a) carrier concentration and resistivity and (b) mobility of films sputtered using oxide target with sputter power...............................	134
5.16	Variation of (a) carrier concentration and resistivity and (b) mobility of films sputtered using oxide target with substrate temperature..................	135
5.17	Variation of (a) carrier concentration and resistivity and (b) mobility of films sputtered using metallic target with sputter power...........................	136
5.18	Variation of (a) carrier concentration and resistivity and (b) mobility of films sputtered using metallic target with substrate temperature...............	136
5.19	Optical transmission spectra of CuO films at different (a) sputter powers and (b) substrate temperatures using oxide target	137
5.20	Optical transmission spectra of CuO films at different (a) sputter powers and (b) substrate temperatures using metallic target	138
5.21	Carbon 1s spectra for XPS calibration of CuO spectra	140
5.22	Survey scan spectrum of CuO films	140
5.23	Narrow scan analysis of copper in sputtered CuO films	141
5.24	Narrow scan analysis of oxygen in sputtered CuO films	141
5.25	Actual photograph of CuO films sputtered at 150^0C and 140W using (a) oxide target and (b) metal target	143
5.26	Crystal structure of Copper Indium Oxide	144
5.27	Yield of sputtering of CIO thin films	145
5.28	XRD pattern of CIO films with varying (a) sputter power and (b) substrate temperature	146
5.29	SEM images of CIO films at powers (a) 60W, (b) 100W, (c) 150W and (d) 200W	147

5.30 SEM images of CIO films at substrate temperatures (a) 25^0C (b) 100^0C (c) 150^0C and (d) 200^0C 147

5.31 2D and 3D AFM images of CIO films at powers (a) 60W, (b) 100W, (c) 150W and (d) 200W 148

5.32 a) 2D Optical profile, (b) 3D Optical profile and (c) line profile of CIO film sputtered at 100^0C and 150W 149

5.33 Variation of (a) carrier concentration and resistivity and (b) mobility of films with sputter power........ 151

5.34 Variation of (a) carrier concentration and resistivity and (b) mobility of films with substrate temperature........ 151

5.35 Optical transmission spectra of CIO films at different (a) sputter powers and (b) substrate temperatures 152

5.36 Narrow scan analysis of copper in sputtered CIO films 154

5.37 Narrow scan analysis of indium in sputtered CIO films 154

5.38 Narrow scan analysis of oxygen in sputtered CIO films 155

5.39 Survey scan spectrum of CIO films 155

5.40 Actual photograph of CIO films 156

6.1 Schematic diagram of the transparent *p*-*n* hetero junction 161

6.2 Equilibrium energy band diagram of the *n*-ITO/*p*-CuO hetero junction diode fabricated by RF sputtering 163

6.3 Typical current-voltage plots of the ITO/CuO transparent hetero junctions 164

6.4 *ln* I vs Voltage graph of the hetero junction diodes with *p*-CuO layer sputtered at (a) 200 W and 100^0C and (b) 150 W and 200^0C 165

6.5 Equilibrium energy band diagram of the *n*-ITO/*p*-CIO hetero junction diode fabricated by RF sputtering 166

6.6 Typical current-voltage plots of the ITO/CIO transparent hetero junctions with (a) varying sputter powers and (b) varying substrate temperatures 167

6.7 *ln* I Vs Voltage graph of the hetero junction diodes (a) for varying sputter powers and (b) substrate temperatures 168

List of Tables

1.1 Chronological list of some of the major results in the field of transparent conductors 4

4.1 Experimental parameters of sputtering process........ 72

4.2 Peak shift of XRD pattern 74

4.3 Crystallite size variations of SnO_2 films with sputter power 75

4.4 Crystallite size variations of SnO_2 films with substrate temperature 75

4.5 Variation of RMS roughness with sputter power 82

4.6 Variation of RMS roughness with substrate temperature 82

4.7 Comparison of d-spacing from TEM and XRD........ 84

4.8 Variation of electrical characteristics of SnO_2 films with sputter power . 85

4.9 Variation of electrical characteristics of SnO_2 films with substrate temperature........ 85

4.10 Variation of band gap energy with sputter power 90

4.11 Variation of band gap energy with substrate temperature 91

4.12 Thickness variation with sputter power of SnO_2 films 92

4.13 Thickness variation with substrate temperature of SnO_2 films 92

4.14 Experimental parameters of sputtering process 99

4.15 Crystallite size variations of ITO films with sputter power 100

4.16 Variation of RMS roughness with sputter power 104

4.17 Comparison of d-spacing from TEM and XRD........ 106

4.18 Electrical characteristics variation of ITO films with sputter power 107

4.19 Variation of band gap energy with sputter power 109

4.20 Thickness variation with sputter power of ITO films 109

5.1 Experimental parameter details used for sputtering process........ 122

5.2 RMS roughness variations of films sputtered using oxide target with (a) sputter power and (b) substrate temperature 130

5.3 RMS roughness variations of films sputtered using metalic target with (a) sputter power and (b) substrate temperature 130

5.4 Comparison of d-spacing from TEM and XRD 131

5.5 Variations of electrical characteristics with sputter power for the films sputtered using oxide target 133

5.6 Variations of electrical characteristics with substrate temperature for the films sputtered using oxide target 134

5.7 Variations of electrical characteristics with sputter power for the films sputtered using metal target 135

5.8 Variations of electrical characteristics with substrate temperature for the films sputtered using oxide target 136

5.9 Variation in band gap with (a) sputter power and (b) substrate temperature for oxide target 138

5.10 Variation in band gap with (a) sputter power and (b) substrate temperature for metal target 139

5.11 Experimental parameter details used for sputtering process 145

5.12 RMS roughness variations of CIO films with sputter power 149

5.13 Variation of electrical properties with (a) sputter power and (b) substrate temperature... 150

5.14 Variation in band gap with (a) sputter power and (b) substrate temperature for metallic target 153

6.1 Electrical property variations of *p-n* hetero junctions 168

List of Abbreviations

AFM	:	Atomic Force Microscope/Microscopy
B-M-effect	:	Burstein Moss effect
CIO	:	Copper Indium oxide
CVD	:	Chemical Vapour Deposition
EDS	:	Energy Dispersive spectroscopy
FWHM	:	Full Width at Half Maximum
ICDD	:	International Centre for Diffraction Data
ITO	:	Indium tin oxide
MBE	:	Molecular Beam Epitaxy
MOCVD	:	Metal Organic Chemical Vapor Deposition
NIST	:	National Institute of Standards and Technology
OLEDs	:	Organic Light Emitting Diodes
PDXL	:	Integrated X-ray Powder Diffraction Software
PLD	:	Pulsed Laser Deposition
RMS	:	Root mean square
SEM	:	Scanning Electron Microscopy
TC	:	Transparent conductor
TCO	:	Transparent Conducting Oxide
TEM	:	Transmission Electron Microscopy
TTFT	:	Transparent Thin Film Transistors
XPS	:	X ray photoelectron spectroscopy
XRD	:	X-Ray Diffraction
UV	:	Ultra violet

CHAPTER 1

AN INTRODUCTION TO TRANSPARENT CONDUCTING OXIDES

1.1 Introduction

Transparent conducting oxides (TCOs) belong to a unique category of materials that achieve high value of electrical conductivity, simultaneously retaining a high transmittance of visible range of the electromagnetic spectrum. For high-efficiency optoelectronic devices, electrical contacts with high electrical conductivity are inevitable with the top contact having high optical transparency and this requirement is met by TCOs. TCOs are being synthesised and technically applied initially as oxides with single-cation such as binary oxides and recently, as multi-cation oxides [1–6]. Currently, the fundamental understanding of structural and physical behaviour of these highly important class of materials are being investigated and new TCO phases are being discovered by researchers.

The first transparent and conducting material synthesised was reported in 1907 by K. Badeker [7]. He coated a thin layer of cadmium by sputtering and annealed it in air. He found that the material coated on the interior walls of the glow discharge tube, formed as a result of oxidation of cadmium, was electrically conducting as well as optically transparent. The incompatibility of optical transparency with electrical conductivity is the significant matter of research in the field of transparent conductors. The simultaneous occurrence of these two properties in the same material is conflicting, from band structure viewpoint. A transparent material will usually be an insulator with completely occupied valence band and unoccupied conduction band; whereas conductivity occurs when high carrier concentration is provided by the Fermi level lying within an energy band having large density of states. These desirable properties are attained in several oxides in their pristine form- indium (III) oxide (In_2O_3), tin (IV) oxide (SnO_2), zinc (II) oxide (ZnO) and cadmium (IV) oxide (CdO).

TCOs have been prepared from a wide variety of materials. Metal oxides are considered as better candidates for transparent conductors because of their better stability at all temperatures, cost effectiveness and improved opto-electronic characteristics. Oxides of zinc, tin, cadmium, indium and gallium are generally established as architectural constituents of transparent conducting electrodes when

mixed together or doped with other metal oxides. Currently, the materials in wide use are tin doped indium oxide - In_2O_3:Sn (known as ITO), fluorine doped tin oxide - SnO_2:F (known as FTO), aluminum doped zinc oxide - ZnO:Al (known as AZO) etc [8-10]. Recently, binary cation materials like $CdSnO_3$, $ZnSnO_3$, Zn_2SnO_4 [11-13] and ternary cation TCOs like $InGaO_3(ZnO)_5$, $InGaZnO_4$ [14,15] also are in use, which exhibit *n*-type electrical conductivity. These materials use defect energy levels created by extrinsic dopants to produce *n*-type conductivity.

Band gap of a material has significant role in its light absorption property. In the pristine state, they exist as insulators with an optical band gap of about 3 eV. In order to make them good TCOs, these materials can be doped degenerately, so that the Fermi level is displaced up into the conduction band. A highly dispersed single free electron-like conduction band is the unique trait of any conventional *n*-type TCO [16–19]. Kawazoe et. al. [20] proposed novel *p*-type transparent conductors with delaffosite structure for the potential application in optoelectronic industry. Based on that, recently $CuAlO_2$, $SrCu_2O_2$ and *p*-type ZnO are also developed [21-23, 61]. The family of transparent conductors also includes metal and carbon nano-composites, graphene and polymer based materials.

ITO was the first of the modern TCO materials, discovered in 1954 by Rupperecht; but this had significant shortcomings due to the high price and rarity of indium and also the decay of films at higher temperatures, which is required for certain device processing. These drawbacks have led to the development of other materials such as fluorine doped tin oxide, antimony doped tin oxide, and lately, doped zinc and cadmium oxides with higher performance, durability and lower cost [24-27]. When these oxides are degenerately doped, it enhances the mobility of charge carriers owing to their small effective masses and promotes lesser absorption of visible radiation caused by the low density of states within conduction band. The higher energy distribution of the conduction band also causes significant displacement of Fermi energy beyond the minimum of conduction band, known as the Burstein – Moss (BM) shift as discussed later in this chapter [28-30]. Table 1.1 gives a chronological list of major milestones in the field of transparent conductors. Although it is not a complete list of all discoveries, we can observe the massive

research work going on in this field, both in the nature of materials and the synthesis methods.

Table 1.1 Chronological list of some of the major results in the field of transparent conductors.

Material	Year	Synthesis method	Reference
CdO	1907	Thermal oxidation	[7]
SnO_2: Cl	1947	Spray Pyrolysis	[31]
SnO_2:Sb	1947	Spray Pyrolysis	[32]
In_2O_3: Sn	1951	Spray Pyrolysis	[33]
CdO	1952	Sputtering	[34]
In_2O_3: Sn	1955	Sputtering	[35]
In_2O_3: Sn	1966	Spray Pyrolysis	[36]
SnO_2:Sb	1967	Chemical Vapour Deposition	[37]
Cd_2SnO_4	1972	Sputtering	[38]
Zn_2SnO_4	1992	Sputtering	[39]
$ZnSnO_3$	1994	Sputtering	[40]
InGaZnO	2001	Pulsed Laser Deposition	[41]
ZnSnO	2004	Sputtering	[42]
SnO_2	2009	Sputtering	[43]
CuO	2013	Sputtering	[44]

1.2 Electrical Conductivity

The high electrical conductivity of transparent conductor is mainly due to deviations from stoichiometry and oxygen vacancies. Donor sites associated with excess metal ions and oxygen vacancies provide the conduction electrons [30]. Carrier mobility is one of the major factors directing the conductivity of TCO films, which in turn depends on scattering of charge carriers due to imperfections in lattice structure. In semiconducting films, the predominant scattering mechanisms are piezo

electric scattering, optical phonon scattering, deformation potential scattering, neutral impurity scattering, electron-electron scattering, ionized impurity scattering and grain boundary scattering [29].

The electrical conductivity of semiconductors is less than that of metals ($<10^4\ \Omega^{-1}cm^{-1}$) and higher than that of an insulators ($>10^{-10}\ \Omega^{-1}cm^{-1}$) and has an energy gap < 4.1 eV. At absolute temperature the conduction band of semiconductors is completely empty and the valence band is completely filled and hence, no conduction is possible. As temperature increases, electrons at the top of the valence band gets thermally excited and reach the bottom of conduction band, creating empty states in the valence band. The conduction is mainly *n*-type and the predominant charge carriers are electrons.

The Burstein–Moss shift is of prime importance in TCOs, by which the apparent band gap of a semiconductor becomes larger. The optical absorption edge is shifted to higher energies, on account of all states close to conduction band being occupied. It is typically observed for a degenerate electron distribution and takes place when the carrier concentration of *n*-type carriers exceeds the conduction band edge density of states.

The emission spectrum of a semiconductor is tailored by this effect, resulting in phenomena such as band gap variation and occupation of the near band gap states. The Fermi level of moderately doped semiconductors lies between conduction and valence bands. As concentration of doping is increased, the electrons occupy conduction band states, pushing the Fermi level to higher energy [45].

The Fermi level of degenerately doped semiconductors, lie inside the conduction band and hence, an electron from the top of the valence band can be energized only into conduction band above the Fermi level, since all states below Fermi level are unavailable. This increases the energy of the lowest optical transition, the optical gap. The excitation into such occupied states is forbidden according to Pauli's exclusion principle. The band gap thus created is regarded as 'apparent band gap', as shown in figure 1.1, and can be calculated using transmission/reflection spectroscopy.

Apparent band gap = Actual band gap + Burstein–Moss shift...............(1.1)

This effect generally results in a blue shift of the absorption edge and varies with effective mass of particles and is made use of in laser applications [46].

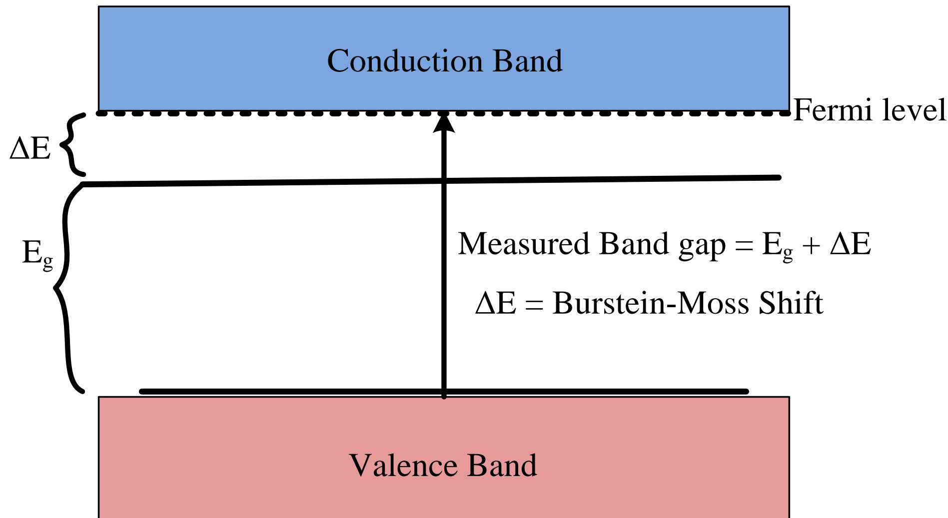

Figure 1.1 Energy band diagram showing the Burstein-Moss shift in semiconductors.

1.3 Optical transparency

The fundamental optical properties of a sample are generally described by transmission, reflection, and absorption of light with respect to a particular wavelength. Energy is conserved when incident light falls on a sample and get partially transmitted, reflected and/or absorbed.

$$T + R + A = 1 \text{ ....(1.2)}$$

where the values of T, R, and A are measured as the fraction of incident light that is either transmitted, reflected or absorbed respectively.

The optical phenomena of TCOs can be described using Drude's theory of free electrons in metals [45]. When these electrons come within an electromagnetic field, it results in the polarisation of field inside the material, which influences the relative permittivity. Electromagnetic waves are incapable of propagating in a negative dielectric constant medium, since the wave decays exponentially and wave

vector is imaginary. In such a medium, the incident waves get totally reflected. The plasma frequency or cut off frequency of electromagnetic transmission is given by the relation,

$$\omega_p = \sqrt{\frac{4n\pi e^2}{m}} \dots\dots\dots\dots\dots..(1.3)$$

At frequencies greater than plasma frequency, the material behaves as a transparent dielectric, and at lesser frequency, TCO reflects incident radiation. That is, for wavelengths longer than plasma wavelength λ_p, as in figure 1.2, the incident radiation gets reflected and for shorter wavelengths, up to λ_{gap}, TCO transmits incident radiation [47].

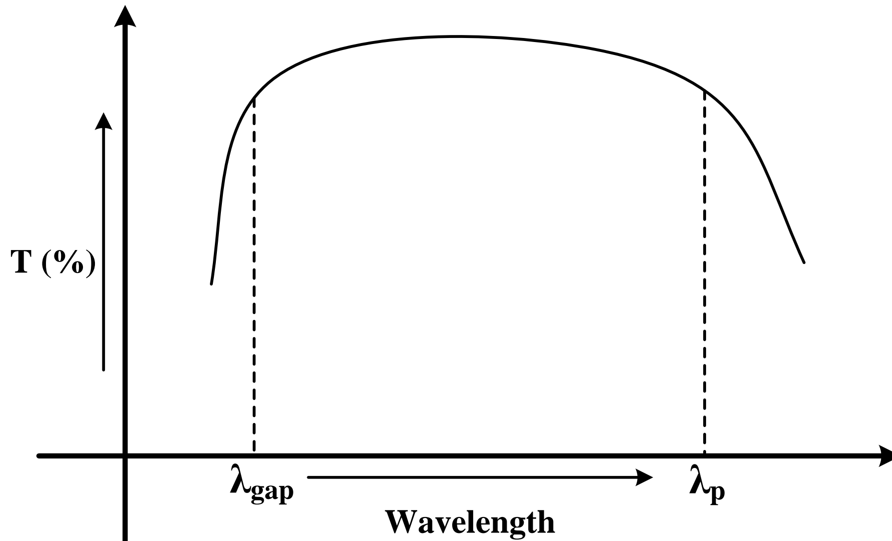

Figure 1.2 Spectral dependence of TCOs.

1.4 Simultaneous occurrence of optical transparency and electrical conductivity in TCOs.

In the general context, optical transparency and electrical conductivity are regarded as mutually exclusive properties. The solution to Maxwell's equation [48] delivers the refractive index and extinction co-efficient for electromagnetic (EM) waves through a semiconducting medium as,

$$n^2 = \frac{\epsilon}{2}\,[\,[1 + \left(\frac{2\sigma}{\upsilon}\right)^2]^{0.5} + 1] \quad \text{.......................(1.4)}$$

and $$k^2 = \frac{\epsilon}{2}\,[\,[1 + (\frac{2\sigma}{\upsilon})^2]^{0.5} - 1] \quad \text{................(1.5)}$$

where n gives the index of refraction of the medium,

k gives the coefficient of extinction,

∈ gives the dielectric constant,

σ is the value of conductivity and

ν is the frequency of electromagnetic radiation.

For insulators, the conductivity is zero, and hence, σ is nearly zero. Hence from the above equations, n approaches $\varepsilon^{1/2}$ and k approaches zero - that is, insulators allow electromagnetic waves to pass through them, whereas for an ideal conductor, the components of reflected and transmitted electric field vector get totally reflected with a 180^0 phase difference. That is, an ideal conductor reflects the EM waves falling on it, while an insulator acts transparent to the EM radiations [49].

Most TCOs will be transparent ~ 80% along the visible region of the EM spectrum and fluctuations produced as a result of interference effects are observed in the optical spectroscopy studies. The short wavelength cut off around 300 - 400nm are resulted owing to the fundamental band gap excitation from the valence to conduction band in figure 1.3.

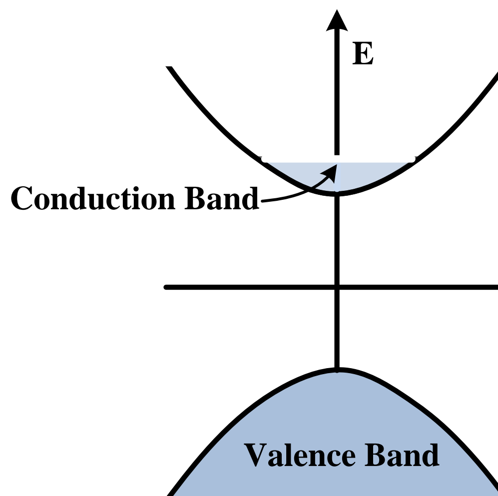

Figure 1.3 Schematic diagram showing valence and conduction band in TCOs.

Typically in the optical spectrum of a TCO, decrease in transmission starts around 1000 nm and almost simultaneously increase in reflection starts. This is due to oscillations of large number of conduction band electrons, also known as plasmons. This can result in considerable absorption of incident radiation with a maximum value at characteristic plasma wavelength, λ_p.

Due to substitutional doping, the number of conduction band electrons (N) increases resulting in shifting of plasma wavelength to a smaller value, since plasma wavelength is inversely proportional to N [45] according to the relation,

$$\lambda_p \propto 1/\sqrt{N} \quad \text{.............................(1.6)}$$

This creates swap over between electrical conductivity and long wavelength transparency limit in TCOs. When the electron concentrations are very high, it may lead to decrease in transparency of the visible wavelength radiation and vice versa. Hence, we cannot label one particular TCO as '*single best TCO*', since the preferred characteristics are dependent on its possible applications.

Since the most significant parameters governing a TCO- optical transparency and electrical conductivity are inversely related, the performance of one thin film TCO can be compared with another using a term '*figure of merit*', which is generally regarded as the ratio of transmission of light to the sheet resistance of the thin film [50]. Since transmission through a thin film depends on its thickness, this definition of figure of merit depends on thickness of the thin film. According to another definition given by Iles and Soclof [51], figure of merit,

$$F = R_s[1-T] \quad \text{..............................(1.7)}$$

where R_s is the sheet resistance and T is the transmission and a lower figure of merit indicates a film of superior quality. Figure of merit depends on mobility, which is in turn affected by electron scattering by phonons. It has no dependence on the charge carrier concentration and the grain boundary scattering lowers mobility of charge carriers in thin film TCOs.

1.5 Other characteristics of TCOs

Thermal stability of TCO is an important parameter to be taken care of while using it for external applications. Generally, it remains stable up to a temperature slightly greater than its deposition temperature [52]. In order to obtain best TCO properties, the substrates should be maintained at sufficiently high temperature during deposition. The optimum substrate temperature increases in the order, ITO < ZnO < SnO_2 < Cd_2SnO_4.

Due to higher substrate temperatures used, there is a chance for diffusion of sodium into TCO layers while using soda lime glass [53]. A coating of silica or alumina barrier layer can be given in order to avoid this. Other significant features preferred for TCOs are chemical stability; the ability to withstand corrosive chemical environment, and mechanical durability which depends on the materials from which they are formed. The cost of production plays a major role in the selection of a particular TCO for a specific use. The price of raw materials, method of thin film deposition as well as speed of the process is also significant. Certain compounds of cadmium are carcinogens and are restricted in use as TCOs. Hence the cost of processing these compounds to prevent release of toxic materials into the environment and to protect the users is very high. Toxicity of elements generally has the order zinc < tin < indium < silver < cadmium [54].

1.6 Different types of TCOs

a) *n*- type TCO

The immense research in the field of TCOs has resulted in the development of variety of *n*-type TCOs, suitable for use in various applications. TCOs are mainly *n*-type due to the ease in creating oxygen vacancies and in oxides, cation interstitials. TCO properties can be enhanced by introducing other elements or impurities intentionally into the lattice of a pure oxide, by substitutional doping. Majority of TCOs in use and under research are *n*-type since doping can be quite easily achieved in them, compared to *p*-type [55-60]. A detailed study about *n*-type TCOs is presented in Chapter 4.

b) *p*-type TCO

Even though there are quite a large number of *n*-type TCOs in use, the number of *p*-type TCOs is very limited. In *p*-type TCOs, majority charge carriers are positively charged holes created by the absence of electrons. Their modelling and processing are still being a great challenge, despite much efforts. The pioneering works on *p*-type conducting oxides had been conducted by Kawazoe and Hosono on $CuAlO_2$ [20] and $SrCu_2O_2$ [62] respectively. They have achieved good conductivity, but the carrier density (N) and mobility (m) were low, typically N < $10^{18}/cm^3$ and m < 1 cm^2/Vs. Even though enormous research efforts have been put on these materials, these problems still persist in these copper based metal oxides. Recently works have been done to improve the desirable properties of sulphides and selenides such as LaCuOS [63], BaCuSF [64]. Due to the large hole effective masses of most oxides, they exhibit much lower carrier mobilities [65]. *p*-type TCOs are applied in a variety of electronic devices and can possibly serve as positive terminals in optoelectronic devices, allowing new solar cell architectures. We shall discuss about *p*-type TCOs extensively in Chapter 5.

c) Amorphous TCOs

It has been a historical belief that crystalline materials have superior properties, but the emergence of new amorphous TCOs has challenged it; they possess properties even better than their crystalline counterparts. They also offer advantages of low temperature processing and hence can be used for flexible substrates. Amorphous TCOs were illustrated mainly by the ternary compound InGaZnO [66,67] and the binary Cd_2SnO_4 [68]. The electronic transport mechanism in these systems is complex, but the performance is superior, especially electron mobility achieved was as high as 50 cm^2/Vs, superior to some of the available crystalline TCOs [69, 70]. These materials are amorphous mixtures in which all single metal oxides have filled up *d*-shells. The conduction band states arise mainly from vacant *s*-states of metal atoms. Hosono et al. stated that elevated mobility of electrons in amorphous TCOs may be due to overlap of *s*-states of such large metal atom [71]. However, over the past decade, TCO material synthesis in both

crystalline and amorphous state has progressed so as to make a difference of an order of magnitude or more in the attainable maximum conductivity.

1.7 Applications of TCOs

In the last few years, there has been an extensive increase in active research groups as well as number of publications in the field of transparent conducting oxides. This is mainly due to inevitability of this class of materials in applications such as flexible electronics, solar cells, display systems and most recently in thin film transistors. The development of high definition flat screen televisions, electro chromic windows, transparent electrodes etc. had been contributed mainly by TCOs.

Touch-screen sensors, plasma and organic light emitting diode (OLED) displays, low emissivity windows, liquid crystal display (LCD) devices, smart windows and photovoltaic devices are some of the innumerable applications of these materials. Smart windows or energy efficient windows are capable of sensing and responding to external stimuli such as heat, light or electricity and can change from transparent to translucent to opaque with the simple turn of a knob [72]. It regulates the passage of light through it, thereby regulating indoor light and temperature for households or industries. It influences the energy use of the building and occupant comfort. The materials used in these systems are either electro chromic, thermo chromic or photo chromic and typically comprises of a passive counter electrode inserted among transparent conductors [73]. The assembly of a smart window is schematically shown in figure 1.4.

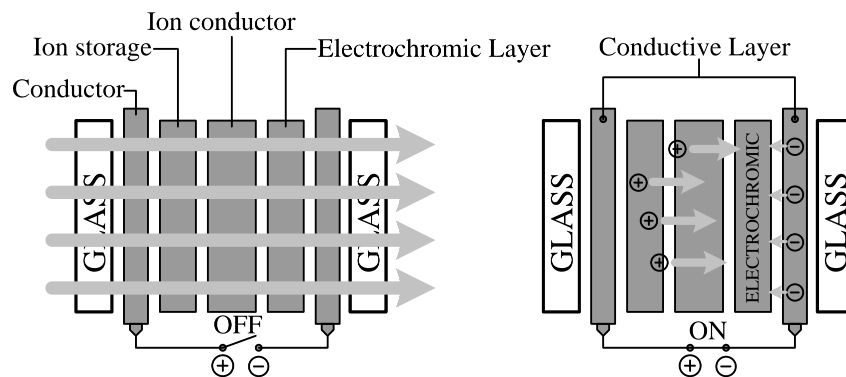

Figure 1.4 Schematic diagram of the assembly of a smart window

Low emissivity windows are yet another class of smart windows, used to block particular wavelengths incident on it. For instance, they are used typically to prevent IR radiation passing all the way through the window. This considerably reduces inside temperature of the building without diminution of incoming light. Besides, these windows are capable of color controlling property, where photo chromic or electro chromic coatings are given on TCO materials depending on their applications. Using the electronic control system incorporated, the colours and patterns on the windows can be varied within seconds providing a novel dimension to beautification of contemporary buildings [74].

It has been predicted that by 2020 transparent conducting films will become a $3.39 billion dollar market for printed electronics, largely due to photovoltaic, optoelectronic and OLED display applications [75]. There are various companies such as Evaporated coatings inc Ltd. that manufacture TCOs - indium tin oxide, transparent gold and various other transparent and conductive coatings which are typically employed in applications that demand high transmission of visible light and electrically conducting surface. They supply TC coatings for applications requiring environmental stability such as in military, medical displays, security and aerospace, display windows, LCD fabrication, heaters, touch panels, cathode ray tube displays, heads-up displays, shielding for electromagnetic interference and radio frequency interference [76].

Touch screens are now inevitable in human lives - from simple mobile phones to the complicated machineries and instruments. They are fabricated mainly on glass substrates, coated with a TCO material and transparent patterns created on it by means of lithography. Screen patterns are fed to software, where the touch is sensed by the recognition of change in resistivity or capacitance, identified through microprocessors. In this simple device architecture, as given in figure 1.5, all materials used are transparent, thereby making the vision vivid to the device user.

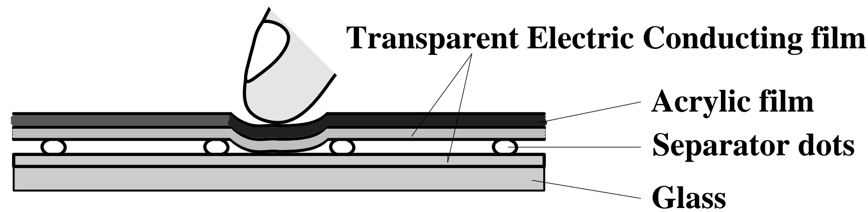

Figure 1.5 Schematic of a touch sensor

Quite a lot of display units have also been grown by TCO electrodes - Liquid Crystal Display (LCD) being one of the most popular. It is assembled by patterning TCOs using lithography and liquid crystals sandwiched between two transparent conductors, as in figure 1.6. On receipt of electrical signals, the crystals orient themselves between the electrodes, thereby generating specific colors [77].

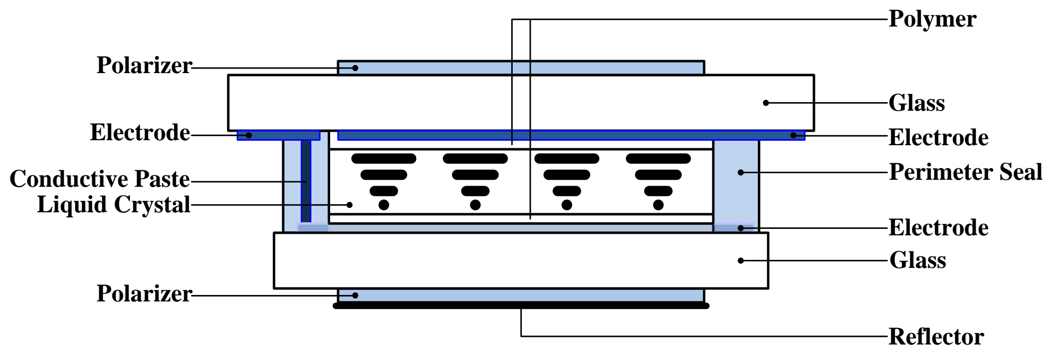

Figure 1.6 Schematic of an LCD display unit

Photovoltaic devices using organic or inorganic semiconductors produce electric power when light is incident on it. TCOs are deposited to form *p-n* junctions depending on the applications like thin-film transistors (TFTs) used in modern microelectronics. They ought to be flexible, shock resistant, portable and financially affordable in optoelectronics industry [78]. Together with transparent circuit technology, TFTs can function as display units on different areas; even on the windscreens of cars.

Transparent field-effect transistors (TFET), yet another major application of TCs, developed from wide band gap semiconducting materials, exhibit superior performance and durability at high temperatures and high power operation [79]. Oxide semiconductors provide an alternative prospect for discovering novel usability with supplementary functionality, since they exhibit various magnetic and electronic behaviors which originate from their crystal structure and constituent elements.

Scientists at National Renewable Energy Laboratory (NREL) are involved in high end research for enhancing the properties of existing TCOs as well as addition of novel materials in TCO phase space [80]. Transparent conducting nano fiber papers have been developed by Masaya Nogi et. al. for the potential use in foldable solar cells and future portable electronic devices [81].

1.8 Specific objectives of this work

The main objective of this work is to fabricate transparent and conducting thin films for device applications and their detailed structural, electrical, optical and morphological investigation. In this thesis, a comprehensive elucidation of the fabrication of tin based *n*-type and copper based *p*-type TCO thin films by radio frequency magnetron sputtering is presented. It also accounts for the optimization of fabrication parameters to obtain good optical transparency and high electrical conductivity. Indium 3^+ was chosen as the conducting ion that can be fused with both these TCO materials in order to enhance their optical and electrical behavior. Hence indium tin oxide (ITO) and copper indium oxide (CIO) thin films were synthesized and investigated.

Tin oxide and indium tin oxide were selected as *n*-type TCOs, due to previous reports on their good electrical conductivity along with optical transparency [8, 9]. Secondly, copper oxide and copper indium oxide were selected as *p*-type TCOs due to its natural *p*-type conductivity which is rare among existing TCOs [82].

Objectives of the present work, which has been successfully completed, are as follows:

I. Optimization of radio frequency magnetron sputtering (RFMS) parameters of the system for the fabrication of thin films.

II. Investigation of the effects of substrate temperature, RF sputter power, time duration of sputtering and nature of substrates on the quality of thin films obtained.

III. Studies on the optical properties of fabricated thin films to optimize the synthesis conditions to maximize their transparency in the visible range.

IV. Structural characterization of these sputtered thin films using X-Ray Diffraction and X-Ray Photoelectron Spectroscopy.

V. Investigations on the charge carrier concentration and their mobility to maximize electrical conductivity.

VI. Exploration of the influence of sputtering conditions on the surface morphological behavior of the films.

VII. Finally and most importantly, highly transparent *p-n* hetero junctions were constructed using these *n* and *p*-type conducting oxides to form diode structures.

VIII. Investigation of unidirectional conduction properties and computation of ideality factors of these hetero junctions.

References

[1] Sebastian C. Dixon, David O. Scanlon, Claire J. Carmalt and Ivan P. Parkin, Journal of Materials Chemistry C, 4 (2016) 6946.

[2] A. L. Dawar and J. C. Joshi, Journal of Materials Science, 19 (1984) 1.

[3] Marius Grundmann, Andreas Rahm, Holger Von Wenckstern, Physica Status Solidi A, 212, 7 (2015) 1408.

[4] Yan M, Zhang Q, Zhao Y, Yang J, Yang T, Zhang J, Li X. Journal of Nano science and Nanotechnology, 15,9 (2015) 6279.

[5] E. Fortunato, D. Ginley, H. Hosono and D. C. Paine, MRS Bulletin, 32 (2007).

[6] G. J. Exarhos and X.-D. Zhou, Thin Solid Films, 515 (2007) 7025.

[7] K. Badeker, Annals of Physics (Leipzig) 22 (1907) 749.

[8] Mohammad Hossein Habibi and Nasrin Talebian, Acta Chimica Slovenica, 52 (2005) 53.

[9] M. Ait Aouaj, R. Diaz, A. Belayachi, F. Rueda, M. Abd-Lefdil, Materials Research Bulletin, 44 (2009) 1458.

[10] Emin Bacaksiz, Serdar Aksu, Salih Yılmaz, Mehmet Parlak, Mustafa Altunbaş, Thin Solid Films, 518 (2010) 4076.

[11] P. D. Sesion Jr, J. M. Henriques, C. A. Barboza, E. L. Albuquerque, V. N. Freire and E. W. S. Caetano, Journal of Physics: Condensed Matter, 22 (2010) 43.

[12] Khuong P. Ong, Xiaofeng Fan, Alaska Subedi, Michael B. Sullivan, and David J. Singh, APL Materials, 3 (2015) 062505.

[13] Mario A. Alpuche-Aviles and Yiying Wu, Journal of American Chemical Society, 131 (2009) 3216.

[14] Kenji Nomura, Hiromichi Ohta, Kazushige Ueda, Toshio Kamiya, Masahiro Orita, Masahiro Hirano, Toshiyuki Suzuki, Chizuru Honjyo, Yuichi Ikuhara and Hideo Hosono, Journal of Applied Physics, 95 (2004) 5532.

[15] W. Assenmacher, G. Schnakenburg, Y. Michiue, Y. Kanke,N. Kimizuka and W. Mader, Journal of Solid State Chemistry, 215 (2014) 176.

[16] R. Asahi, A. Wang, J. R. Babcock, N. L. Edleman, A. W. Metz, M. A. Lane, V. P. Dravid, C. R. Kannewurf, A. J. Freeman and T. J. Marks, Thin Solid Films, 411 (2002) 101.

[17] H. Mizoguchi and P. M. Woodward, Chemistry of Materials, 16 (2004) 5233.

[18] J. E. Medvedeva and A. J. Freeman, Euro Physics Letters, 69 (2005) 583.

[19] J. E. Medvedeva, Applied Physics A, 89 (2007) 43.

[20] Kawazoe, Yasukawa and Hyodo, Nature, 389 (1997) 939.

[21] W. Suzhen , D. Zanhong, D. Weiwei , S. Jinghen and F. Xiaodong, Journal of Semiconductors, 35, 4 (2014) 043001.

[22] Kate G. Godinho, John J. Carey, Benjamin J. Morgan, David O. Scanlon and Graeme W. Watson, Journal of Materials Chemistry, 20 (2010) 1086.

[23] Ruiqin Ding, Huiqun Zhu and Qingguang Zeng, Vacuum, 82 (2008) 510.

[24] Farsad Imtiaz Chowdhury, Thomas Blaine and Adel B. Gougam, Energy Procedia, 42 (2013) 660.

[25] Hanlin Luo, Zhen Fang, Na Song, Timothy Garvey, Rene Lopez, and Thomas J. Meyer, ACS Applied Materials & Interfaces, 7 (2015) 25121.

[26] Yanli Liu, Yufang Li, and Haibo Zeng, Journal of Nanomaterials, 196521 (2013).

[27] Shu Jin, Yu Yang, Julia E. Medvedeva, John R. Ireland, Andrew W. Metz, Jun Ni, Carl R. Kannewurf, Arthur J. Freeman and Tobin J. Marks, Journal of American Chemical Society, 126 (2004) 13787.

[28] T. S. Moss, Proceedings of the Physical Society B, 67 (1954) 775.

[29] Antonio Facchetti and Tobin J. Marks, Transparent Electronics: From Synthesis to Applications (2010) John Wiley & Sons Ltd.

[30] K. Sreenivas, T. Sudarsana Rao, A Mansingh and S. Chandra, Journal of Applied Physics, 57 (1985) 384.

[31] H.A. McMaster, U.S. Patent 2, 429, 420 (1947).

[32] J.M. Mochel, U.S. Patent 2, 564, 706 (1947).

[33] J.M. Mochel, U.S. Patent 2, 564, 707 (1951).

[34] G. Helwig, Zeitschrift für Physik, 132 (1952) 621.

[35] L. Holland and G. Siddall, Vacuum, 3, 4 (1953) 375.

[36] R. Groth, Physica Status Solidi, 14 (1969) 69.

[37] H.F. Dates and J.K. Davis, U.S. Patent 3, 331, 702 (1967).

[38] A.J. Nozik, Physical Review B, 6 (1972) 453.

[39] H. Enoki, T. Nakayama and J. Echigoya, Physica Status Solidi A, 129 (1992) 181.

[40] T. Minami, H. Sonohara, S. Takata and H. Sato, Japanese Journal of Applied Physics, 2, 33 (1994) L1693.

[41] M. Orita, H. Ohta, M. Hirano, S. Narushima and H. Hosono, Philosophical Magazine B, 81 (2001) 501.

[42] Toshihiro Moriga, Yukako Hayashi, Kumiko Kondo, Yusuke Nishimura, Kei-ichiro Murai, and Ichiro Nakabayashi, Journal of Vacuum Science and Technology A, 22 (2004) 1705.

[43] Abdul Faheem Khan, Mazhar Mehmood, A. M. Rana, M. T. Bhatti and A. Mahmood, Chinese Physical Letters, 26, 7 (2009) 077803.

[44] Shinho Cho, Metals and Materials International, 19, 6 (2013) 1327.

[45] David S Ginley, Handbook of Transparent conductors (2010) Springer New York.

[46] I Hamberg and C G Gramquist, Journal of Applied Physics, 60 (1986) R123.

[47] H. L. Hartnagel, A. L. Dawar, A. K. Jain and C. Jagdish, Semiconducting Transparent thin films (1995) IOP Publishing Ltd.

[48] D. Griffiths, Introduction to Electrodynamics (1999) Prentice Hall, New Jersey.

[49] Jordan and Balmain, Electromagnetic waves and radiating systems (1964) Prentice Hall, India.

[50] D. B. Fraser, H. D. Cook, Journal of Electrochemical Society, 119 (1972) 1368.

[51] P. A. Iles and S. I. Soclof, Proceedings of 12th IEEE Photovoltaic Conference, (1976) 978.

[52] Tadatsugu Minami, Takeshi Kuboi, Toshihiro Miyata, and Yuusuke Ohtani, Physica Status Solidi A, 205, 2 (2008) 255.

[53] G. R. Asoka Kumara, C. S. Kumara Ranasinghe, E. Nirmada Jayaweera, H. M. Navaratne Bandara, Masayuki Okuya, and R. M. Gamini Rajapakse, Journal of Physical Chemistry C, 118 (2014) 16479.

[54] Clark I. Bright, Review of Transparent Conductive Oxides (2007) http:// www. svc. org/ DigitalLibrary/documents/2008_Fall_CIBright.pdf.

[55] Tsuyoshi Nakajima and Henri Groult, Fluorinated Materials for Energy Conversion (2005) Elsevier.

[56] Computational Chemistry Group, Trinity College, Dublin http://chemistry.tcd.ie/staff/people/gww/gw_new/research/TCOs/n-type.

[57] Zhangxian Chen, Liang Huang, Qingfan Zhang, Yongjie Xi, Ran Li, Wanchao Li, Guoqin Xu and Hansong Cheng, Journal of Physical Chemistry C, 119 (2015) 4789.

[58] Viet-Anh Ha, David Waroquiers, Gian-Marco Rignanese and Geoffroy Hautier, arxiv.org/pdf/1603.04038.pdf.

[59] Peter Agoston, Christoph Korber, Andreas Klein, Martti J. Puska, Risto M. Nieminen and Karsten Albe, Journal of Applied Physics, 108 (2010) 053511.

[60] T. Minami, MRS Bulletin (2000) doi: 10.1557/mrs2000.149

[61] M. A. Marquardt, N. A. Ashmore, and D. P. Cann, Thin Solid Films, 496 (2006) 146.

[62] T. Otabe, K. Ueda, A. Kudoh, and H. Hosono, Applied Physics Letters, 71 (1998) 1036.

[63] Y. Nakachi and K. Ueda, Journal of Crystal Growth, 311 (2008) 114.

[64] H. Yanagi, J. Tate, S.Park and H. Hosano, Journal of Applied Physics, 100, 8 (2006) 083705.

[65] Geoffroy Hautier, Anna Miglio, Gerbrand Ceder, Gian-Marco Rignanese and Xavier Gonze, Nature Communications, 4 (2013) 2292.

[66] Matthew P. Taylor, Dennis W. Readey, Charles W. Teplin, Maikel F. A. M. van Hest, Jeff L. Alleman, Matthew S. Dabney, Lynn M. Gedvilas, Brian M. Keyes, Bobby To, John D. Perkins and David S. Ginley, Measurement Science and Technology, 16 (2005) 90.

[67] Chien-Yie Tsay, Tzu-Yi Yan, Journal of Physics and Chemistry of Solids, 75 (2014) 142.

[68] X. Wu, P. Sheldon, T.J. Courts, D.H. Rose, and H.R. Moutinho, NREL/CP-520-22941 (1997).

[69] K.Nomura, H.Ohta, K.Ueda, T.Kamio, M.Hirano and H.Hosono, Science, 300 (2003) 23.

[70] Fortunato E, Ginley D, Hosono H and Paine D.C, MRS Bulletin, 32 (2007) 242.

[71] Toshio Kamiya and Hideo Hosono, NPG Asia Materials, 2 (2010) 15.

[72] Evan L. Runnerstrom, Anna Llordes, Sebastien D. Lounisac and Delia J. Milliron, Chemical Communications, 50 (2014) 10555.

[73] Rong-Hua Ma and Yu- Chia Chen , Sensors, 12 (2012) 359.

[74] Marco Casini, Proceedings of the Second International Conference on Advances In Civil, Structural and Environmental Engineering- ACSEE 2014.

[75] Luis Rebouta, Mikkeli International Industrial Coating Seminar (2010) www.miics.net/archive/getfile.php?file=159.

[76] www.evaporatedcoatings.com/transparent-conductive-coatings.

[77] http://www.fujitsu.com/downloads/MICRO/fma/pdf/LCD_Backgrounder.pdf.

[78] K.Nomura, H.Ohta, A.Takagi, T.Kamio, M.Hirano and H.Hosono, Nature, 432 (2004) 25.

[79] C. Besleaga, G. E. Stan, I. Pintilie, P. Barquinha, E. Fortunato and R. Martins, Applied Surface Science, 379 (2016) 270.

[80] John Perkins, www. eere. energy. gov/ solar/ review_meeting /pdfs /prm2010_nrel_perkins.pdf.

[81] Masaya Nogi, Makoto Karakawa, Natsuki Komoda, Hitomi Yagyu and Thi Thi Nge, www.nature.com/scientificreports/ 5:17254.

[82] A. N. Banerjee and K. K. Chattopadhyay, Progress in Crystal Growth and Characterization of Materials, 50 (2005) 52.

CHAPTER 2

THIN FILM DEPOSITION TECHNIQUES

2.1 Introduction

Any three dimensional film with one dimension much lesser compared to the other two may be termed as a 'thin film'. The thickness of a thin film used in devices would in general be about 50nm to 50μm, very less compared to devices using bulk materials with thickness above 1mm [1]. This enables miniaturisation of devices to a large extend. The microstructure, nature of dopants present and physical properties determine the specific use of a thin film, which are in turn influenced by the technique adopted for its fabrication. By altering substrate temperature, rate of deposition, partial pressure, chemical concentration of reacting materials and many other thermodynamic parameters, a multitude of properties can be obtained, depending on the method of thin film deposition [2]. Various methods for thin film growth have been intensively investigated for their explicit uses, since growth techniques play a considerable role in governing properties of films.

In general, deposition of thin films undergoes the following sequential steps:

1. The source material/target is converted into solid/liquid condensed phase.
2. From the condensed phase, it is converted into vapour form-atomic, molecular or ionic.
3. It is transported to a substrate by applying pressure/voltage/magnetic field.
4. It is then made to condense onto the substrate to coat a thin film.

Depending on how the vapour form is created for condensation, the thin film deposition methods can be classified broadly into two-chemical methods and physical methods, as explained in subsequent sections.

2.2 Chemical methods of thin film deposition

There are numerous chemical deposition techniques for material formation, which includes wet chemical processes such as spray pyrolysis, dip/spin coating, electroplating, chemical reduction plating and vapour phase deposition such as chemical vapour deposition (CVD) and metal-organic CVD (MOCVD). Certain

deposition techniques used for fabrication of TCO thin films are discussed in the subsequent sections.

2.2.1 Spray pyrolysis

This is one of the methods adopted for the bulk fabrication of films in large area coatings used in industries, which is relatively simple and economic. Basically, it depends on the decomposition of a compound (metal) in liquid form, when sprayed onto a pre-heated substrate. The hydrolysis of metal chloride on heated surface takes place as follows to give well adherent films.

$$MCl_x + y\,H_2O - MO_y + xHCl \text{ ....} (2.1)$$

M can be any metal such as Zn, In or Sn. A carrier gas provides enough pressure at the spray nozzle for the atomisation of precursor solution into spray of fine droplets. The flow rate can be controlled at the nozzle, which determines the growth kinetics and hence the quality of films grown. The temperature of substrate during deposition, concentration of precursor solution, the nozzle to substrate distance etc. are some of the other important parameters in spray pyrolysis as described elsewhere [3,4]. Spray deposited TCO films do not generally require a post deposition heat treatment to improve TCO characteristics, as needed in alternative processes. Also, it provides an easy way to dope any element in the required proportion through solution medium by controlled addition. However, certain unavoidable disadvantages of this method exist, such as possibility of oxidation of sulphides when using corresponding precursors at normal pressure and temperature. Also the spray nozzle may become clogged in the long run, causing variations in droplet size and pressure at the nozzle, thereby reducing the quality of films and hence its properties.

2.2.2 Dip coating

Dip coating represents one of the oldest commercially applied thin film manufacturing processes. In this method, a substrate is dipped into a precursor solution at constant speed and left for sufficient dwell time for the interaction of

substrate with the solution. Then the substrate is pulled away from the solution at a constant speed, whereby a thin layer of precursor solution is deposited onto the substrate [5]. Excess solution drips off the surface. The solvent evaporates and after drying, the substrate may be subjected to further heat treatment to enhance crystallization of the functional oxides. This process can be applied to all types of precursor solutions, but no universally valid model has been approved yet. The surface morphology of films is controlled mainly by viscosity of precursor solution and hence, it is very difficult to control the thickness of films precisely. Also, repeatability of films is very less compared to other methods of thin film coating. One of the major disadvantages in this technique is that both sides of the substrate gets coated; if coating is preferred only on a single side, the other side has to be sealed or protected by an adhesive foil, which creates much complications.

2.2.3 Spin coating

Spin coating involves the acceleration of a viscous liquid on a rotating substrate. The solution to be coated is poured at the center of the substrate before rotation. The spin speed controls the centrifugal force and the solvent viscosity controls the viscous forces and a balance between the two forces leads to a coating of homogeneous layer of solution onto the substrate. Thus the film properties can be diverse by varying the solution viscosity, concentration, angular speed and spin time. Multiple coatings are preferred to obtain a film of homogeneous thickness. The range of film thicknesses obtained by spin coating is 1-200 mm. This method is widespread in organic electronics and nanotechnology for effective device preparation. The advantage of spin coating is its ability of quick and easy production of films [6, 7]. Similar to dip coating, in this method, the thickness of films cannot be controlled precisely. Also, this process has relatively low throughput compared to other methods, since the fast drying times lead to lower yield for certain specific applications, which requires time to self-assemble or crystallize. Also, material usage is typically around 10%, which is very low; the rest gets flung off sideways and wasted.

2.2.4 Chemical Vapour Deposition

A very significant method used to obtain semiconducting transparent thin films is chemical vapour deposition (CVD). This involves the deposition of metal oxide film from one or more gaseous reacting species on to a solid substrate. Metal oxide thin films are usually grown by vaporising suitable organo-metallic compounds onto a substrate surface, where it is decomposed by a heterogeneous process. Various deposition parameters such as gas flow rate, system geometry and substrate temperature influences the quality of thin films deposited by this method [8]. Highly pure and stoichiometric films with structural perfection can be obtained by this method. The most common method involves the use of metal-organic precursors and is thus known as Metal-Organic CVD. The reproducibility and purity of films, low cost involved in the production and the non-use of vacuum are the main advantages of this method along with the ease in large scale production, since it can be performed as a continuous process. A significant disadvantage results, since the morphology of thin films depends on the behaviour of chemical reaction and activation mechanism, the nature of resultant films are highly unpredictable [9]. Also, a possibility of carbon contamination from metal-organic precursors in the films, adhesion problems and incompatibility of substrate with temperature and possible side reactions are certain disadvantages of this method.

2.3 Physical methods of thin film deposition

In this technique, the films are deposited in high vacuum chambers, retaining a vacuum of 10^{-5} mbar, created by a diffusion pump, typically backed by a rotary pump. Certain important deposition techniques that fall under this category are vacuum evaporation, electron beam evaporation, pulsed laser deposition and sputtering. We shall briefly discuss each method.

2.3.1 Vacuum Evaporation

In this method, a resistively heated material is evaporated using a tungsten or tantalum source. Oxygen deficiency occurs while evaporating an oxide material, and

hence, this method usually requires heat treatment in the presence of oxygen, post deposition [10]. In order to grow transparent thin films, an oxygen partial pressure of 10^{-4} Torr is necessary [11]. The substrate temperature, source to substrate distance, evaporation rate, oxygen partial pressure etc. are the major control parameters. It is a relatively simple and appropriate method for the deposition of metals and alloys, as the only major prerequisite is a vacuum atmosphere, where adequate heat is supplied to the evaporants to achieve necessary vapour pressure.

2.3.2 Electron Beam evaporation

Electron beam evaporation is a process in which a source material is bombarded with an electron beam generated by a tungsten filament under high vacuum [12]. This deposition method utilises a stream of electrons accelerated through 5-10kV fields, which are focussed on a target material to be evaporated. The electron beam forces atoms from the target to evaporate and form a gaseous phase. These atoms form a solid layer, thereby coating the substrate with a layer of the anode material. The impinging electrons generate the heat required to evaporate the material to be coated. The purity of thin film coatings is high using this method since deposition is carried out in high vacuum. Also the rate of deposition can be regulated to be as low as 1 nm per minute to as high as few micrometers per minute. The efficiency of material utilization is relatively high, compared to other methods and also it offers structural and morphological control of films [13-15].

2.3.3 Molecular Beam Epitaxy

This technique to fabricate highly crystalline thin films was introduced by A. Y. Cho and J. R. Arthur at Bell laboratories [16]. This method utilises ultrahigh vacuum (UHV) conditions with much accurate controllability of composition, thickness and morphology [17-19]. Also, it enables the facility to study the growth of crystals on a sub nano meter scale. In this method, the material to be coated is sublimated or evaporated from an effusion cell, forming molecular beams, which are made incident onto a heated rotating substrate with ordered placement of atoms. The

source can be in liquid form-Liquid Phase Epitaxy or vapour form - Vapour Phase Epitaxy or molecular source (MBE) [20].

2.3.4 Pulsed Laser Deposition

An efficient evaporation method for the fabrication of epitaxial films under modest vacuum conditions is pulsed laser deposition (PLD) [21]. Generally this method is preferred for the phase pure growth of multi component composite thin films. It requires a laser source (pulsed) - frequency tripled (355 nm) or quadrupled (266 nm) solid state Nd:YAG laser, KrF (248 nm) or ArF (193 nm) excimer laser. In a usual PLD method, a highly focused beam of laser pulses with high energy, obtained typically from a UV nanosecond pulsed laser source, is moved over the target. A substrate is introduced to the laser plume, created due to the interaction between high energy beam and target. The laser plume comprises of atomic and molecular structures ablated from target. For the deposition of a TCO film, a substrate temperature of 450°C-700°C is used, and the oxygen partial pressure is kept below several milli torr, since decrease in oxygen partial pressure causes formation of vacancies, which in turn generates free carriers, thereby enhancing conductivity [22].

2.3.5 Sputtering

The sputtering process is considered to be the most versatile thin film deposition technique. It is a process whereby atoms are ejected from a solid source material due to bombardment by energetic ions, usually by means of plasma which generate charged particles that are accelerated towards a surface. It produces coatings of device quality, higher purity, much controlled thickness with greater adhesion and film homogeneity. Sputtering was first developed by W.R. Grove in 1852; this method basically involves the formation of ionized plasma of argon in the space between the two electrodes when voltage is applied between a cathode and anode [23]. Usually, cathode is the target material and substrate holder acts as the anode. The target material is bombarded heavily by ions, ejecting atoms from the surface of the cathode through momentum transfer. These particles diffuse away

from the cathode, through the plasma towards the anode, forming a layer of thin film onto the substrate. The pressure inside the sputtering chamber during the process has profound influence on the uniformity, quality, and stress of the resultant film. Initially the chamber is evacuated to 10^{-6} mbar and during sputtering; the chamber is evacuated normally to a pressure of 10^{-2}–10^{-3} Torr [24]. Depending on the mode of powering the sputtering system, they are classified into two; DC and RF system [25-27].

2.3.5.1 DC sputtering: When the source of ions is provided by glow discharge created by an applied electric field between electrodes in a gas at low pressure, the gas breaks down to conduct electricity. This ionized gas or plasma is accelerated by a large electric field. When these ions impact the target, atoms (or molecules) are ejected from the surface, into the plasma, where they are carried away and deposited on the substrate. This simplest and least expensive method of sputtering is DC sputtering, in which a DC power supply is used. In this system, generally restricted for conducting materials, a direct voltage is applied between cathode and anode. The sputter gas used is typically inert, such as argon, in order to avoid any possible chemical reaction between sputtered atoms and sputtering gas [28-30].

During sputter deposition, there is a chance for the formation of arcs, due to accumulation of oxides on erosion groove edges where the rate of sputter is low. When the circuit senses a strong lessening of discharge voltage or a rapid raise of discharge current, the power gets switched off for a small time interval (a few microseconds) in order to reduce charging and prevent the creation of arc. Arcing could possibly destroy a target by melting which eventually results in particulates or pinholes on deposited films, degrading the quality of the films. To avoid this, periodic reversal of polarity can be done as in RF sputtering. Also, an increase in discharge voltage leads to enormous power at the anode, resulting in substrate heating. Thus, the choice of materials for substrates is limited in DC sputter systems. Hence, modified systems have been developed, such as magnetron sputtering system, in which electron trajectories are defined by electric as well as magnetic fields, discussed in the next section.

2.3.5.2 RF magnetron sputtering: RF Magnetron Sputtering is a reliable technique used to deposit both conducting as well as electrically insulating samples. This is currently the most significant technique for film deposition, due to its capability to grow high quality films on large area, high deposition rates and usage of lower substrate temperatures [31]. Also, adhesive property of films is superior to that of evaporated films using corresponding film/substrate combination [32]. Previously, successful deposition of TCOs by this method was hindered by low deposition rates, substrate heating effects and low ionization efficiencies in plasma which often resulted in low-grade films. Intense research in the field led to the rapid development of methods to overcome these limitations.

In an RF system, between the electrodes, a high frequency generator is connected. In magnetron sputtering the high voltage RF sputtering source ionizes sputtering gas, to produce plasma. A transverse magnetic field, and electric field, located beneath the target, directs the argon atoms towards the sputter target, multiple collisions take place and atoms of the target material are released into the plasma [33]. These atoms condense upon the substrate, thus forming the film.

A matching network is used to optimize the power transfer and a permanent magnet is connected to the sputtering gun to enhance the deposition rate, by trapping electrons. This magnet creates lines of flux perpendicular to the electric field, or parallel to the target, causing secondary electrons to confine in the region near the target and increase the number of collisions. A schematic diagram of the sputtering set up is as given in figure 2.1.

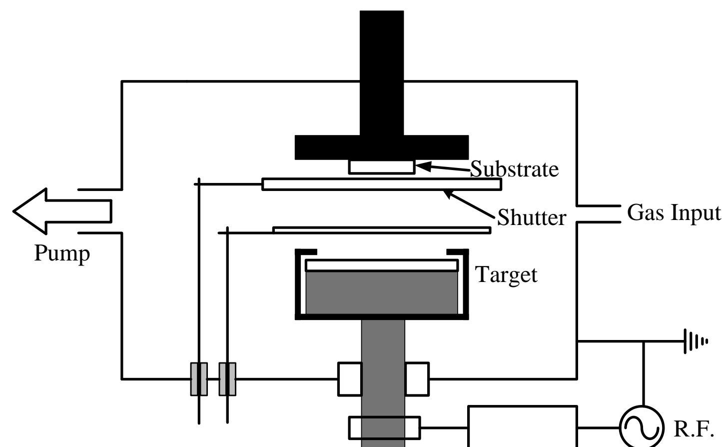

Figure 2.1 Schematic diagram of RF magnetron sputtering system

Compared to other physical vapour deposition techniques, the additional kinetic energy possessed by the sputtered atoms can lead to more adherent films and improved conformal coverage. Cylindrical, conical, and planar magnetron sources are in use for specific applications, since it benefits the formation of many different compound thin films at much lower temperature.

2.3.5.3 Reactive sputtering: Powering the magnetron for sputtering is much easier when we use a conducting or a metallic target. However, it creates a constraint in the choice of materials capable of deposition using this technique. To avoid this crisis, compounds can be coated using reactive sputtering, ie., deposition of elemental or alloy targets in reactive gases such as nitrogen, oxygen, hydrogen sulphide, etc. that can react with sputtered ions to form a stable compound on the substrate. Target-generated secondary electrons do not collide with the substrates, since near the target; they are trapped in cycloidal trajectories, and hence do not shoot up substrate temperature and cause radiation damage. However, the presence of reactive gas significantly affects the process of deposition in several ways and also increases the complication of the whole process [34].

2.3.5.4 Yield of sputter deposition: Sputtering process is said to occur when a particle hits a target with sufficient energy to dislocate an atom from the exterior plane. Sputter yield is defined as the ratio of number of ejected particles per incident projectile. In other words, it is a quantification of the rate of removal of atoms on the surface of the target material [35]. In all realistic cases, sputtering employs bombardment of ions, with inert gas ions, for instance argon, or smaller ions such as nitrogen or oxygen. Sputtering depends on the transport of momentum and kinetic energy between incident particle and the surface atoms, to break bonds and dislodge atoms and is entirely independent of charge of the particle. For incident energy up to 40 eV, no sputtering occurs, since the threshold ion energy needed for sputtering is the binding energy of the most weakly bound atom on the surface. Yield in this range is below 10^{-2}.

If the incident ion energy is in the range of 40-1000 eV, it is enough to dislodge hundreds of target atoms. The incident and impacted particles move

erratically creating knock on collisions, thereby resulting in ejection of atoms from the surface. The yield in this case varies from 0-10. In most practical laboratory and industrial purposes, this range of incident ion energy is preferred.

Incident ion energies of 1 keV to 50 keV are sufficient to break bonds between the atoms in a spherical region at the collision site. In this case, the yield is higher, but the higher energies make it impractical for use in any device applications [36]. Many researchers have explained the yield of a sputtering process in many different ways, out of which, we shall discuss the one proposed by Mahan et. al [37]. They derived an expression for the sputter yield Y as,

$$Y = \frac{E}{4E_{av}} \frac{R_{PR}}{R_{PP}} \ldots\ldots\ldots\ldots\ldots\ldots\ldots\ldots\ldots. (2.2)$$

where, E is the projectile energy and E_{av}, the average energy of recoils and ratio of E/E_{av} shows the average number of recoils. The ratio between R_{PR}, the projected range of the recoils, and R_{PP}, the projected range of the projectile, gives the probable value of the recoils which are close enough to the surface to escape. The fraction ¼ gives the average probability that the ions are moving towards the surface. E_{av} and the projected range can be calculated directly using this equation, giving insight into the sputtering process.

2.4 Criteria for selection of a particular deposition technique

Deposition technology can be regarded as the major key to the development of optoelectronic and display devices, since majority of solid-state devices are built up of material structures produced by thin film deposition. Careful selection of deposition technique is indispensable for the control over the properties of resultant films [38]. In most cases, the preferred physical and morphological characteristics of the deposited films will be the decisive factor for selecting a particular deposition technology.

As discussed earlier, a multitude of process technologies are available for coating thin films. They differ in their physical and chemical principles of operation and commercial availability of equipments. However, each technology has its own advantages as well as limitations [39]. The stability, quality and repeatability of the thin films are significant, especially in the fabrication of semiconductor devices.

Taking into consideration, all these parameters, there was considerable motivation for us to choose RF Magnetron sputtering for our study since we required films having good TCO properties, film microstructure and controllable deposition rate. It is not only suitable for the low temperature fabrication of films but also easy to achieve high deposition rate on a large area, with good adhesive properties [40].

Stoichiometry had to be maintained as that of target materials. Also, RF sputtering fabricates thin films having high density, which increases its conductivity, and the films obtained are relatively smooth when compared with films produced by other deposition methods [41]. For the fabrication of transparent diodes, masking of substrates was necessary and this could easily be done in the sputter chamber. In addition to that, this method yields superior compositional control and hence, the resulting films have compositions analogous to that of target materials [42].

We have fabricated metal oxide thin films by sputtering with a source target of corresponding metals by reactive sputtering with oxygen gas and oxide target in oxygen free environment. The sputtering process is carried out in Hind Hivac 12 MSPT sputter chamber evacuated to 10^{-6} mbar using diffusion pump backed by a rotary pump. Automatic matching network controller supplied by SERENE (MC2) equipped with radio frequency power supply R301 is used. During the sputtering process, a pressure of 10^{-3} mbar is maintained in the chamber. High pure argon is used as the sputter gas and in certain cases, oxygen as reactive gas.

Figure 2.2 Radio frequency magnetron sputtering set up.
In the inset, plasma formed during the coating of ITO films.

Fully equipped set up for gas distribution system allows oxygen, argon and nitrogen into the chamber for reactive sputtering. The set up is as shown in the figure 2.2. A two inch diameter target holder and a twelve inch diameter water cooled magnetron are mounted on the base with sputter up configuration. The substrate to target distance is optimized for each target material used to obtain crystalline films. Pre-sputtering is carried out for 10 minutes before each deposition in order to remove contaminants. The thickness of thin film is monitored in situ using a quartz crystal monitor. Substrate heating is done using resistive heating method and the maximum temperature that could be attained is 500^0C. The maximum sputter power that can be supplied is 400W.

References

[1] A. Goswami, Thin film fundamentals (1996) New Age International.

[2] Leon I. Maissel and Reinhard Glang, Handbook of Thin film technology (1983) Mc Graw Hill Book Company.

[3] A. Abrutis, G. Valincius, G. Baltrunas, L. Parafionovic, A. Valiuniene and Z. Saltyte, Thin Solid Films, 515 (2007) 6817.

[4] Dainius Perednis and Ludwig J. Gauckler, Journal of Electroceramics, 14 (2005) 103.

[5] C.J.Brinker,www.unm.edu/~solgel/PublicationsPDF/2013/BrinkerDipCoating 2013.pdf.

[6] Niranjan Sahu, B. Parija and S. Panigrahi, Indian Journal of Physics, 83 (2009) 493.

[7] M. B. Sahana, C. Sudakar, C. Thapa, G. Lawes, V. M. Naik, R. J. Baird, G. W. Auner, R. Naik and K. R. Padmanabhan, Materials Science and Engineering B, 143 (2007) 42.

[8] T. Maruyama and K. Fukui, Thin Solid Films, 203 (1991) 297.

[9] H. L. Chen, H. F. Lee, W. C. Chao, C. I. Hsieh, F. H. Ko and T. C. Chu, Journal of Vacuum Science and Technology B, 22 (2004) 6.

[10] M. Mizuhashi, Thin Solid Films, 70 (1980) 91.

[11] F. C. Eze, Materials Chemistry and Physics, 89 (2005) 205.

[12] Y. Shigesato,Y. Hayashi and T. Haranoh, Applied Physics Letters, 61 (1992) 73.

[13] S. A. Agnihotri, K. K. Saini, T. K. Saxena, K. C. Nagpal and S. Chandra, Journal of Physics D-Applied Physics, 18 (1985) 2087.

[14] www.nanofab.ualberta.ca/wpcontent/uploads/2009/03/choosingsputteringetc.pdf.

[15] www.sc.mahidol.ac.th/scpy/courses/scpy663/lecture3_evaporation.pdf.

[16] Cho A. Y. and Arthur J. R., Progress in Solid State Chemistry, 10, 3 (1975) 157.

[17] www.eeeguide.com/molecular-beam-epitaxy.

[18] www.rci.rutgers.edu/~dbirnie/solarclass/MBEgrowth.pdf.

[19] Fernando Rinaldi, Annual Report (2002) Optoelectronics Department, University of Ulm.

[20] P. Frigeri, L. Seravalli, G. Trevisi, and S. Franchi, Comprehensive Semiconductor Science and Technology (2011) Elsevier.

[21] Robert Eason, Pulsed Laser deposition of thin films (2007) Wiley-Interscience.

[22] M. Grundmann, H. Wenckstern, R. Pickenhain, T. Nobis, A. Rahm and M. Lorenz, Superlattices and Microstructures, 38 (2005) 317.

[23] W. R. Grove, Philosophical Transactions of the Royal Society of London, 142 (1852) 87.

[24] Dengyuan Song, Dirk-Holger Neuhaus, James Xia and Armin G. Aberle, Thin Solid Films, 422 (2002) 180.

[25] P. F. Carcia, R. S. McLean, M. H. Reilly, Z. G. Li, L. J. Pillione and R. F. Messier, Journal of Vacuum Science and Technology, 21 (2003) 745.

[26] L. R. Damiani and R. D. Mansano, Journal of Physics: Conference Series, 370 (2012) 012019.

[27] K. B. Sundaram and A. Khan, Journal of Vacuum Science and Technology, 15 (1997) 428.

[28] G. Kiriakidis, M. Suchea, S. Christoulakis, and N. Katsarakis, Reviews on Advanced Materials Science, 10 (2005) 215.

[29] R. A. Baragiola, Philosophical Transactions of the Royal Society of London A, 362 (2004) 29.

[30] V. S. Smentkowski, Progress in Surface Science, 64 (2000) 1.

[31] K. Yim and C. Lee, Crystal Research Technology, 41, 12 (2006) 1198.

[32] P. J. Kelly and R. D. Arnell, Vacuum, 56 (2000) 159.

[33] I. Baia, M. Quintela, L. Mendes, P. Nunesa and R. Martins, Thin Solid Films, 337 (1999) 171.

[34] D. Depla and S. Mahieu, Reactive Sputter Deposition, 109 (2008) Springer.

[35] Sigmund, Physical Review, 184 (1969) 383.

[36] M. S. Hwang, H. J. Lee, H. S. Jeong, Y. W. Seo and S. J. Kwon, Surface and Coating Technologies, 171 (2003) 29.

[37] J. E. Mahan and A. Vantomme, Journal of Vacuum Science and Technology, 15 (1997) 1976.

[38] S. Mahieu, P. Ghekiere, D. Depla and R. De Gryse, Thin Solid Films, 515 (2006) 1229.

[39] K. Van Aeken, S. Mahieu and D. Depla, Journal of Physics D-Applied Physics, 41 (2008) 205307.

[40] S. Mahieu and D. Depla, Applied Physics Letters, 90 (2007) 121117.

[41] A. Anders, Surfaces & Coatings Technology, 200 (2005) 1893.

[42] Krishna Seshan, Handbook of thin film deposition processes and techniques (2002) William Andrew Publishing.

CHAPTER 3

CHARACTERISATION TECHNIQUES

3.1 Structural analysis

The most inevitable characteristics to be studied, following the synthesis of any material is its crystalline and molecular structure. It is relevant since the periodic arrangement of atoms and molecules in the material describes its electrical and optical properties. The most significant method for determining the structure experimentally is X-ray diffraction (XRD).

3.1.1 X-Ray Diffraction

This non-destructive, basic structural analytical method was first developed by Bragg in 1913, for studying unit cell dimensions and phase identification of powdered crystalline materials. The most important advantage of this method is that it is faster and requires very less quantity of sample.

X-rays are generated in a cathode ray tube by heating a filament that produces electrons by applying voltage. These electrons are accelerated and impinged on a target material. Electrons having sufficient energy to knock out inner shell electrons of the target material produce characteristic X-rays. When a sample is hit with X-rays, it will either get transmitted, or scattered by the electrons of the atoms in the material. The scattered waves destructively interfere with each other, except at certain orientations at which Bragg's law ($n\lambda = 2d \sin \theta$) is satisfied, where they get constructively interfered. This law relates the wavelength of electromagnetic radiation to the diffraction angle θ and the lattice spacing d in a crystalline sample. Since the samples are likely to be randomly oriented, it is possible to detect all probable diffraction directions of the lattice by scanning the sample through a range of 2θ angles. The results are obtained graphically as a set of peaks with percentage intensity on the Y-axis and 2θ angle on the X-axis. Figure 3.1(a) gives a schematic illustration of how the X- rays get diffracted from a sample and figure 3.1(b) shows the inside view of X-ray diffractometer.

A given material produces characteristic diffraction pattern, if it is present in pristine or compound state. The specific crystal structure and lattice spacing determines the unique set of angles and peak intensities of the observed diffraction

pattern. Hence the graph can be used to identify the exact phases present in the sample [1-3].

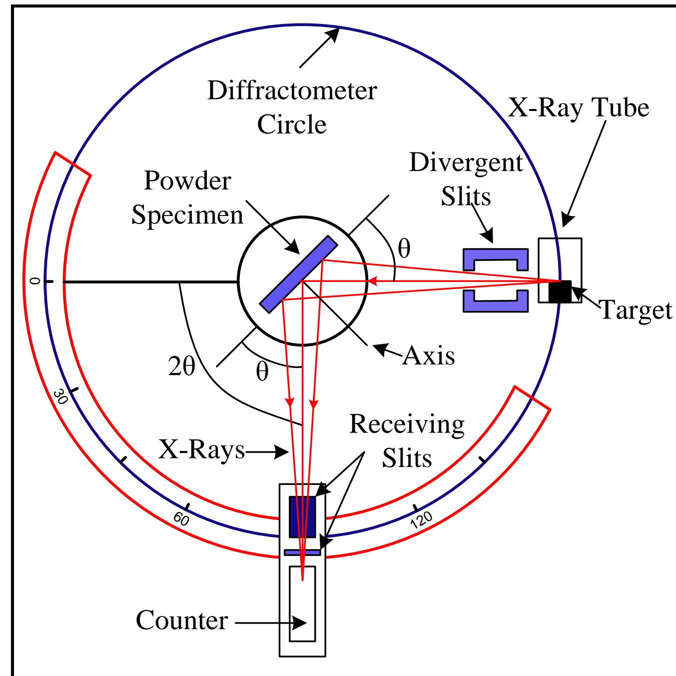

Figure 3.1(a) Schematic illustration of diffraction process and (b) Internal view of the X-ray diffractometer

If the crystal structures of all phases are not known, in a mixture of two or more phases, the phase fractions can be accurately studied using this method. Also, for an unknown material, if a similar material exists with a known structure, then the crystal structure can be determined with a high level of accuracy. This method is applicable to polycrystalline powder phases as well as films grown on a substrate [4]. The average grain size of the film can be found using Scherrer formula [5] given by,

$$d = \frac{0.9\lambda}{\beta \cos\theta} \ldots\ldots\ldots\ldots\ldots\ldots..(3.1)$$

where λ is the wavelength of X-ray used, β is the full width at half maximum intensity in radians and θ is the diffraction angle. The lattice parameter values for different crystallographic systems can be calculated using (hkl) planes and inter-planar spacing, d.

In this study, we have employed Rigaku Miniflex 600 X-ray diffractometer with Cu Kα (λ= 1.542 A^0) radiation, operating at 40 kV and 15 mA. Cu target and graphite monochromator were used and data recorded in continuous scan mode from 10^0 to 80^0, in step size of 0.02^0 and scan speed of 10^0 per minute. The XRD pattern was analysed using PDXL software. The diffraction patterns obtained experimentally were compared with standard diffraction data published by International Centre for Diffraction Data (ICDD).

3.1.2 Transmission Electron Microscopy

Transmission Electron Microscope (TEM) has emerged as an indispensible apparatus in materials research, due to the high lateral spatial resolution (better than 0.2 nm). It is also capable of delivering sample images as well as crystallographic information through diffraction. This technique utilizes highly energetic electron beam, which interacts with matter to generate radiations characteristic to a particular material. It can be used in characterisation techniques such as energy dispersive spectroscopy, electron energy loss spectroscopy, backscattered and secondary electron imaging etc. [6]. In TEM, a highly focused beam of electrons is made incident on the sample and signal attained from the electrons that penetrate the sample thickness are focussed using a series of magnetic lenses and detected using a detector, usually a fluorescent screen.

Significant amount of magnification is facilitated in a TEM by the smaller wavelength of incident electrons, which is responsible for the unique potential related to TEM. It provides mainly, two modes of sample observation - diffraction mode and imaging mode. In the first one, an electron diffraction pattern from the sample is acquired from the area illuminated on to a fluorescent screen. The diffraction pattern obtained in a TEM is commonly known as selected area electron

diffraction, SAED and is analogous to that obtained from X-ray diffraction. If the sample observed is a single crystal, it produces a characteristic spot pattern on the screen, a poly crystal creates a ring pattern and an amorphous sample produces a progression of diffused circles [7].

SAED patterns are helpful in determining the lattice parameters of crystalline materials, similar to XRD. Each diffraction angle is measured and an associated inter-planar atomic spacing *d* is determined using Bragg's law [4]. The crystal group or Bravais lattice of an unknown material can be determined easily using this method, employing similar indexing procedures as in XRD.

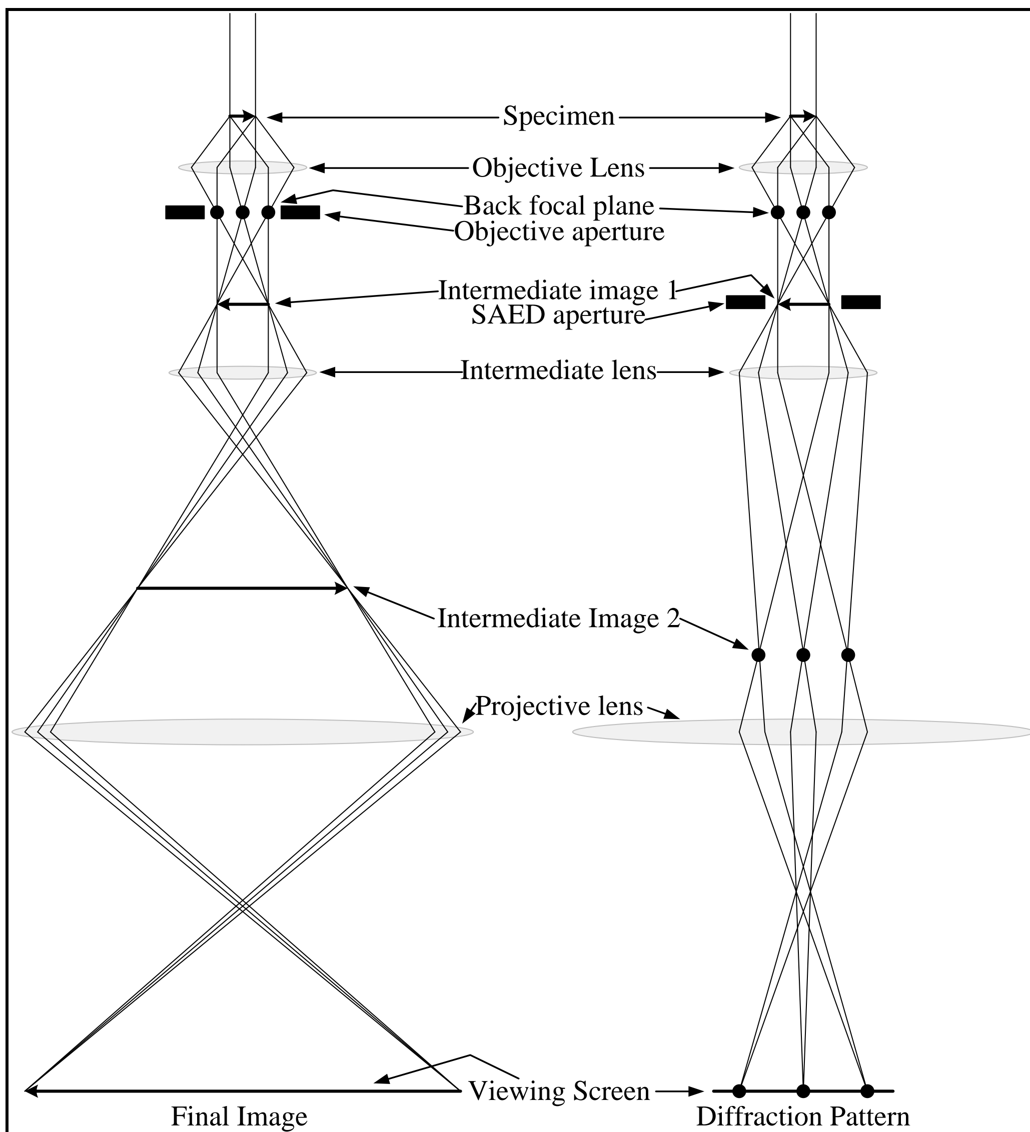

Figure 3.2 Schematic diagram of the electron path in a TEM

In image mode, transmitted signals are detected at the image plane of objective lens and the scattered electron wave forms an image with identifiable information associated with the microstructure of the specimen under investigation. Figure 3.2 is a schematic diagram of the electron paths in TEM equipment in the image and diffraction mode.

In our study, we have used high resolution Jeol/JEM 2100 TEM equipped with a high-stability goniometer for elevated tilt tomographic applications. The source used was LaB_6 at a voltage of 200 kV. The camera length being 80-2000 mm, the magnification of 2,000x to 15,00,000x was achievable with this instrument.

3.2 Spectroscopic analysis

3.2.1 X-ray Photoelectron Spectroscopy

X-ray photoelectron spectroscopy (XPS) is a quantitative analytical technique that measures the surface chemistry of the material and is used for analysing the elemental constituents, composition of chemical states, depth profile and thickness of thin films [8]. It can also provide information regarding the charge of ions within the material, and can be useful in determining the physical structure of the material. XPS is based on photoelectric effect, proposed by Einstein in 1905 as the ejection of electrons from a surface when photons impinge upon it. This process can be expressed by the following equation,

$$E_{binding} = E_{photon} - (E_{kinetic} + \phi) \quad (3.2)$$

where $E_{binding}$ is a function of the type of atom and its environment, E_{photon} is the energy of photon from the X-ray source, $E_{kinetic}$ is the kinetic energy of the emitted electron, measured using spectrometer and ϕ is the work function [9]. As the initial X-ray photon energy is known, it is possible to calculate the binding energy of each electron using the above equation. XPS technique is highly surface specific due to the short range of the photoelectrons that are excited from the solid. Al Kα (1486.6 eV) or Mg Kα (1253.6 eV) are often used as the photon energies. In certain cases, Ti Kα (2040 eV) is also used.

Due to photoelectric effect, this irradiation causes emission of electrons from the sample, which is directed towards a detector, where an analyzer determines the

energy of these photoelectrons and this gives a continuum with a series of photoelectron peaks. A typical XPS spectrum is a plot of the number of electrons detected versus binding energy of electrons detected [10, 11]. The photoemission process is shown in figure 3.3, where an electron from the K shell (1*s* electron) is ejected from an atom. The binding energy of electrons is characteristic of each element [12]. Peak shifting can be caused by shared electrons in covalent bonds as well as variations in ionic charge.

The peak areas can determine the composition of material surface. The chemical state of emitting atom can slightly vary peak shape and binding energy, and hence information about chemical bonding of the material can also be obtained [13, 14]. The resulting curve can be analysed by comparing it with existing data, but is most commonly analysed using peak fitting software. Peak indexing can be done using the XPS database [15].

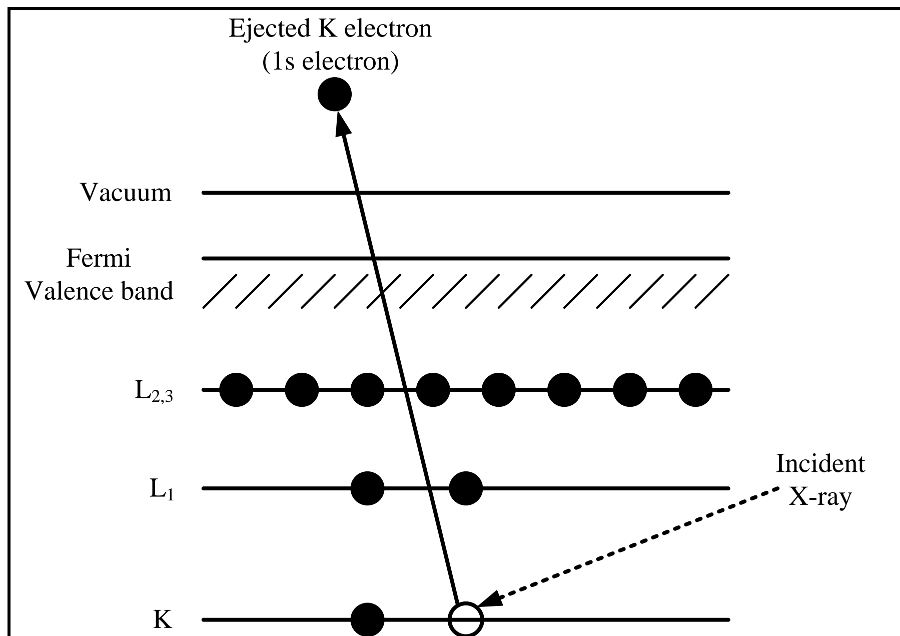

Figure 3.3 Schematic diagram of the photo electron emission process

The data of all constituent elements of the film can be collected from the survey scan spectrum. XPS is not sensitive to hydrogen and helium, but can detect all other elements. It requires ultra-high vacuum conditions, and is used to analyze

inorganic compounds, metal alloys, semiconductors, biomaterials, etc. The number of detected electrons in each of the characteristic peaks is directly related to the amount of element within the area irradiated. The number of peaks in the spectrum decides the number of occupied energy levels in the atoms whose binding energies are lower than X-ray energy. The position of peaks directly measures binding energy of electrons in the orbitals and identifies the atoms concerned [7]. Shape of the peak provides vital information regarding electronic state of elements in the compound, additional energy levels, error estimation, binding energy shift and orbital energy level splitting.

In this work, X-ray photoelectron spectra of thin film samples were obtained from high resolution AXIS Ultra model XPS system from Kratos Analytical Pvt. Ltd., U.K., equipped with Al Kα source. Energy drift due to charging effects was calibrated, taking Carbon 1*s* (285.4 ± 1eV) core-level spectrum. The error estimation, peak fitting and orbital energy level splitting observed in the spectrum, full width at half maxima (FWHM), binding energies, area of the peaks and the energy difference between peak maximas were obtained using CASA XPS and PEAKFIT-41 software. The binding energies and their shifts were evaluated by National Institute of Standards and Technology (NIST) database.

3.2.2 UV- Visible Spectroscopy

In UV-Visible spectrophotometer, a beam of light is split into two: one is directed through a transparent cell containing the thin film sample to be analyzed, and the other one is directed through an identical cell without any coating, which serves as the reference beam. The intensities of these two beams are compared, as it scans over a particular wavelength. If the sample absorbs light at a particular wavelength, intensity of sample beam will be less than that of reference beam and rest of the beam is transmitted through it [7]. Percentage of transmission of beam through a sample is measured at various wavelengths and plotted by a recorder to obtain the spectrum, which is a plot of wavelength of the entire region versus transmittance (T) of light at each wavelength. The schematic diagram of a UV-Visible spectrophotometer is shown in figure 3.4. The UV spectrum ranges from 100 to 400 nm and both UV and visible radiation are of higher energy than IR radiation

[16]. Absorption of ultraviolet or visible light results in electronic transitions, that is, electrons are shifted from lesser energy state orbitals to higher energy excited state orbitals. In a semiconductor, absorption of a photon across the band gap is significant and UV/Visible spectroscopy is one of the best methods to investigate it. This technique measures different percentages of light reflected, transmitted or absorbed by samples in the form of solutions, powders, thin films and crystals. Since it is very difficult to obtain transmitted light in powders and solids, diffused radiation reflected from the surface is measured in such samples. This technique is known as diffuse reflectance spectroscopy (DRS).

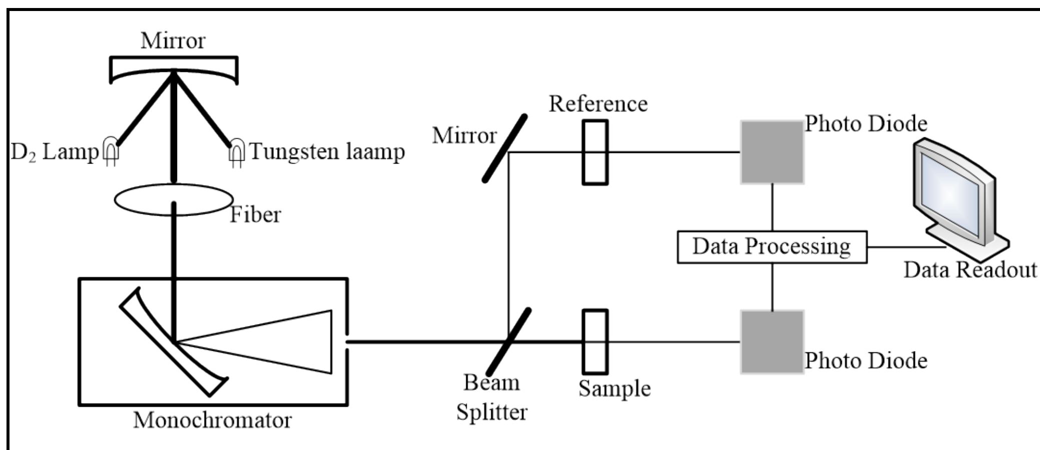

Figure 3.4 Schematic diagram of UV - Visible spectrophotometer

When the incident photon energy ($h\nu$) is larger than band gap energy (E_g), the valence band electrons get excited to the conduction band empty states, causing absorption of light by the sample and generation of electron hole pairs. The number of electron hole pairs created is linearly proportional to the number of incident photons per unit area, unit time and unit energy. The frequency ν is related to the wavelength λ by the relation,

$$\lambda = c/\nu \text{ ....(3.3)}$$

where c is the velocity of light. The absorption coefficient (α) is determined by the absorption process in semiconductors and k is the extinction coefficient, given by,

$$\alpha(\nu) = 4\pi k\nu/c \text{ ....(3.4)}$$

For parabolic band structure, the relation between the absorption coefficient (α) and the band gap (E_g) of the material is given by,

$$\alpha h\nu = A\,(h\nu - E_g)^r \quad \text{..(3.5)}$$

where r = 1/2 for allowed direct transitions,

r = 2 for allowed indirect transitions,

r = 3 for forbidden indirect transitions and

r = 3/2 for forbidden direct transitions.

A is the parameter which depends on the transition probability.

This method is predominantly useful for probing the valence band and to determine the band gap and material surface work function. The absorption coefficient can be deduced from absorption or transmission spectra using the relation,

$$I = I_0\, e^{-\alpha t} \quad \text{..(3.6)}$$

where I is the intensity of transmitted wave, I_0 is the intensity of the incident light and t thickness of the film. For direct transitions, $(\alpha h\nu)^2$ will show a linear dependence on the photon energy ($h\nu$) and hence a plot of $(\alpha h\nu)^2$ against ($h\nu$), known as Tauc plot, will be a straight line. An intercept on the energy axis at $(\alpha h\nu)^2$ equal to zero will give the band gap energy [17-18]. The optical properties of TCOs are significant while analyzing its performance. In this work, we studied the optical behaviour of thin film TCOs and the band gap of these sputtered films were estimated by recording transmission spectrum in the wavelength range of 200-900 nm using Jasco V-550 UV-Visible spectrophotometer. From the transmission spectra, using Swanepoel method, various optical constants of thin films such as index of refraction, thickness of coating, absorption and extinction coefficient etc. can be calculated, if the film transmission spectra exhibit interference patterns [18]. The refractive index (n) at different wavelengths can be calculated using envelope curve of maximum transmittance (T_{max}) and minimum transmittance (T_{min}) in the transmission spectra. The expression for refractive index is given by,

$$n = [N + (N^2 - {n_s}^2)^{1/2}]^{1/2} \quad \text{..................(3.7)}$$

$$\text{where } N = 2n_s\left[\frac{T_{max} - T_{min}}{T_{max} \cdot T_{min}}\right] + \frac{{n_s}^2 + 1}{2} \quad \text{...........(3.8)}$$

and ns is the index of refraction of the substrate (ns =1.54 for quartz). The thickness of the films were calculated from the equation as given below, using the value of refractive indices obtained.

$$t = \frac{\lambda_1 \lambda_2}{2[n_1 \lambda_2 - n_2 \lambda_1]} \qquad (3.9)$$

3.2.3 Energy Dispersive Spectroscopy

Energy dispersive spectroscopy (EDS) is a procedure to measure intensity of X-ray emission as a function of the energy of X-ray photons. The X-ray intensity can be related to the concentration or atomic fraction, by performing physical/empirical matrix corrections [4]. Using current detectors, most EDS systems are capable to detect X-rays from all elements in the periodic table above Beryllium. The least quantitative assessment that can be performed by a typical EDS system, known as minimum detection limit (MDL) for elements with atomic numbers greater than 11 is as low as 0.02% wt., if the peaks are isolated; and the accuracy of quantitative analysis has been reported to be better than 2% [7]. EDS systems are mainly used in electron column instruments such as scanning electron microscope (SEM), transmission electron microscopes (TEM) and electron probe micro analyzer (EPMA).

Since X-ray generation depends on electrons in the material, preference of accelerating voltage is determined by the nature of sample under analysis. For thin films, it is desirable to minimize the electron range and an accelerating voltage slightly higher than the critical ionization voltage for the X-ray is preferred. Since the MDL for most elements is 100-200 ppm, an EDS system can detect even a monolayer of thin film, using Kα lines at moderate accelerating voltages of 5 to 15 keV.

Energy dispersive X-ray spectroscopy is used for quality control and constituent analysis in many industries including semiconductors, metals, cements, papers and polymers. The main advantages of this technique are its fast data collection, analytical and geometrical efficiency of detectors, portability and the relative ease of interfacing to data interpretation equipments. A schematic

demonstration of the EDS system is given in figure 3.5. A major advantage of this system is that it can be placed very close to the sample and present a large solid angle for collecting the emitted X-rays.

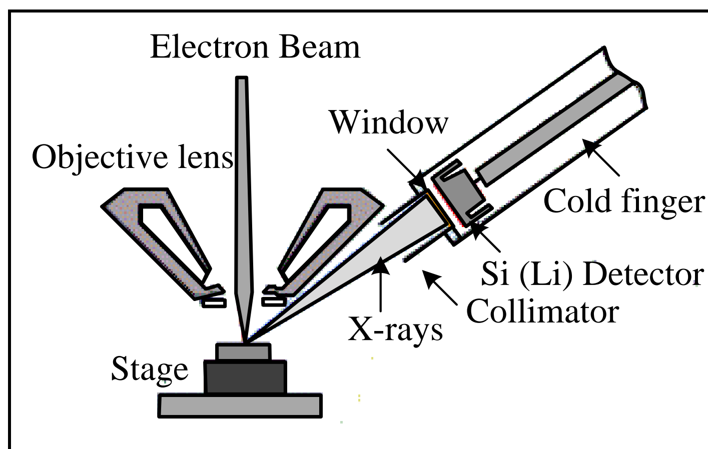

Figure 3.5 Schematic diagram of Energy Dispersive Spectrometer

The major aim behind the usage of an EDS analytical system is to have the capability of measuring the concentrations of all elements in the sample. The peak intensity obtained for each element in the sample is compared to that obtained from a reference standard using the same operating conditions and a qualitative survey of the elements present can be made [7]. EDS works on the basic principle of Moseley's Law, which states that the energy of a particular radiation within a series of emission lines ($K\alpha$, $K\beta$ lines) varies consistently with atomic number of the elements.

$$E = C_1 (Z - C_2)^2 \quad (3.10)$$

where E is the energy of emission line for a given X-ray series, Z is the atomic number of the emitter and C_1 and C_2 are constants. If the value of energy of a particular K, L or M emission line is determined, the atomic number of the species generating that particular emission line can be calculated. The K, L and M X-ray emission lines increase in energy with increasing atomic number. In this work, EDS spectra of the samples were obtained from Horiba EMAX instrument and the elemental compositions were confirmed.

3.3 Surface morphology analysis

3.3.1 Scanning Electron Microscopy

Scanning electron microscopy (SEM) provides the user with a highly magnified illustration of a material surface, which is exactly same as what one would actually "see" visually at the surface [7]. It simplifies surface topography interpretations to a large extend. Modern SEM systems can operate at magnifications from about 3X to 150000X and the resolution can be a few nano meters. At high vacuum, an electron source is focussed into a fine probe that moves over the surface of the sample in a raster scan pattern. When the electron beam strikes the surface and penetrates it, a number of interactions occur resulting in the emission of electrons from the surface. These are collected by appropriate detectors and image construction is accomplished by mapping its intensity onto a viewing screen or film. The images obtained by SEM are mainly of three types: secondary electron image (SE), backscattered electron image (BSE), and elemental X-ray image. Secondary and backscattered electrons are typically classified based on their energies [7]. For both images, the yield increases by decreasing the incident glancing angle, since more scattering occurs nearer to the surface. Another significant electron interaction occurs in SEM when incident electrons collide and eject a core electron from an atom. When this atom in excited state comes to ground state, it emits either a characteristic X-ray photon or an Auger electron, characteristic to the elements [19]. The schematic diagram of the electron path in a SEM is shown in figure 3.6.

Sample preparation procedure is effortless in SEM, compared to transmission electron microscopy (TEM), provided, the sample is vacuum compatible. Also, the sample needs to be conducting or else, it has to be coated with a thin conducting film of carbon, gold, or any other metal of about 10 nm thickness. For metal samples coated with an oxide layer, a higher accelerating voltage should be used to improve the quality of image, since high-energy beam is impinged on the oxide, it can create electron-hole pairs in adequate numbers in order to set up local conduction [20]. This phenomenon is often observed while studying semiconductor devices passivated with thin oxide deposited films. In recent SEM systems, the

energy of incident electron beam can range from a few hundred electron volts to about 30 keV. It can also provide crystallographic information. Grain size and shape of individual grain structures on the surface can be identified clearly, and hence this method is significant for micro-structural analysis. The topographical features, morphology, phase distribution, compositional differences, crystal structure, crystal orientation, and the presence and location of structural defects can be identified using this analytical technique [7].

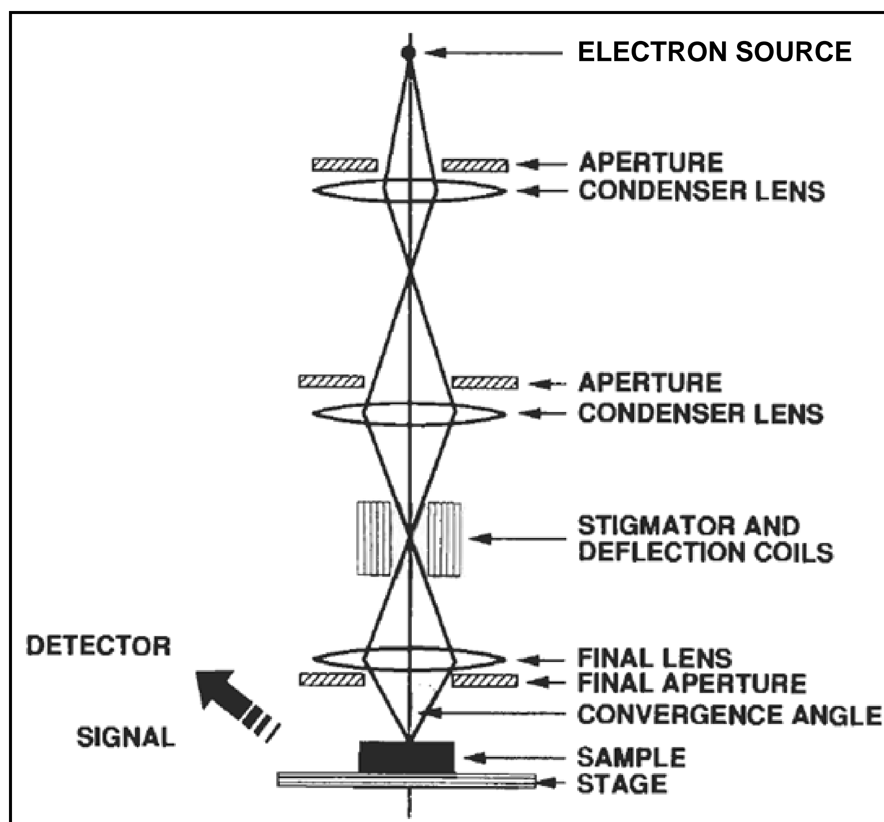

Figure 3.6 Schematic diagram of the electron path in a scanning electron microscope

Depth of field is the property of this method, by which surfaces at different distances from the lens are focussed, which gives a three dimensional information about the image. SEM has 300 times the depth of field than the normal light microscope. Focusing of electron beam is accomplished using electromagnetic or electrostatic fields, which focus the electrons into a small area, thus reducing the diameter of electron beam produced by the electron gun [21].

The field emission scanning electron microscope (FESEM) is significant due to the enormous impact on the field and the electron gun allows for the creation of an exceptionally bright and small high current density electron beam. Also, FESEM is capable of producing a small probe diameter at low voltage, difficult to attain with conventional thermionic electron guns, catering to the needs of various applications [4]. In this work, we have obtained SEM images from Hitachi 0066, equipped with a Schottkey electron gun and ultra high resolution Zeiss Gemini SEM. Cross sectional SEM images were also obtained to study the morphology of the interface and coatings of the sputtered films.

3.3.2 Atomic Force Microscopy

Atomic Force Microscope (AFM) is a high-resolution, three-dimensional profilometer, also called a Scanning Force Microscope (SFM). It can achieve extremely high magnifications up to 1000000X, analogous or even superior to electronic microscopes. The measurement is made in three dimensions; X-Y plane horizontally and Z dimension vertically. It can determine the force between the top surface of a sample and a sharp cantilever probe tip [7]. Scanning is done in a raster motion, controlled by piezoelectric tubes. When the tip to sample distance is of the order of a few angstroms, a predominant repulsive force appears between the probe tip and the atoms on the sample surface. This is mainly due to the exchange interactions by the overlap of electronic orbitals. At this stage, the tip and the sample are considered to be in the contact mode.

The surface topography can be evaluated, if the force is determined as a function of the position of the sample. In this versatile technique, the cantilever tip is placed in contact with the sample and detection is done optically by interferometry or beam deflection [4]. Scanning can be done in three different modes namely contact, non-contact and tapping mode. In the contact mode, deflection of cantilever is kept constant and this mode can damage samples or distort image data, since it is subjected to frictional and adhesive forces. In the non-contact mode, probe tip oscillates at resonance frequency where, the oscillation amplitude is kept a constant. The resolution is less in this mode and the presence of any contaminant such as water can interfere with oscillation and possibly hamper the images. Tapping mode

is a combination of contact and non-contact mode and takes advantages of both. In this mode, the tip comes into contact with the sample surface intermittently, thereby eliminating the frictional forces and oscillating with adequate amplitude to prevent the adhesive forces of the contaminant layer from trapping the probe tip.

Conducting as well as insulating materials can be analyzed without much sample preparation. The depth of grain boundaries can be determined from a 3D image and surface roughness can be calculated. Inter atomic forces between atoms on the sample surface and atoms on the probe tip cause deflection of the cantilever. Since magnitude of cantilever deflection depends on the distance between the surface and tip atoms, this method can be used to map the sample topography with atomic resolution [14].

Spatial resolution of an AFM is typically few nano meters for scans up to 130 pm. The standard deviation of surface height profile from the average height is known as root mean square roughness and can be directly computed using interfacing software [22]. The schematic of an AFM system is shown in figure 3.7(a) and 3.7(b) is the photograph of AFM equipment. In this work, the surface probing was done using Park XE 70 instrument in non-contact mode. Values of root mean square (RMS) roughness were calculated from the height values in the images using AFM data analysis XEI commercial software.

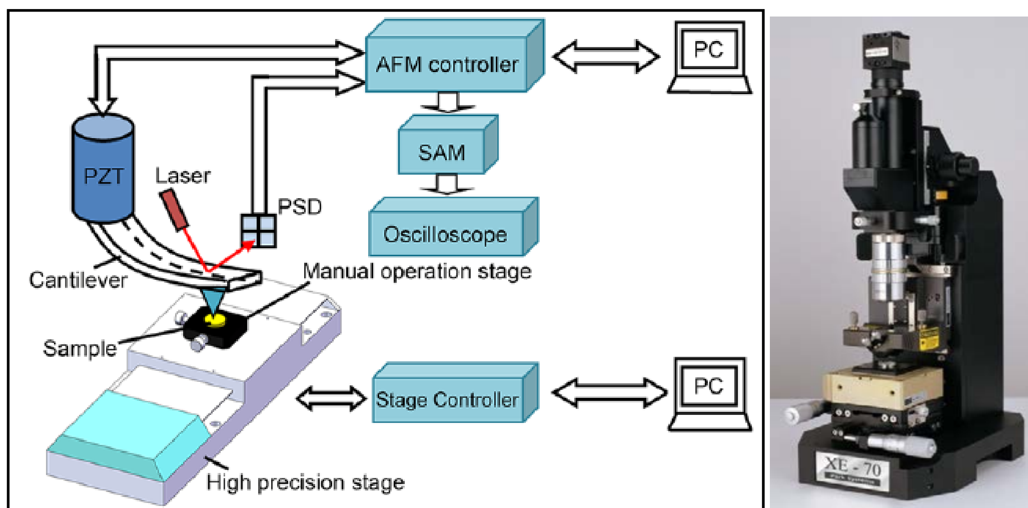

Figure 3.7(a) Schematic diagram of atomic force microscope unit and (b) Photograph of AFM equipment

3.3.3 Optical Profilometry

Optical profilometry (OP) is a method for studying the surface topography of thin film samples in non-contact mode. This is based on principles of interferometry and provides 2D and 3D images of the sample under investigation. Incident light that falls on the sample surface gets reflected and interferes with light from an optically flat reference sample. The divergence in fringe pattern generated by interference of light is measured and it corresponds to surface roughness profile of the sample. The beam of light in the interferometer is shifted to compute the variations [7].

Dimensional analysis, roughness studies and thickness measurement of transparent films, which are difficult to perform using other methods, can also be performed using an optical profilometer. A line scan is generated similar to a mechanical profiler and the average roughness is determined using computer interfaced software, using the stored data points from the line scan. A 3D depiction adds considerably to the information provided about the surface. Sample analysis is quite easy and no prior preparations are necessary. Also the data acquisition time is very less. But if the surface is very rough (>1.5 pm), the interference fringes will be highly dispersed and hence the topography cannot be resolved [4].

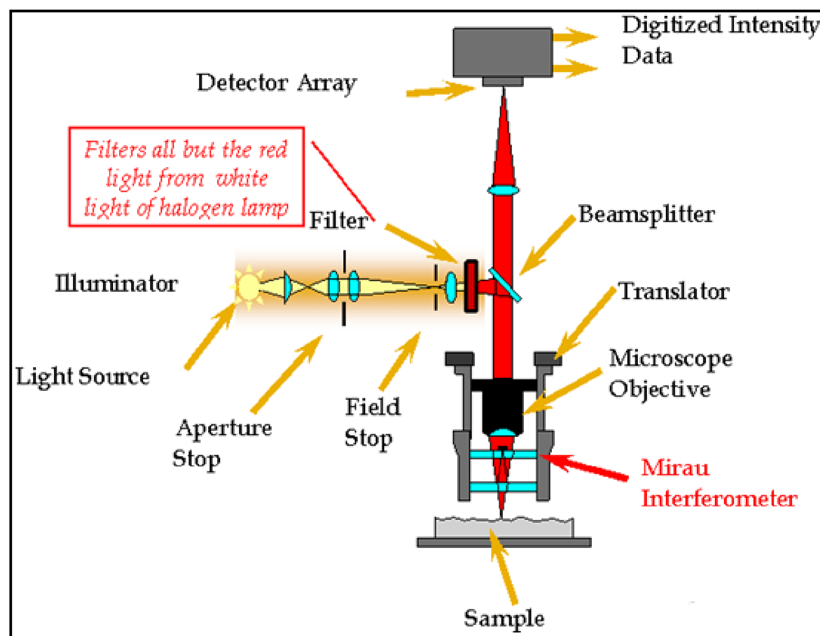

Figure 3.8 Schematic representation of a non-contact optical profilometer

If the sample under investigation comprises of more than one film on a substrate or if the film is completely transparent to the wavelength corresponding to the measurement system, errors are likely to be introduced. But such films may be investigated using advanced software, if there are differences in the refractive index of the film and substrate. Multiple coatings can be studied if coated with an intermediate layer which is opaque to the wavelength of measurement system used [23]. Figure 3.8 shows the schematic representation of an optical profilometer.

In this work, we have used Taly Surf CCI sub-nanometric 3 dimensional non-contact optical profiling for surface morphology analysis of sputtered thin films. It has the capability to scan surfaces with a Z resolution of 0.01 nm together with a 0.4 nm lateral resolution with 1048 x 1048 pixel array for large field of vision with high resolution.

3.4 Electrical property analysis

3.4.1 Hall effect

The electrical and electronic property measurements of a material can reveal its electrical transport behaviour, which in turn yields information about carrier concentration, nature of charge carriers, mobility and scattering mechanisms. Hall measurement is considered to be one of the most versatile techniques that can yield information about all these properties, all of which affect the conductivity of the material. Also, ionisation energy of dopants and band structure of semi conductor can be calculated using this technique.

It was in 1879 that Edwin Hall discovered the phenomenon of Hall effect, which eventually turned out to be one of the most valuable tools for material characterization [4]. An electric field is developed in a conductor on the application of a magnetic field perpendicular to the direction of current flow. The developed voltage is called Hall voltage and the phenomenon is called Hall effect. Ohmic contacts of silver are made at the corners of a 1 cm^2 thin film (figure 3.9) and a series of measurements are conducted.

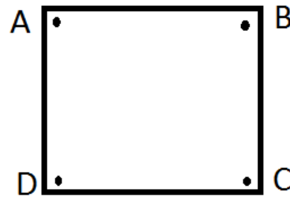

Figure 3.9 Van der Pauw Hall measurement sample

If R_1 is the potential difference between A and B per unit current through C and D and R_2, that between B and C per unit current through D and A, sheet resistance R_s is calculated as:

$$R_s = \left(\frac{\pi}{ln(2)}\right)\frac{(R_1 + R_2)}{2} f\left(\frac{R_1}{R_2}\right) \quad (3.11)$$

where $f(\frac{R_1}{R_2})$ is the Van der Pauw function, given by

$$f\left(\frac{R_1}{R_2}\right) = 1 - 0.3466\left(\frac{R_1 - R_2}{R_1 + R_2}\right) \quad (3.12)$$

To measure resistivity, a predetermined current is applied between two adjacent contacts. Voltage drop is measured across a diagonal pair of contacts. By repeating the measurements using next pair of contacts, all four possible configurations are measured [24]. This is repeated by reversing the polarity. The electrical resistivity of a semiconductor thin film can be written using Ohm's law,

$$\rho = \frac{1}{en\mu} \quad (3.13)$$

where ρ is the film resistivity, e is the electronic charge, n is the number of carriers corresponding to the carrier concentration and μ is the carrier mobility.

The sample is placed in a perpendicular magnetic field of known value to measure carrier concentration, and a predetermined current is passed between a pair of diagonal contacts and voltage is measured. By increasing the carrier concentration or mobility or both, low resistivity can be achieved. Increase in carrier concentration beyond certain value results in decrease in mobility due to scattering of charge carriers. Hence an optimum value of carrier density and mobility has to be maintained for achieving low resistivity. The underlying principle of this method is the Lorentz force: the force on a point charge owing to electromagnetic fields. The

direction of force on a charge carrier can be determined using right hand rule, with respect to its direction of motion and that of the applied magnetic field.

According to Ohm's law the carrier mobility affects resistivity. The technique works by measuring the voltage induced by carrier detection, which is caused by Lorentz force resulting from the interaction of external magnetic field applied perpendicular to the plane with applied electric current and measured voltage. Measurement of Hall voltage enables calculation of the film carrier density, which can be converted into bulk carrier concentration by dividing the result by the sample thickness.

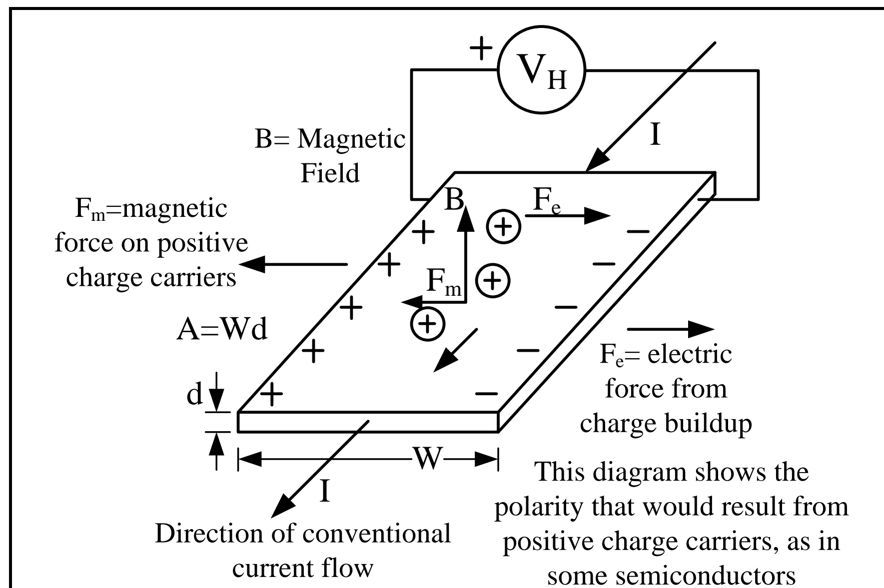

Figure 3.10 Schematic diagram of Hall measurement set up

The Hall coefficient R_H gives the nature of charge carriers; a negative value of R_H corresponds to *n*-type carriers (electrons) and positive value to *p*-type (holes). It can be calculated as $R_H = \rho\mu$ [25].

In our study of thin films, the resistivity of thin films ρ, carrier concentration n, and carrier mobility μ were measured using four point probe in the Van der Pauw configuration. The thin film samples used were 1cm x 1cm in size. Silver paste was applied at the corners of the sample symmetrically. The Hall measurements were taken using Ecopia Hall measurement system, HMS 3000.

3.4.2 I-V characteristics

A semiconductor *p-n* junction forms the fundamental component of many commercially significant devices such as bipolar junction transistors, hetero junction transistors, junction field-effect transistors, zener diodes, rectifying diodes etc. The current-voltage (I-V) measurement is significant for characterisation of semiconductor devices, since complementary techniques do not provide enough information whether the material can operate as required in a semiconductor device.

Some of the parameters usually measured for a *p-n* junction are built-in voltage, the ideality factor for a forward-biased junction, and reverse-biased breakdown voltage. The *I–V* measurement of Si diodes are generally performed in dark, but those of transparent oxide semiconductor thin film diodes can be done under normal illumination, since they are insensitive to visible light. Shockley derived the ideal diode equation with certain assumptions such as,

(1) the semiconductor is neutral as a whole and a dipole layer exists with abrupt boundaries, which defines the built-in potential and applied voltages,

(2) no recombination of electrons and holes takes place in the depletion region,

(3) minority charge carrier densities are small compared to majority charge carrier densities and

(4) the semiconductor is non-degenerate [26].

Different materials deviate from the ideal diode equation in many predictable ways. Taking all these assumptions into consideration, the equation of state has been solved for the current density, as

$$I = I_0 \left[e^{\left(\frac{qV_j}{nkT}\right)} - 1 \right] \ldots\ldots\ldots\ldots\ldots\ldots\ldots\ldots (3.14)$$

where V_j is the junction voltage, q is the magnitude of the electron charge, k is the Boltzmann constant, and T is the temperature. For positive voltage (forward-biased junction), the first term is several times greater that kT, and the current increases exponentially, when the applied voltage is greater than the built-in electric field. For negative applied voltages, the second term is several times greater than kT, and hence the reverse current reaches a constant value of I_0. For voltages above 50mV, the term -1 is usually ignored. Hence the equation can be written as

$$I = I_0\left[e^{\left(\frac{qV_j}{nkT}\right)}\right] \ldots\ldots\ldots\ldots\ldots\ldots\ldots\ldots (3.15)$$

Taking log on both sides, $ln(I) = ln(I_0) + \left(\frac{q}{nkT}\right)V_j \ldots\ldots\ldots (3.16)$

Hence, a plot of *ln (I) v/s V* of the diode give the slope as *(q/nkT)* and X-intercept gives *ln* (I_0). Thus the value of ideality factor, *n* can be calculated.

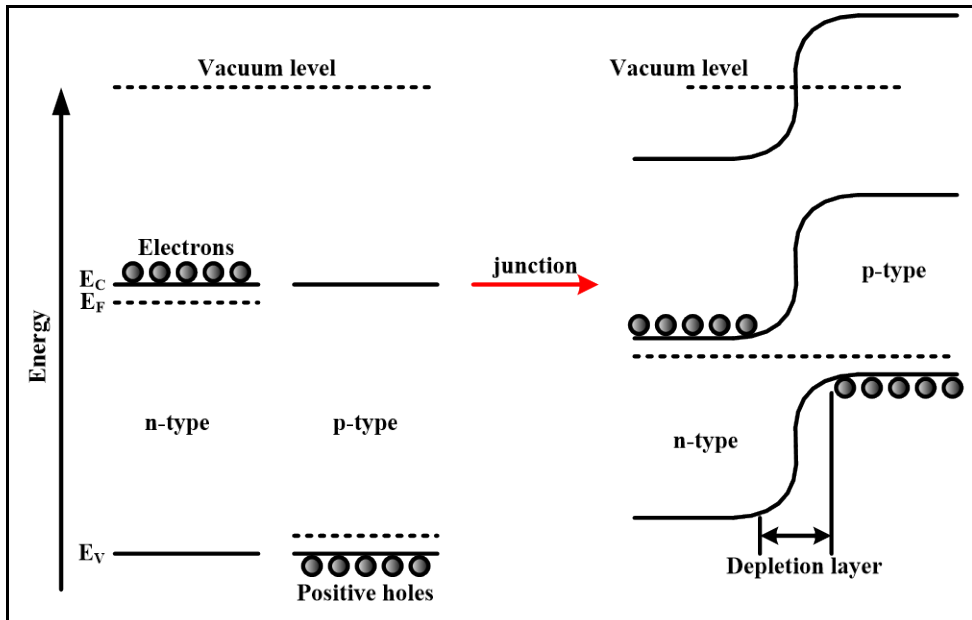

Figure 3.11 Schematic energy diagram of p-type and n-type semiconductors before junction formation (left) and of the p–n junction (right)

An electron-hole pair is generated at the junction as in figure 3.11, when a photon is absorbed and is rapidly split into *n* and *p*-type, by the applied electric field, by the phenomenon of photovoltaic effect. The amount of current flow in a *p-n* junction is determined by the polarity of applied voltage.

The equipment required for *I-V* measurement comprises of a semiconductor parameter analyzer, data collection and storage capability and a probe station. The probe contacting the *n*-electrode is grounded, and the other probe contacts the *p*-electrode. The analyzer scans the bias voltage range, and data collection software is properly initialized. The hetero interface between two layers needs to be very even for the diode to exhibit good *I–V* characteristics, since crystallographic imperfections at the interface can generate leakage currents [27]. Also, deviations of a diode from its ideal behaviour can be due to surface related currents, generation

and recombination of electrons and holes between states in the band gap and their tunnelling. Care should be taken to eliminate electrical noise by using suitable cables and giving proper grounding, since even good quality semiconductors may have reverse currents approaching the electrical noise level of the instrumentation.

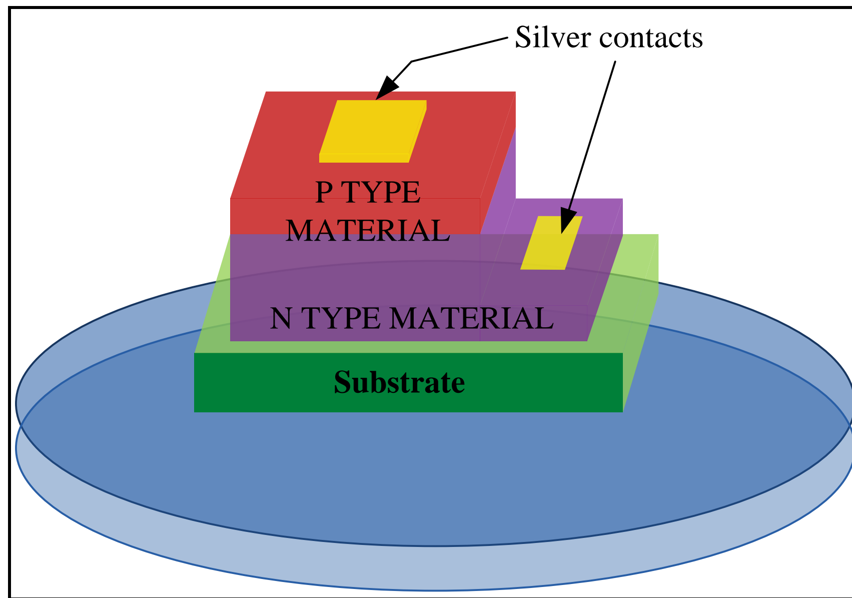

Figure 3.12 Schematic of thin film p-n junction diode

The schematic representation of a typical thin film *p-n* junction is shown in figure 3.12. *p-n* junction diodes of transparent oxide semiconductors are preferred as active devices in ultraviolet detectors, because of their wide bandgap, optical transparency in the visible and near UV-light region, environmentally benign nature, and moreover thermal and chemical stability [7]. In this work, Agilent DC probe station with voltage source units were used to measure the *I-V* characteristics of the transparent thin film hetero junction diodes.

References

[1] B. Bob, Two-dimensional X-ray diffraction (1954) John Wiley & Sons.

[2] M. M. J. Treacy and J. B. Higgins, Collections of simulated XRD powder patterns for zeolites (2007) Elsevier.

[3] M. J. Buerger, X-ray Crystallography (1962) John Wiley and Sons.

[4] E. N. Kaufmann, Characterization of Materials (2003) John Wiley & Sons.

[5] B. D. Cullity and S. R. Stock, Elements of X ray diffraction (2001) Prentice Hall.

[6] Thomas LaGrange, http://cime.epfl.ch.

[7] C. Richard Brundle, Charles A. Evans, Jr, Shaun Wilson, Encyclopedia of Materials Characterisation (1992) Manning Publications Co.

[8] J. F. Watts and J. Wolstenholme, An introduction to surface analysis by XPS and AES (2003) John Wiley & Sons.

[9] D. Briggs, Surface and Interface Analysis (1986) John Wiley & Sons.

[10] B. Vincent Crist, Handbooks of Monochromatic XPS Spectrab- Vol. I (1999) XPS International.

[11] http://www.xpsdata.com.

[12] John C. Vickerman, Surface Analysis-The Principal Techniques (1997) John Wiley & Sons.

[13] J. M. Hollander and W. L. Jolly, Accounts of Chemical Research, 3 (1970) 193.

[14] D. W. Turner, Philosophical Transactions of the Royal Society of London A, 268 (1970) 7.

[15] http://srdata.nist.gov/xps/Default.aspx.

[16] H. H. Perkampus, UV-VIS Spectroscopy and its applications (1992) Springer.

[17] A. B. Murphy, Solar Energy Materials and Solar cells, 91 (2007) 1326.

[18] John Coates and R. A. Meyers, Encyclopedia of Analytical Chemistry (2000) John Wiley and Sons.

[19] K. Robbie, L. J. Friedrich and S. K. Dew, Journal of Vacuum Science and Technology A – Vacuum, Surfaces, and Films, 13 (1995) 1032.

[20] J. I. Goldstein, Dale E. Newbury, P. Echlin, D. C. Joy, C. Fiori and E. Lifshin, Scanning Microscopy and X-Ray Microanalysis (1981) Plenum Press.

[21] D. B. Holt and D. C. Joy, SEM Micro characterization of Semiconductors (1989) Academic Press, London,

[22] Rugar D. and Hansma P., Physics Today, 43 (1990) 23.

[23] C. Y. Poon and B. Bhushan, Wear, 190 (1995) 76.

[24] J. Y. W. Seto, Journal of Applied Physics, 46 (1975) 5247.

[25] D. H. Zhang and H. L. Ma, Applied Physics A, 62 (1996) 487.

[26] Shockley W., Electrons and Holes in Semiconductors (1950) D. Van Nostrand Company.

[27] H. Kawazoe, H. Yanagi, K. Ueda and H. Hosano, MRS Bulletin, 25 (2000) 8.

CHAPTER 4

STUDIES ON *n*-TYPE TRANSPARENT CONDUCTING OXIDES

4.1 Introduction

The design of *n*-type transparent conductors with the desired structural, optical and electrical properties have been driven mostly by the enhanced importance and potential applications in the field of solid state Physics. This has resulted in new materials as well as theoretical modelling tools that provide better understanding about the behaviour of TCOs. The field of transparent conductors have been dominated historically by a set of oxides; predominantly tin oxide, zinc oxide, indium oxide, cadmium oxide and gallium oxide - generally known as the *TCO phase space*. These oxides generally have the structure with octahedrally coordinated cations and possess *n*-type electronic conductivity. Efforts are going on to include various novel oxide materials into this phase space.

In metal oxides, the metal-oxygen bond is very strong and hence they possess a combination of high heat of formation as well as wide band gap. When these materials are doped, due to Burstein-Moss shift, the optical gap is enhanced along with good conductivity, as described in Chapter 1. The process followed for deposition of materials into thin film form also has profound influence on their properties. This chapter details the fabrication of tin oxide and indium tin oxide *n*-type TCOs in thin film form by radio frequency magnetron sputtering and optimisation of deposition parameters to obtain good TCO properties. Also detailed studies on the structural, optical and electrical characterisation of these films are explained.

4.2 Fabrication of thin films by radio frequency magnetron sputtering

Magnetron sputtering technique for thin film deposition is extensively used due to its ability to control fabrication conditions and produce high purity films. Also, it is considered to be a clean and environment friendly method as the whole process is performed in a closed chamber and no poisonous gases are released into the surrounding atmosphere. Hence, this technique has been made use of in several applications including coatings with specific properties. Extensive research is going

on to study the influence of deposition parameters such as substrate temperature during sputtering, sputter power, target to substrate distance, thickness of films and gas flow rate [1-6].

4.3 Growth kinetics

The structural qualities and physical properties such as electrical and optical behaviour of films strongly depend on the process followed for its deposition. In radio frequency magnetron sputtering, there are various parameters which influence the growth of thin films. Several studies have been conducted to understand the influence of deposition parameters on the characteristics of magnetron sputtered thin films [2,3]. We shall discuss some of them in the succeeding sections.

4.3.1 Effect of sputter power

Power variation is a vital aspect to control the properties of thin films by RFM sputtering technique. Films sputtered with higher power results in larger crystallite size which may be attributed to the high ad-atom energy, and thereby resulting in the formation of crystalline films [7]. For the formation of highly crystalline films, higher power is required in magnetron sputtering system to energize argon gas and provide sufficient kinetic energy to ad-atoms, which diffuse on to the surface of substrates, causing nucleation and growth of thin films. The thickness of films and crystallite size were found to vary linearly with the sputtering power. Power also influences the film density, which in turn affects the resistivity and optical properties of films [8,9]. In our work, the sputter power was varied from 60W to 200W and the optimum power required for the growth of each film was estimated. The details about the effect of sputter power variations are discussed in forth coming sections.

4.3.2 Effect of substrates

Different substrates provide films with different orientation and have an influence on the crystalline nature of the films formed. Micro glass slides are

usually used for the deposition of films at low temperatures since they have good transparency in the visible range and also due to their cost effectiveness. Films deposited on quartz substrates are used to investigate the optical properties since they possess high transmission over the range of wavelengths from ultraviolet to infrared. They also have enhanced smoothness and uniformity of thickness, compared to normal glass substrates. Contamination can be avoided up to a certain limit using quartz substrates, since they are available in highly pure form. Their chemical resistance or stability against a wide variety of solvents and heat resistance over a wide temperature range makes them suitable candidates for high temperature deposition [10]. Quartz substrates were used in this work to obtain conducting films. Kapton tapes were used to mask the films during deposition of *p-n* hetero junctions. The substrates were subjected to a thorough cleaning process prior to deposition. They were washed in distilled water and extran solution twice and dried. Then the substrates were ultrasonically cleaned in acetone and dried and used for deposition.

4.3.3 Effect of nature of target

The technique of magnetron sputtering was developed initially to coat films of metals or alloys having high electrical conductivity; for eg: aluminium, gold, silver, copper etc. The target material had to be essentially electrically conductive to achieve acceptable rates of deposition. Ceramic targets were later used for TCO applications by sintering powders into desired target dimensions by hot or cold pressing. RF magnetron sputtering allows the coating of materials with poor electrical conductivity or insulating materials into thin films.

Oxides, sulphides, selenides, and tellurides are brittle and poorly conducting, and usually, these materials are crushed to fine powders and sintered into high-density targets to avoid cracks and voids and to achieve consistent sputtering [11]. Commercially available metallic targets are typically made from cast metal ingots by melting and solidification to ensure full density with minimum voids, in vacuum or inert atmosphere and hence purity levels of 99.95% - 99.999% can be achieved

[12]. Metallic targets can be shaped into suitable dimensions through thermo-mechanical processes such as forging, rolling and heat treatment.

In this work, we have used high purity tin (IV) oxide powder obtained from Sigma Aldrich (99.99% pure) as the target material for the deposition of *n*-type SnO_2 thin films. The powders were pressed into 2 inch diameter aluminium discs and cold pressed at 1200 kg/cm^2 to achieve high density targets. Care was taken to eliminate voids and cracks in the target to avoid cracking during sputtering. The surface of the target was made smooth and pre-sputtering was done to ensure purity of thin films obtained. For the deposition of indium tin oxide, metallic target purchased from ITASCO, Japan was used with composition-10% by weight tin oxide and 90% by weight indium oxide with purity 99.999%.

4.3.4 Effect of substrate to target distance

The ultrafine structures obtained for coatings by RF magnetron sputtering exhibit enhanced properties compared to traditional materials, thereby ensuring their direct application in modern optoelectronic devices. The substrate - target distance or working distance is vital in determining the characteristics of deposited films in atomic and molecular scale, since the energy of the depositing particles are expected to affect the nucleation and hence the structural formation of the films [4]. At very close working distances, the deposited atom distribution follows the cathode erosion profile. As we increase the working distance to about 100–150 mm, a uniform distribution of the depositing atoms may develop but the kinetic energy of particles will be lower as they approach the substrate, due to larger travel distance. This leads to increase in collision and scattering of sputtered atoms. Working distance has a significant role in enhancing the deposition rate, microstructure and hardness of coatings [13]. At very large working distances, the energy of atoms/molecules are reduced, thereby reducing the nucleation leading to the formation of a coarse grain structure.

Although a strict formula has not been proposed for grain size control and uniform film density distribution at a particular working distance, in our work, the working distance was varied from 60 mm to 200 mm and after several trials, a

particular distance was selected for each target, appropriate for getting good quality films. We have optimised the distance between substrate and target for each type of film for the effective control of thin film properties.

4.3.5 Effect of substrate temperature during sputtering

Substrate heating has profound influence on the adhesive properties and deposition rate of films [14-16]. The effect of substrate temperature on the rate of deposition at low pressure conditions is entirely different from that at high pressure conditions, which may be attributed to variation in gas density. The pressure dependence of deposition rate at different substrate temperatures is a result of variations in gas density with temperature [17]. These variations take place according to the equation,

$$P = NkT \qquad (4.1)$$

where P is the pressure of gas, N is the gas density, k is the Boltzmann's constant and T is the temperature of the gas. An increase in temperature at constant pressure is correspondent to a decrease of pressure at constant temperature to obtain decrease of gas density N, and vice versa. We have investigated the effect of substrate temperature on the surface morphological and physical properties of thin films from room temperature to 200^0 C.

4.4 Tin (IV) oxide

Tin (IV) oxide (SnO_2) is one of the simplest semiconductor material used as TCO. Earlier it was widely used for anti-static coatings, transparent electrodes in display panels and transparent heater films in aircraft windshields. Its low cost, non - toxic nature and ease in handling renders it largely in use in laboratories as well as industries [18]. Almost all *n*-type TCOs are characterised by a conduction band similar to highly dispersed lone free electrons. Degenerate doping enhances the charge carrier mobility due to small effective mass thereby leading to Burstein-Moss shift, as discussed previously. This enables broadening of optical transparency range and maintains the valence band optical transitions out of the visible range [19]. This is vital for oxides which are not transparent throughout the visible

spectrum. Achieving the most favourable performance in a TCO is demanding because of the compound relationship between its electronic and optical properties [20]. Our main aim was the detailed investigation of the transparent and conducting behaviour of tin oxide thin films deposited by radio frequency magnetron sputtering.

4.4.1 Electronic structure and transparent conducting properties

Tin belongs to group IV B metals and its oxide has a rutile structure. It possesses smaller ions and is primarily ionic bonded. Each tin atom is bounded by six oxygen atoms in an octahedral array, and each oxygen atom is surrounded by three tin atoms in a planar array. The crystal structure of SnO_2 is given in figure 4.1. It has a direct band gap of 3.6 eV and electron effective mass is low, 0.23-0.3 m_e. Interaction between the 2*p* orbitals of oxygen and *ns* metal orbitals gives rise to electronic band structures in metal oxides in the TCO phase space. The bonding and non-bonding 2*p* oxygen states form the valence band while the anti-bonding *s* orbitals of metals and *p* orbitals of oxygen gives rise to the conduction band.

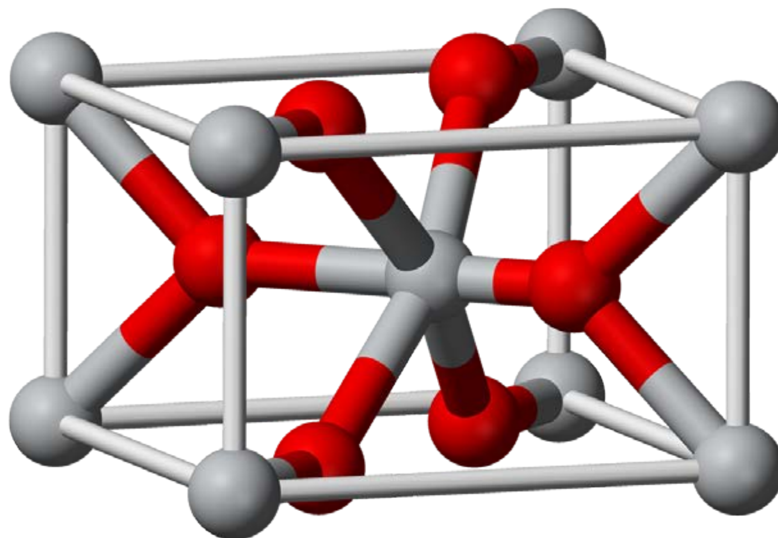

Figure 4.1 Crystal structure of SnO_2

Theoretical band structure calculations reveal the equivalent contributions of oxygen 2*p* and metal *ns* states to the conduction band [21]. Once the charge carriers

fill the conduction band, a metal *s* and oxygen *p* orbital network is formed for effective charge transport, which results the formation of a gap between valence and conduction bands. These band gaps play a key role in the photon induced conduction in TCOs. Electronic band structure calculations within screened-exchange local density approximation (sX-LDA) gives highly accurate values for energy bands and are in good agreement with the experimental values (3.6–4.0 eV for SnO_2) [22].

Due to the spherical symmetry of *s* orbitals, coordination of cations by oxygen atoms does not influence the *s-p* overlap of metal and oxygen atoms. The largest overlap is attained when cations surround the oxygen atoms in an octahedral pattern, i.e., each p_x, p_y and p_z oxygen orbitals are connected to two *s* orbitals.

4.5 Results and Discussion

The sputtering process for the deposition of tin oxide thin films were performed as two separate experiments - one by varying the sputter power and second by varying the substrate temperatures. The rate of deposition of SnO_2 thin films have been studied for a wide range of sputter powers and optimised. When the sputtering was performed below 60 W, the rate of deposition was found to be very less and in order to get a uniform crystalline film, sputtering had to be done for a long interval of time. Also, when the sputter power exceeded 200 W, the films formed were too thick and opaque, which cannot be used as practical TCOs. Hence we had chosen the films sputtered at powers ranging from 60 W to 200 W. Figure 4.2 shows the variations in yield of radio frequency magnetron sputtering equipment at various ion energies. The substrate temperatures were also selected so as to obtain good quality films with good adherence to the substrates. Detailed structural, morphological, optical and electrical characterisations were performed and the results are discussed in the subsequent sections. The optimum experimental parameters followed during deposition in our work are given in table 4.1.

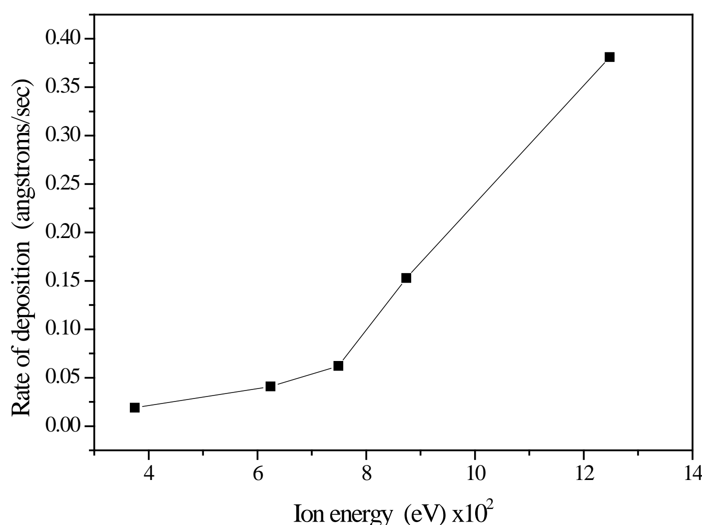

Figure 4.2 Yield of sputtering of SnO_2 thin films

Table 4.1 Experimental parameters of sputtering process

Target	Ceramic SnO_2 target
Substrate	Quartz
Target–substrate distance	120mm
Deposition (Ar) pressure	$4x10^{-2}$ mbar
Base pressure	$1x10^{-6}$ mbar
Deposition time	30 minutes
RF power	60-200W
Substrate temperature	Room Temperature (25^0C) - 200^0C

4.5.1 X- ray Diffraction

XRD analysis was carried out using Integrated Powder X-ray Diffraction software (PDXL) complemented by the database, International Centre for Diffraction Data (ICDD-2012). Figure 4.3 exhibits the room temperature X-ray diffraction pattern of SnO_2 thin films sputtered at a substrate temperature of 150^0 C for 30 minutes at sputter powers ranging from 60-200W. The resulting plots are stacked by *y* offset intensities in the order of increasing sputter power and the detected peaks confirm the polycrystalline nature of thin films.

The films sputtered at 60W showed less intense peaks, but as the sputtering power was increased to 200W, diffraction patterns of (110), (101) and (200) planes appeared corresponding to 2θ values of 21.91, 29.33 and 30.77 respectively. The reflection of each plane is indexed in the plot and identified as the reflections of orthorhombic crystal structure of SnO_2 (ICDD: 00-029-1484) with space group, $P2_12_12_1$. Lattice parameters are a = 4.7140 A^0, b = 5.7270 A^0, c = 5.2140 A^0 and $\alpha = \beta = \gamma = 90^0$. All samples showed the same reflecting planes, but there is considerable increase in the intensity of peaks with increase in the sputter power. This is due to the enhancement in crystallinity, since at higher sputtering power, the inert argon gas acquires adequate energy to provide higher translational kinetic energy to the ad-atoms, causing surface diffusion and thereby leading to the nucleation and growth of the films [23].

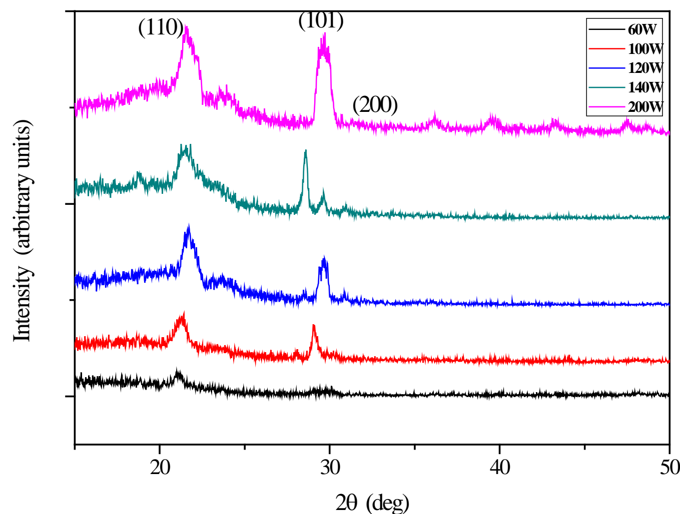

Figure 4.3 XRD pattern of SnO_2 films sputtered at substrate temperature of 150^0C

From figure 4.3, the peaks are observed to be shifted to a higher 2θ values with increase in sputter power, which can be attributed to the apparent stress induced in the thin films during sputtering at higher powers. The peak shifts occurring at different powers are tabulated in table 4.2. Stresses induced in thin films may be of two kinds – intrinsic and extrinsic. Intrinsic stresses are caused mainly due to distortions in lattice structure, impurities and defects in the crystals. Extrinsic stresses are caused due to lattice mismatch between the coated films and substrates or due to large disparity in their thermal expansion coefficients [24-25]. The effect due to the latter is insignificant for thickness of films greater than 100 nm.

In our study, since all films have thickness above 100 nm, stress induced in films may be purely of intrinsic nature. The effect of such stresses increases with sputter power, since, during the process of sputtering, the higher energy of bombarding species induce defects and distortions in the lattice structure, which can be observed in the physical property variations of the films, such as electrical conductivity [26].

Table 4.2 Peak shifts of XRD pattern

Sputter power	Shift in (110) plane from 21.83^0	Shift in (101) plane from 29.25^0
100W	0.18	0.02
120W	0.36	0.34
140W	0.02	0.02
200W	0.08	0.08

Figure 4.4 gives the XRD plots of the samples sputtered at various substrate temperatures at a sputter power of 120W for 30 minutes. From the plots, it can be observed that the respective locations of all reflections are same for all samples but peak intensities are slightly enhanced with increasing substrate temperature. No peak shifting is observed with variations in substrate temperature and hence it can be assumed that lattice strains induced in all films are the same.

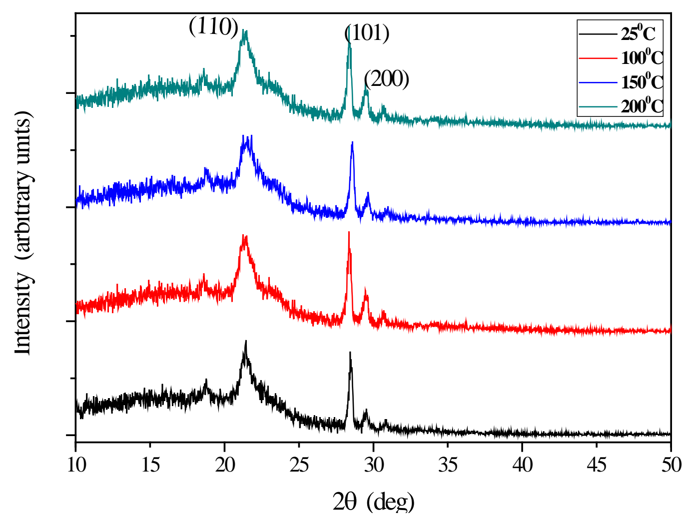

Figure 4.4 XRD pattern of SnO_2 films sputtered at 120W

The crystallite size of the film sputtered at 60W could not be calculated as it showed less intense peaks. The variations in crystallite sizes are consistent with previous literatures [7].

Table 4.3 Crystallite size variations of SnO_2 films with sputter power

Sputter power (Watts)	Crystallite size (nm)
100	178.1
120	232.3
140	287.4
200	317.6

The crystallite size, *d* was evaluated using Scherrer's relation from the full width at half maximum. The narrower the diffraction peak, the larger is the crystallite size, due to periodicity of the individual crystallite domains which are in phase. Generally, thin films have certain preferred orientation, such as (101) for SnO_2, which has the greatest degree of orientation. Therefore, the measured crystallite size of the diffraction peak at (101) represents the crystallite size in a vertical direction, normal to the surface of substrate [7]. The crystallite sizes of all samples, calculated by Scherer's formula are given in table 4.3 and 4.4, which are in agreement with the crystallite sizes observed from Scanning Electron Micrographs, as discussed in the next section. Figure 4.5 illustrates the variations in crystallite sizes.

Table 4.4 Crystallite size variations of SnO_2 thin films with substrate temperature

Substrate temperature	Crystallite size (nm)
25^0C	108.6
100^0C	112.1
150^0C	232.3
200^0C	262.0

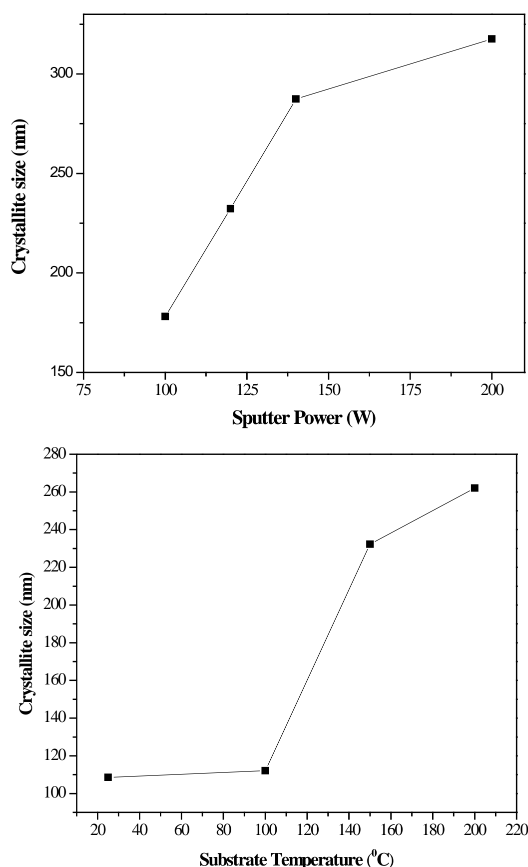

Figure 4.5 Crystallite size variations with sputter power and substrate temperature of SnO_2 thin films

From figure 4.5, it can be observed that the crystal size increases almost linearly with sputter power. This is due to the increased kinetic energy of particles striking the substrate per unit time.

4.5.2 Scanning Electron Microscopy

SEM images of the samples sputtered at different RF powers are shown in figure 4.6, under same magnification. From these images, it can be inferred that as the sputter power is increased, there is slight increase in the crystallite size, similar to that calculated from the diffraction pattern of the corresponding samples. This can be attributed to the increased surface diffusion of ad-atoms due to larger mobility acquired from the generated plasma.

The films sputtered at 120W and below showed definite crystallites uniformly distributed on the substrates, whereas above this value, the film surface

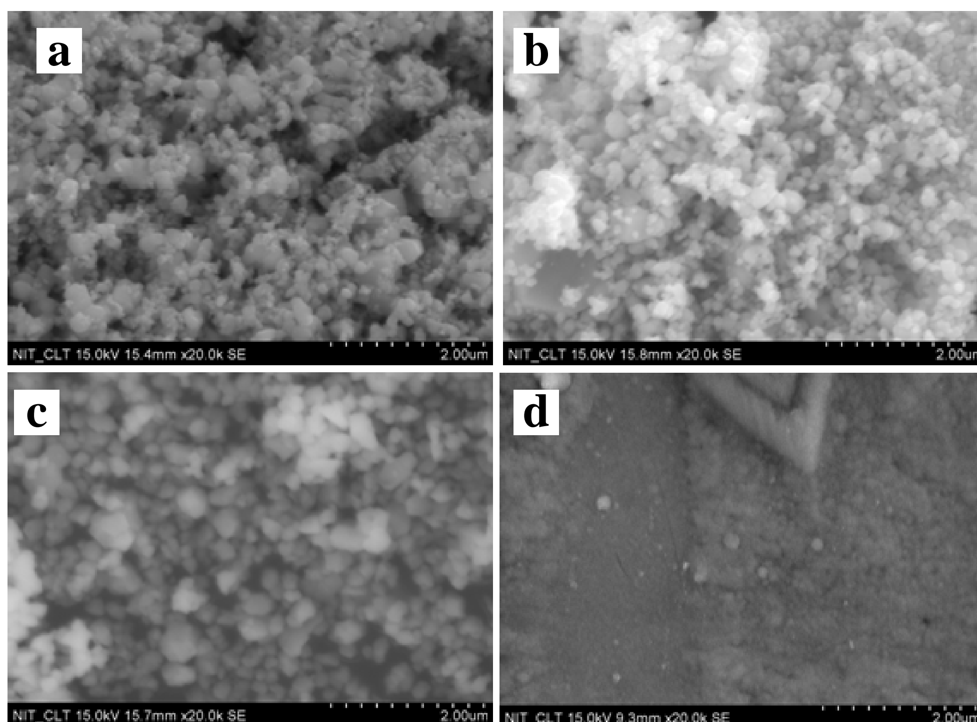

Figure 4.6 SEM images of SnO_2 films sputtered at substrate temperature of 150^0C and sputter power (a) 60W, (b) 100W, (c) 120W and (d) 200W

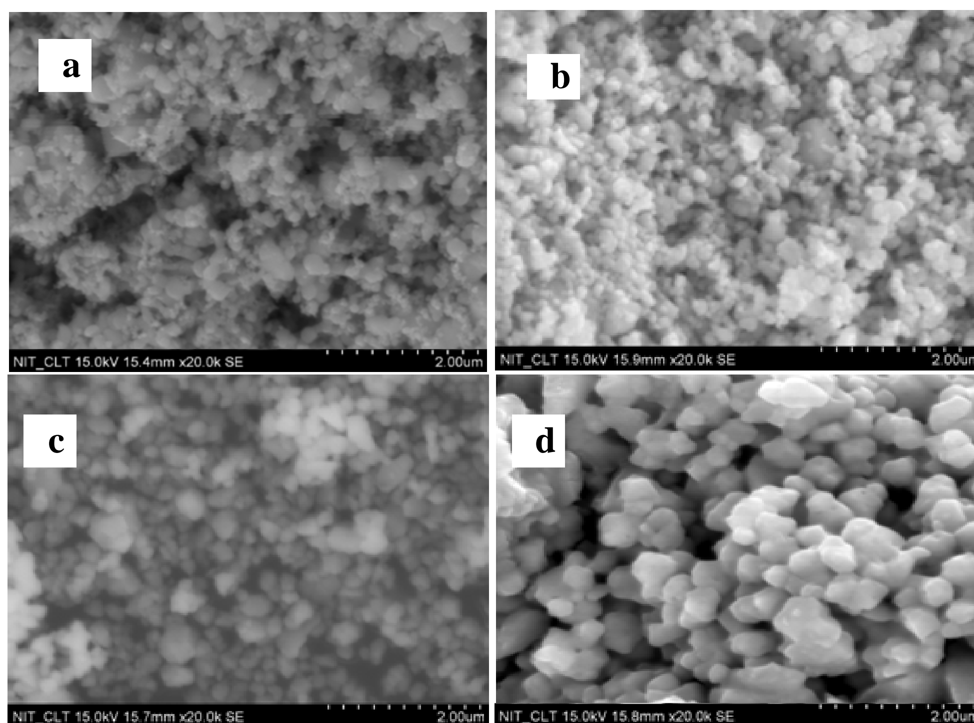

Figure 4.7 SEM images of SnO_2 films sputtered at sputter power of 120 W and substrate temperatures of (a) 25^0C, (b) 100^0C, (c) 150^0C and (d) 200^0C

showed the formation of large crystallites. This may be due to the non uniform scattering taking place at higher power, due to the very high energy of ionised plasma. For the film sputtered at 200 W, no definite particles were observable. These may be conglomerates of many smaller sized grains in the samples that may be formed due to the greater energy imparted to the ions [21].

SEM micrographs of the samples at different substrate temperatures also exhibit enhancement in crystallinity as can be seen from figure 4.7. These show heterogeneous grain distribution with increased substrate temperature that may be due to larger rate of deposition, resulting in faster grain growth. These results establish the fact that energy of ions during sputtering process plays a key role on the surface morphologies of the resultant films [6].

4.5.3 Energy Dispersive Spectra

In the scanning electron microscope, the backscattered electron images represent the compositional arrangement of different elements and the identification of these elements can be performed using Energy Dispersive Spectroscopy (EDS). This involves generation of X-ray spectra from the entire scan area of SEM.

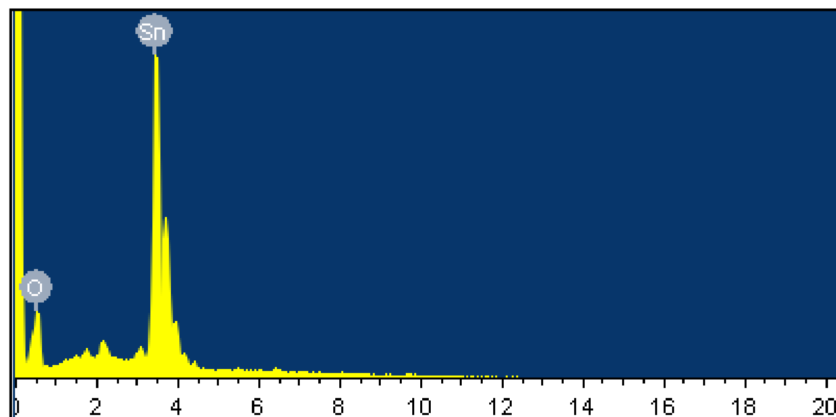

Figure 4.8 EDS spectra of the samples

In an EDS spectrum, the *Y* axis represents the X-ray counts and *X* axis represents the energy level of those counts. EDS interpretation is done by associating energy level of generated X-rays with elements and shell levels from

which they are generated. The compositional analysis of the samples was performed using energy dispersive spectroscopy (EDS) for the films grown at 150^0C and 120W and is shown in figure 4.8. Similar pattern was obtained for all other films. It confirms the presence of the desired constituents, tin and oxygen and the absence of other impurities in the sample.

4.5.4 Atomic Force Microscopy

The surface morphology of the samples deposited at various sputter powers and substrate temperatures were examined by Atomic Force Microscopy (AFM). The 2D and 3D surface topographies of the thin films deposited at various sputter powers at constant substrate temperature of 150^0C are shown in figure 4.9 and those sputtered at 120W at different substrate temperatures are shown in figure 4.10.

The images were obtained in a 5x5 µm area under non-contact mode at room temperature and ambient pressure conditions for the films deposited on quartz substrates. The tip of the atomic probe is attached to a cantilever, which scans the surface in a raster pattern, laterally on the surface. Whenever the cantilever detects an obstacle, a laser beam attached to it deflects, which is used for the estimation of interaction force between the scanned surface and the probe tip, and thereby to calculate the surface features and to obtain the surface topographical image.

The surface morphology images confirm the dense growth of crystallites and homogenous distribution of grains with increase in sputter power and substrate temperature. The films deposited at high sputtering powers exhibit large cluster formations with non uniform orientations as in figure 4.9 (d) and (e). This phenomenon can be observed clearly in SEM images also (Page no. 77). These structural formations are due to the boost in surface mobility of ad-atoms with sputter power, which results in the formation of continuous films. Transfer of momentum takes place onto the growth surface by the surface diffusion of these ad-atoms, which is enhanced by higher sputtering powers [6].

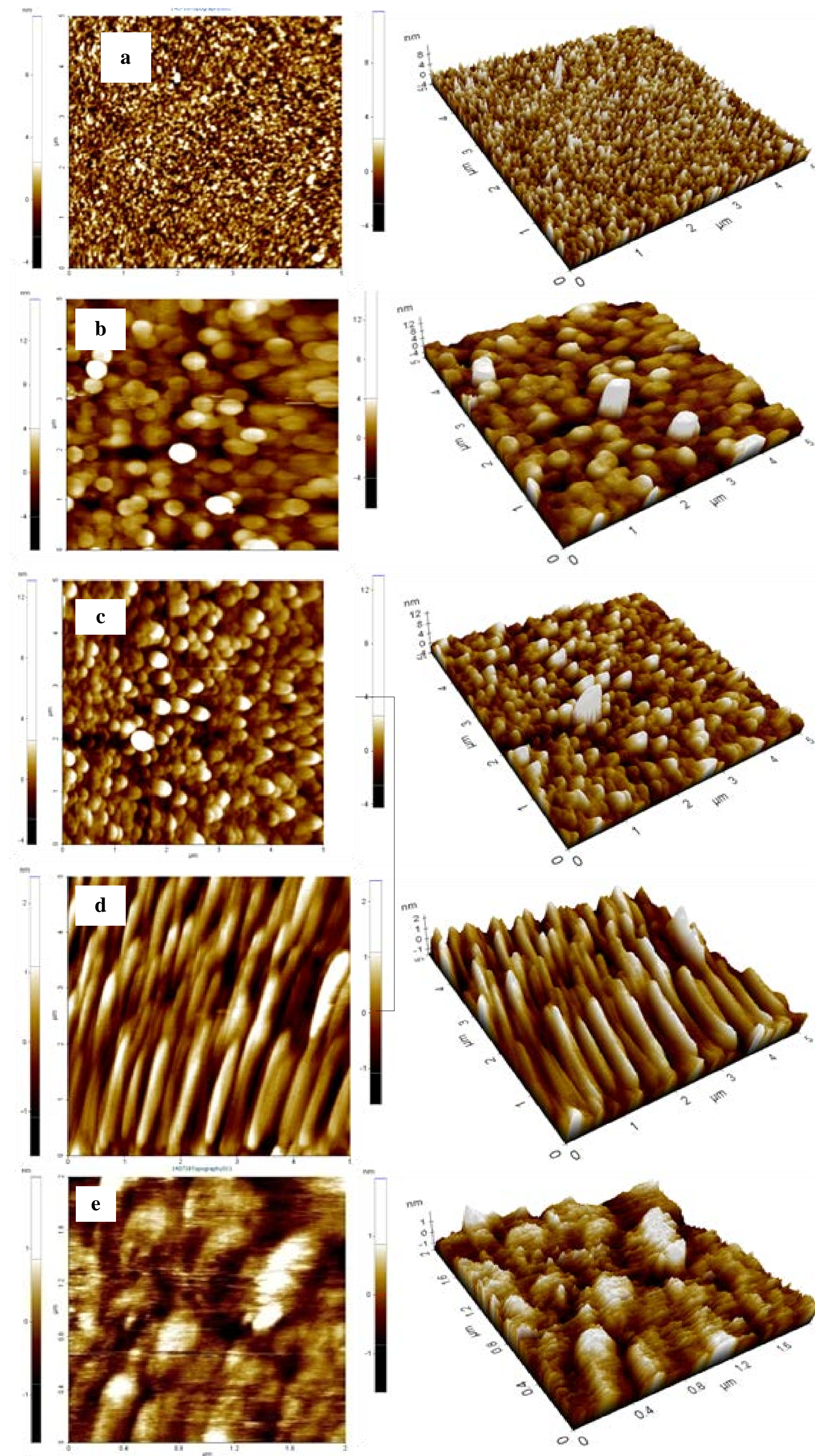

Figure 4.9 2D and 3D AFM images of SnO_2 thin films sputtered at power (a) 60W (b) 100W (c)120W (d) 140W and (e) 200W

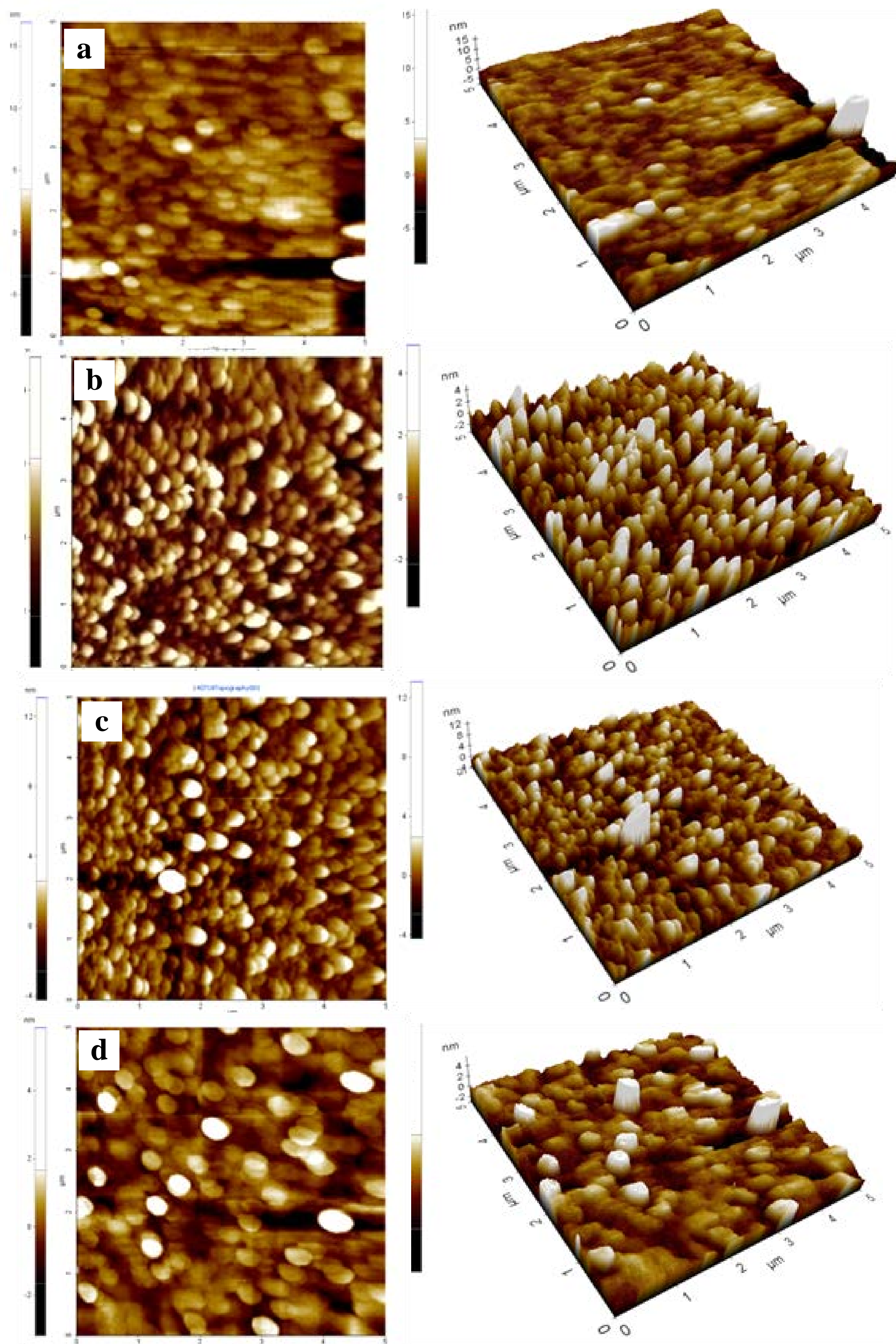

Figure 4.10 2D and 3D AFM images of SnO_2 thin films grown at substrate temperature of (a) 25^0C (b)100^0C (c)150^0C and (d) 200^0C

Table 4.5 Variation of RMS roughness with sputter power

Sputter power (W)	RMS surface roughness (nm)
60	0.436
100	0.553
120	1.023
140	1.216
200	2.118

Surface roughness of a TCO film has significant role in its application in optoelectronic devices, since the carrier mobility and surface light scattering depends on the smoothness of that particular coating. A smooth surface morphology provides less scattering of incident light, which leads to increase in film transmittance [6]. To analyse the surface roughness of the sputtered thin films, four random areas over the surface was chosen and the root mean square (RMS) measurements were recorded. These values as a function of sputtering power and substrate temperature are given in table 4.5 and 4.6.

Table 4.6 *Variation of RMS roughness with substrate temperature*

Substrate temperature	RMS surface roughness (nm)
25^0C	0.853
100^0C	0.974
150^0C	1.023
200^0C	1.666

It was observed that the RMS roughness increased with sputtering power. For films deposited at a substrate temperature of 150^0C and 60 W, the lowest RMS value of surface roughness of 0.436 nm was observed and as the sputter power was increased to 200 W, the RMS value was 2.118 nm. This trend of RMS roughness is related to crystallite size and it is likely that low sputtering power exhibits low deposition rate which is due to less energetic argon ion over the target species, resulting in slow nucleation and growth onto the substrate surface.

The root mean square roughness of the films varied linearly with substrate temperature. The two dimensional and three dimensional surface topographies of the samples confirm that grain distribution on substrate surfaces are more heterogeneous with increasing substrate temperature. AFM images showed that by increasing substrate temperature the size of grains/clusters on the surface of thin films increases. The value was found to vary from 0.853 nm to 1.666 nm for films with variation in substrate temperature from room temperature (~25^0C) to 200^0C during sputtering. Significant variations were observed in the morphology of these films with deposition conditions. This result is consistent with previous conclusion that the crystalline growth increases by increasing the substrate temperature, which was observed in SEM images also.

4.5.5 Transmission Electron microscopy

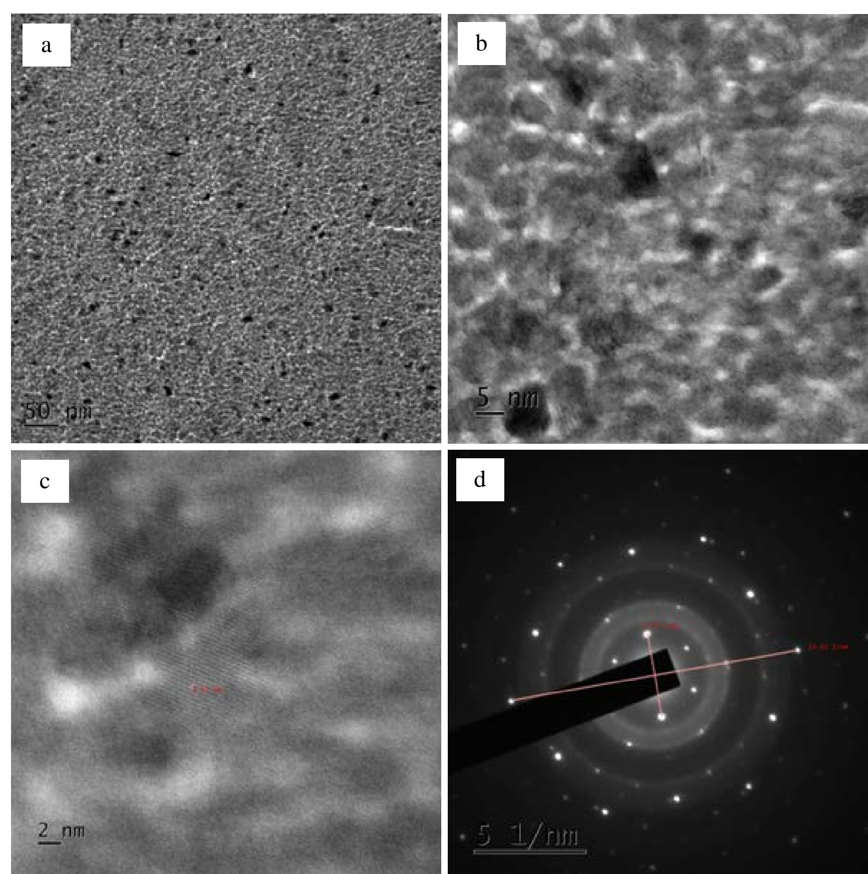

Figure 4.11 TEM images at (a) Low resolution (b) Low resolution (c) High resolution and (d) SAED pattern of SnO_2 films sputtered at 150^0C and 120W

Figure 4.11 shows the TEM images and corresponding SAED pattern of SnO_2 films sputtered at 120 W and 150^0C for 30 minutes. It shows highly crystalline nature of the films. From the diffraction rings in SAED pattern the predominant (110) and (101) planes of orthorhombic SnO_2 were identified. The d-spacing of the lattice was also determined and compared with that obtained from XRD. The values are tabulated in table 4.7.

Table 4.7 *Comparison of d- spacing from TEM and XRD*

Parameter	SAED	XRD
d spacing (110)	0.533nm	0.408nm

4.5.6 Optical profilometry

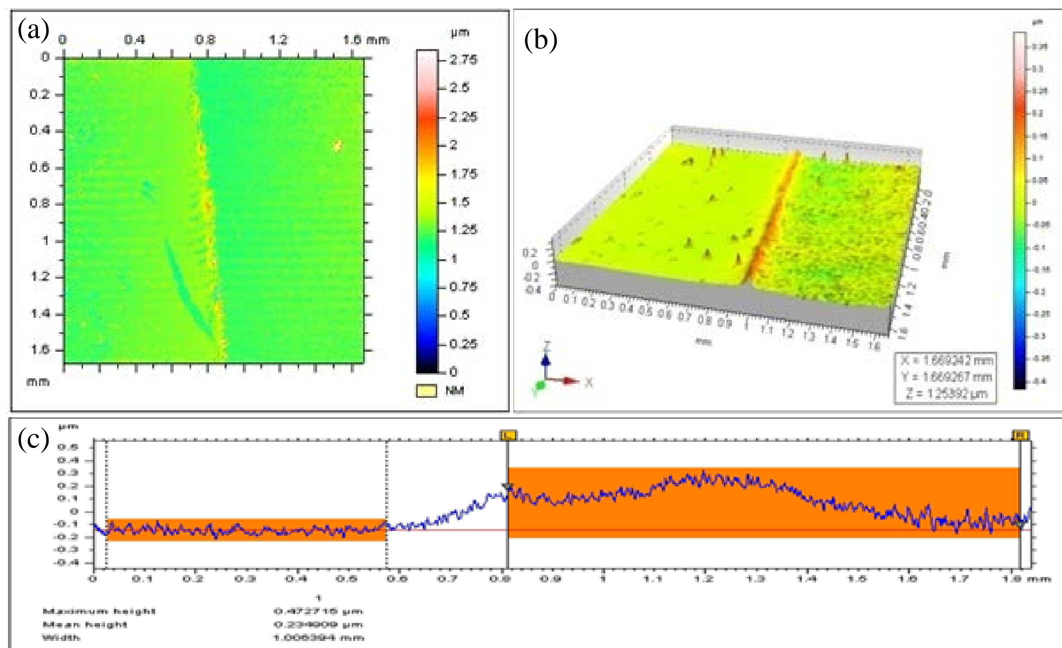

Figure 4.12 (a) 2D Optical profile, (b) 3D Optical profile and (c) line profile of SnO_2 films sputtered at 150^0C and 120W

Figure 4.12 (a) and (b) shows 2D and 3D optical profile of the SnO_2 film sputtered at 120W and 150^0C for 30 minutes. The profile was made on the surface by masking it using Kapton tapes during coating. Figure 4.12 (c) shows the line profile of the film and thickness estimated as the mean height is 234.91 nm. The

films exhibit a smooth surface, comparable to the surface roughness value obtained from AFM (1.023 nm).

4.5.7 Hall measurements

The conductivity of the sputtered thin films was analysed by Hall measurements. It is observed that the sputter power and substrate temperature during sputtering has a significant influence on the electrical properties. Tables 4.8 and 4.9 demonstrate the variations of charge carrier concentration, mobility of charge carriers and the resistivity of thin films with sputter power and substrate temperature respectively.

Table 4.8 Variation of electrical characteristics of SnO_2 films with sputter power

Sputter power (W)	Charge carrier concentration (electrons) (/cm^3)	Mobility (cm^2/Vs)	Resistivity (Ω cm)
60	1.333×10^{15}	80.52	58.14
100	7.092×10^{15}	42.51	0.207
120	2.522×10^{16}	27.79	0.08902
140	2.820×10^{16}	8.643	0.02561
200	3.113×10^{16}	7.923	0.02531

Table 4.9 Variation of electrical characteristics of SnO_2 films with substrate temperature

Substrate temperature	Charge carrier concentration (electrons) (/cm^3)	Mobility (cm^2/Vs)	Resistivity (Ω cm)
25^0C	2.823×10^{15}	66.40	0.333
100^0C	4.313×10^{15}	45.7	0.09217
150^0C	2.522×10^{16}	27.79	0.08902
200^0C	7.87×10^{16}	17.55	0.0452

It is observed that the carrier concentration increases almost linearly with the sputter power. At highest power of 200 W, the charge concentration reaches

3.113x10^{16}/cm^3 while at 60W, it is only 1.333x10^{15}/cm^3, which can be seen in figure 4.13 (a). Carrier concentration follows a linear relation with substrate temperature also, as can be observed in figure 4.13 (b).

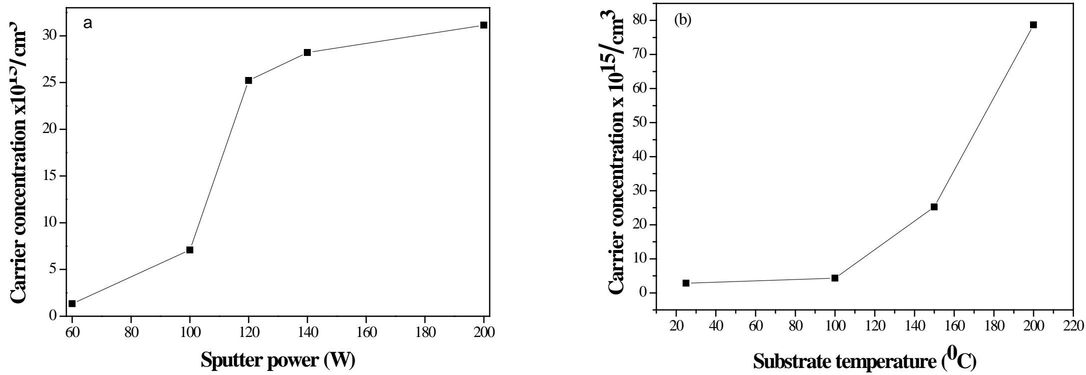

Figure 4.13 Variation of carrier concentration with (a) sputter power and (b) substrate temperature

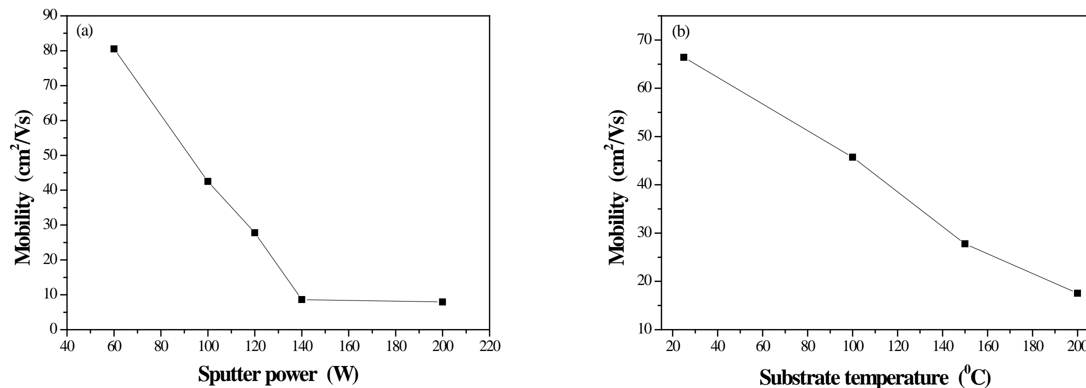

Figure 4.14 Variation of charge carrier mobility with (a) sputter power and (b) substrate temperature

As the concentration of charge carriers increase, there is a decrease in their mobility. Hence the mobility of charge carriers follows an inverse relation with sputter power as well as substrate temperature, as observed in figure 4.14 (a) and (b). The most important electrical property- the resistivity of thin films was also found to have an inverse relation with sputter power. The films sputtered at 60W were found to have a higher resistivity of 58.14 Ωcm, and when the sputter power was increased to 200W, it decreased drastically to 2.531x10^{-2} Ωcm. There had been a decrease in resistivity of the order of 3. The possible factors that contribute to

higher resistivity of films sputtered at lower powers are size effects and reduced diffusion due to lesser surface mobility, as a result of lower energy of ad-atoms during fabrication [8,23].

Lesser surface diffusions of ad-atoms at low sputter powers results in films with lesser crystallinity, as observed from XRD and this contributes to the increased film resistivity. Figures 4.15 (a) and (b) show the resistivity variations with sputter power and substrate temperature respectively. The decrease in resistivity with RF power largely results from the increase in carrier concentration. With higher RF power, sputtered target atoms with higher kinetic energy arrive at the substrate, leading to increased local bonding and consequently, it could be concluded that films sputtered at higher RF power possess a more ordered microstructure with less defects, resulting in enhanced carrier concentration and lower resistivity.

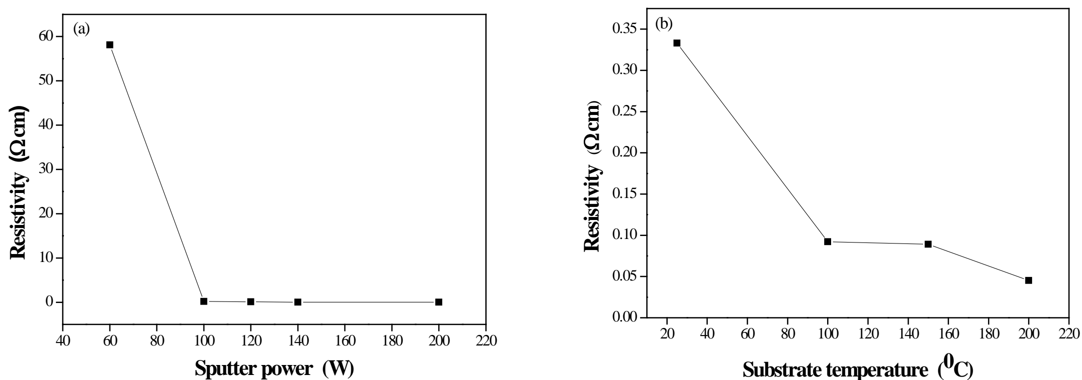

Figure 4.15 Variation of thin film resistivity with (a) sputter power and (b) substrate temperature

4.5.8 UV-Visible spectroscopy

All sputtered films exhibit an average transmittance over 75% in the visible region and a strong absorption in the UV region. The interference fringes in the transmission spectra are indications of the uniform and homogeneous nature of film surface [24]. The maximum average transmittance is observed for the films deposited at 60W with transmittance above 80% and the film with maximum thickness, sputtered at 200W exhibited lower transparency of ~65%. The absorption edge of thin films corresponds to electron transitions from valance band to conduction band

and the band gap energies can be determined using Tauc plot, as described in Chapter 3. The variations in transmission of the films with sputter power are shown in figure 4.16 and it exhibits an overall decrease in transmittance with sputter power. The reduction in transmittance may be caused by the increase in light scattering as the grain size increased and increase in thickness of films with sputter power. Figure 4.17 shows the transmittance variation with increase in substrate temperature during deposition. The films deposited at room temperature showed the least transmittance and films at 100^0C showed the maximum transparency.

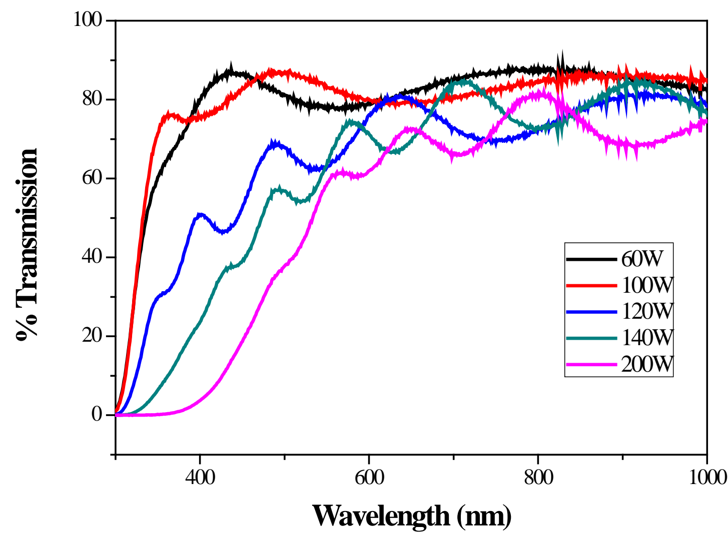

Figure 4.16 Optical transmission spectra of SnO_2 thin films at different sputter powers

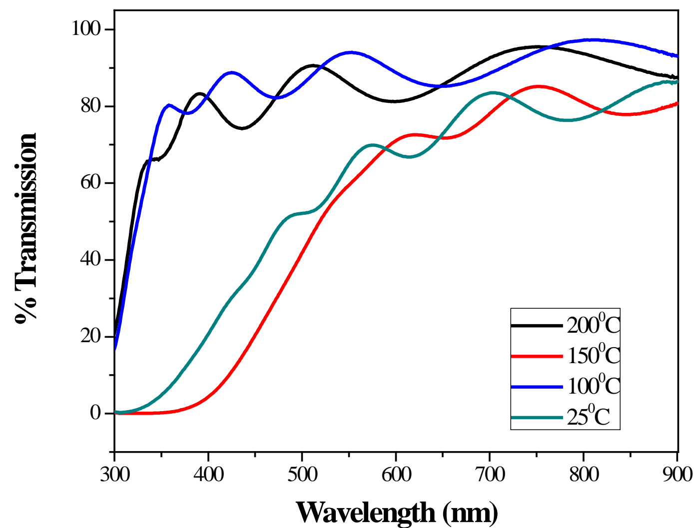

Figure 4.17 Optical transmission spectra of SnO_2 films at different substrate temperatures

As described in Chapter 3, the band gaps were calculated from the optical transmission spectra by plotting $(\alpha h\nu)^2$ versus $h\nu$ and extrapolating the linear portion of the curve to the X axis as given in figure 4.18 (a) and (b). From these plots, it is observed that the band gap increases with RF power and substrate temperature. It can be seen from the Hall measurements that the carrier concentration increases correspondingly with power and temperature of substrate during deposition. The enhancement in band gap is due to the Burstein-Moss effect at high carrier concentrations. The correlation of carrier density and optical band gap of the films with sputter power is depicted in figure 4.19 (a) and (b).

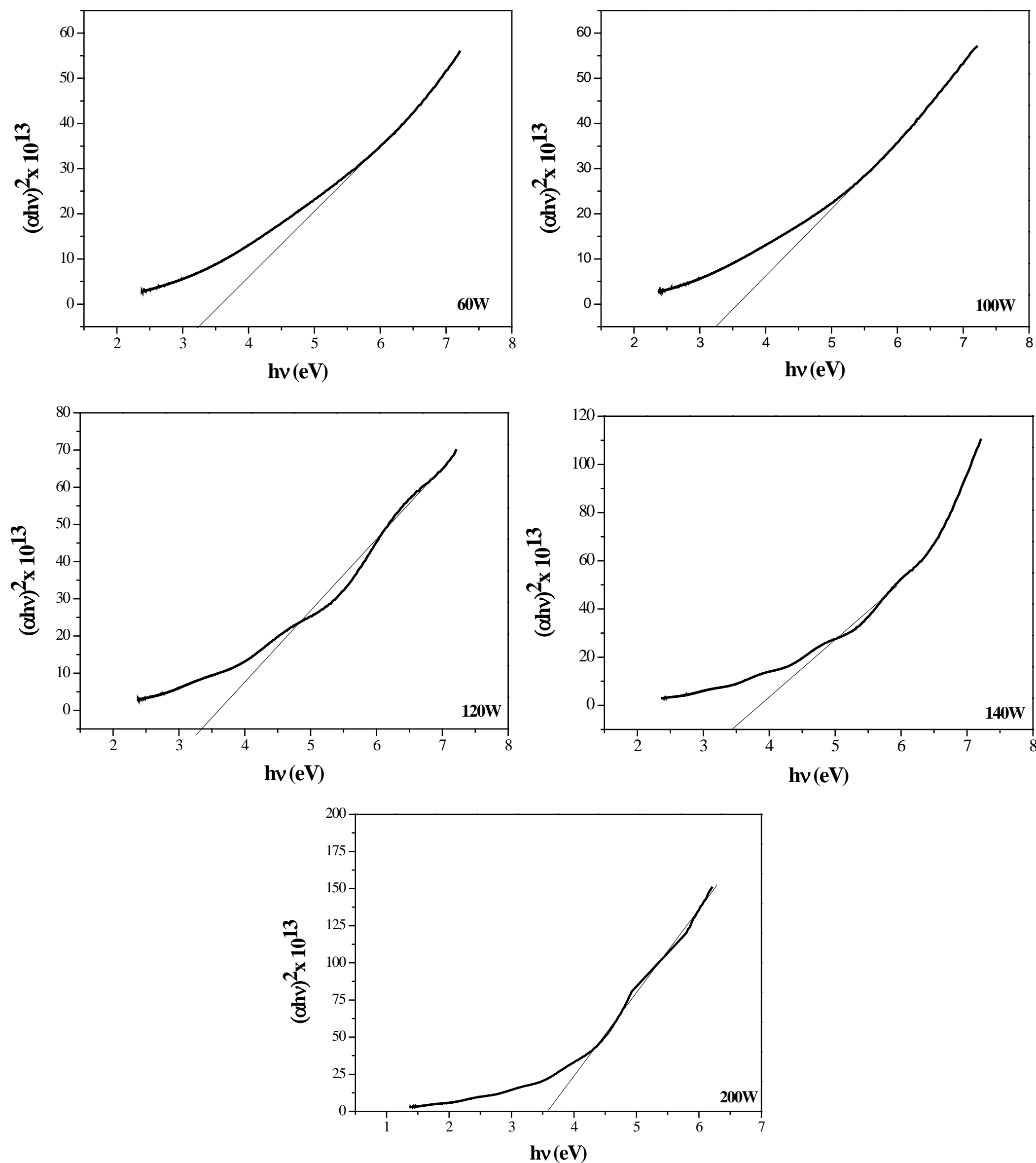

Figure 4.18(a) Tauc plot of SnO_2 films at different sputter powers

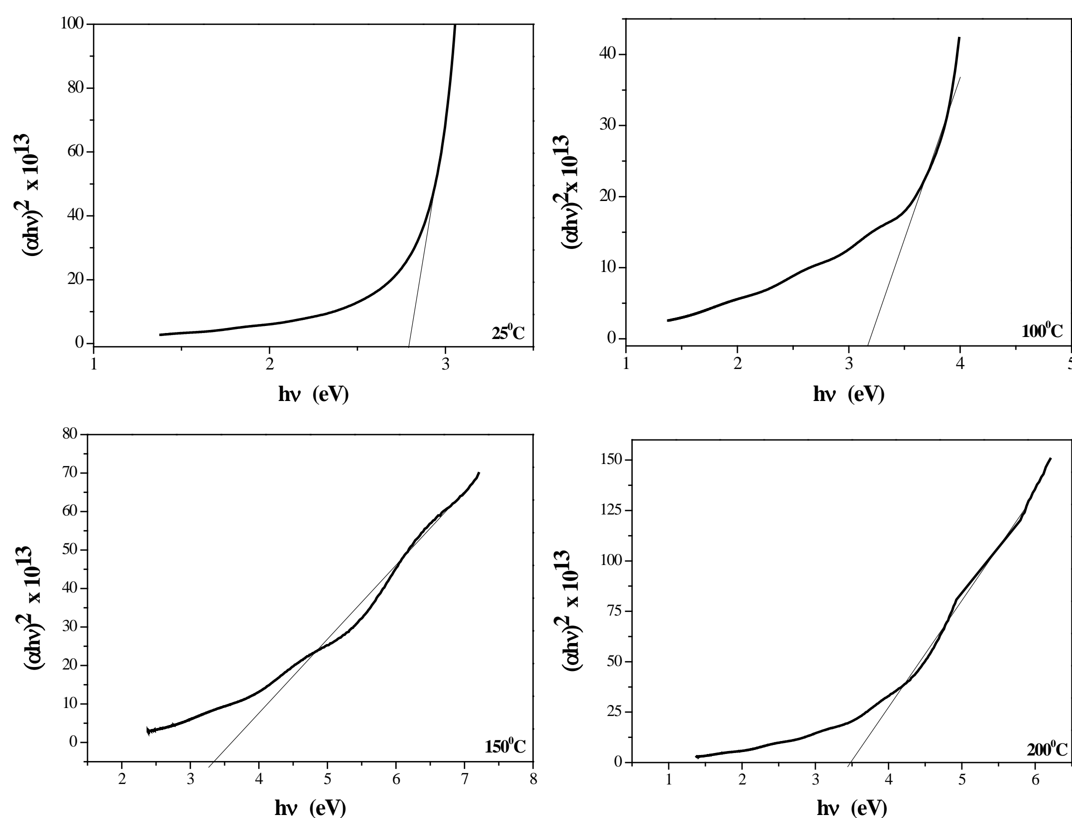

Figure 4.18(b) Tauc plot of SnO_2 films at different substrate temperatures

Table 4.10 Variation of band gap energy with sputter power

Sputter Power (W)	Band gap Energy (eV)
60	3.22
100	3.25
120	3.34
140	3.42
200	3.57

The band gap energies of samples deposited at different sputter powers at 150^0C are tabulated in table 4.10 and that at different substrate temperatures at 120W in table 4.11. It can be observed that the optical band gap energy increases by ~ 11%, from 3.22 to 3.57 eV, when the sputter power was varied from 60W to 200W.

By increasing the temperature of substrate from room temperature to 200^{0}C, the band gap was varied by ~ 21%, from 2.86 to 3.47 eV, which may be due to the increase in thin film thickness [6]. The Burstein-Moss effect can explain the broadening of band gap energy with the increasing carrier concentration [21]. The optical characteristics of sputtered films substantiate typical transparent conducting nature of the films by absorption of photons at effective band gap in the near UV-region.

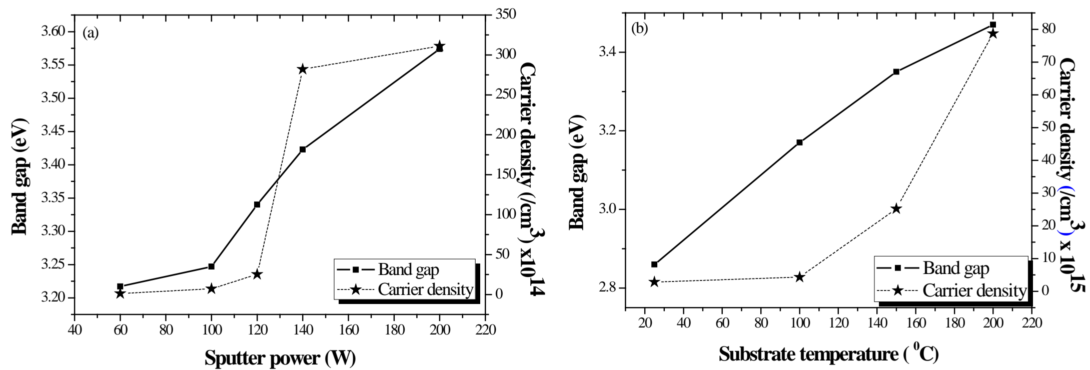

Figure 4.19 Correlation of charge carrier density and optical band gap with (a) sputter power and (b) substrate temperature

Table 4.11 Variation of band gap energy with substrate temperature

Substrate temperature	Band gap Energy (eV)
25^{0}C	2.86
100^{0}C	3.17
150^{0}C	3.34
200^{0}C	3.47

Thicknesses of the films were calculated from the transmittance spectra using the Swanepoel envelope method [25], as discussed in Chapter 3. The envelope curve of T_{max} and T_{min} in the transmission spectra is used to determine thickness of the films. The value obtained for films sputtered at different powers are tabulated in table 4.12.

Table 4.12 Thickness variation with sputter power of SnO_2 films

Sputter power (W)	Thickness of films (nm)
60	-
100	-
120	258.97
140	320.24
200	492.84

The thickness of films at 60W and 100W could not be calculated as the number of fringes does not meet the minimum requirement to calculate using this method. The variation in thickness of films grown at different substrate temperatures are tabulated in table 4.13. The thickness calculated was found to be close to the values obtained using optical profiler.

Table 4.13 Thickness variation with substrate temperature of SnO_2 films

Substrate Temperature	Thickness (nm)
25^0C	172.03
100^0C	202.54
150^0C	258.97
200^0C	311.56

The results of optical investigation of the sputtered tin oxide films are significant since it confirms the phenomena of Burstein-Moss shift in TCOs. This can improve the electrical properties of TCOs such as conductivity and mobility of charge carriers.

4.5.9 X-ray Photoelectron Spectroscopy

The XPS studies were performed using standard Al Kα source for the investigation on element valence state of SnO_2 film sputtered at 150^0C and 120 W. C*1s* core-level spectrum at 284.5 ± 0.1eV as in figure 4.20 was used to standardise the energy glide due to charging effects.

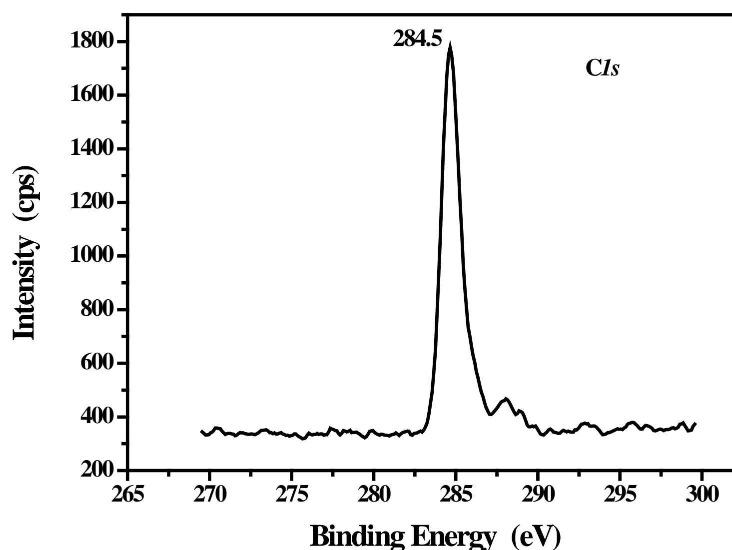

Figure.4.20 Carbon 1s spectra for XPS calibration of SnO_2 spectra

The wide survey scan was used for identifying the elements present in the sample and the spectra were further processed for calculating the percentage of elements present. CASA XPS was used for the data analysis, and detailed surface analysis of the thin film was performed by recording elemental scanning for the constituent elements on sample surface at same experimental conditions. The obtained elemental spectra were processed using PEAKFIT 41 software for extracting additional information. A standard Shirley background was used as baseline for fitting the narrow scan spectra with Standard Gaussian–Lorentzian components at 70% - 30%. The peaks are fitted with the components in a reduced "chi-square" parameter ranging from 0.5 to 1.5, which confirms the goodness of fit in asymmetric peak fitting. NIST database was used to evaluate the binding energy and binding energy shifts.

In the narrow scan spectra, Sn *3d* and O *1s* have been detected. The core level peaks corresponding to Sn *3d* orbital levels give rise to two possible energy states with different energies, due to spin-orbit splitting (*j-j* coupling). Sn *3d* core level spectra typically have two components due to the *j-j* coupling.

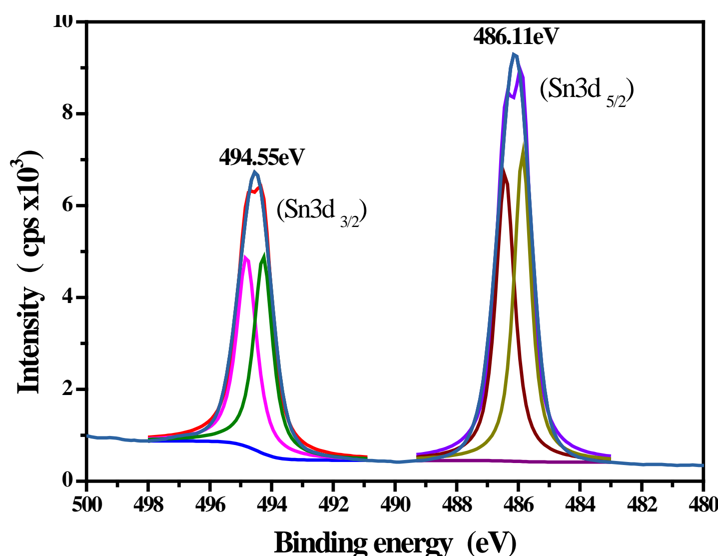

Figure 4.21 Narrow scan analysis of tin in sputtered SnO_2 films

The chemical bonding status between tin and oxygen was investigated with XPS to determine the electrical properties of the tin oxides. Figure 4.21 shows the Sn *3d* XPS spectra of thin films deposited at 120W and figure 4.22, shows the corresponding core level spectra of oxygen. The Sn *3d* is further split into two due to its *j-j* splitting. The spectra were asymmetric with probable electronic instability, and the peaks correspond to Sn $3d_{5/2}$ and Sn $3d_{3/2,}$ centered at 486.11eV and 494.55eV. The peak shape analysis revealed that, the Sn ions in the thin film surface are composed of Sn^{2+} and Sn^{4+} ionic states. The spectrum is fitted with corresponding components, as in figure, with two peaks centered at 485.78 ± 0.10 eV and 486.42 ± 0.10 eV for Sn $3d_{5/2}$ and 494.12 ± 0.10 eV and 494.83± 0.10 eV for Sn $3d_{3/2}$ components. The results suggest that the sputtered films are composed of tin oxides with random distribution of Sn ions and the doublet separation is consistent with literature [27]. Also from the survey scan spectrum in figure 4.23, the ratio of O: Sn peak intensity of binding energy was calculated and found to be 1.077, which suggests oxygen deficiency in crystal structure, which may be the major cause of good conductivity in these films, as confirmed by Hall measurement studies.

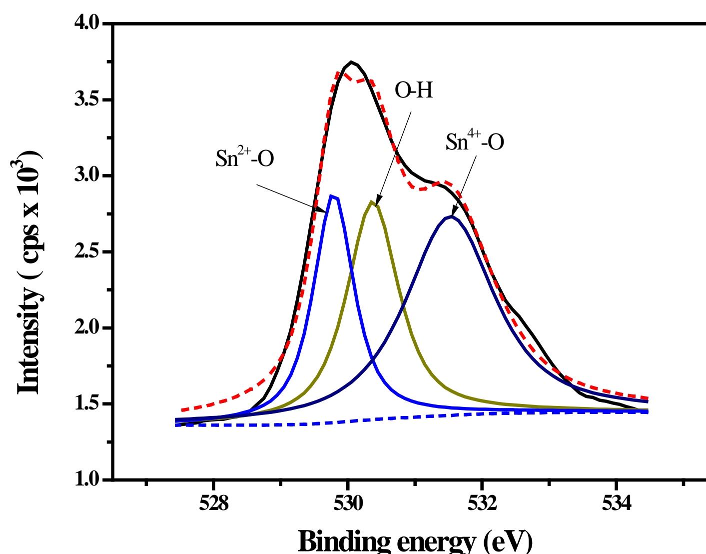

Figure.4.22. Narrow scan analysis of oxygen in sputtered SnO_2 films

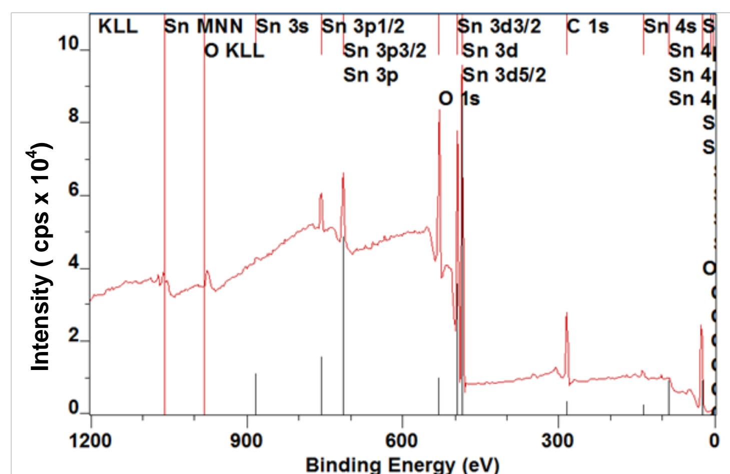

Figure 4.23 Survey scan spectrum of SnO_2 films

Figure 4.23 shows the survey spectrum of the sample, clearly establishing the existence of tin and oxygen in the sample without any impurities. The main peak located at 932.7 eV could be attributed to the Cu $2p_{3/2}$ orbitals. No obvious shake-up satellite peaks on the higher binding energy side could be observed, which confirmed the absence of Cu^{2+} on the sample surface. Figure 4.21 shows high resolution XPS spectrum over Sn $3d_{5/2}$ peak. It could be best fitted by the combination of two peaks centered at 486.5 eV and 485.5 eV, which could be assigned to Sn^{4+} $3d_{5/2}$ peak and Sn^{2+} $3d_{5/2}$ peak, respectively. Thus, a small portion of

Sn^{4+} on the film surface was reduced to Sn^{2+} during the sample synthesis and storage under normal ambient condition. The Sn^{2+} percentage was determined to be ~36%, while no SnO could be distinguished either in TEM or XRD analysis results. As a surface characterization technique, XPS could determine the surface composition within a very shallow depth. Thus, the existence of Sn^{2+} must be only on the surface of SnO_2 thin films, while the dominant Sn species in the sample existed as Sn^{4+}. It had been well reported in literature that Sn^{2+} state could be detected on the surface due to the oxygen deficiency in the top layer of the films.

4.5.10 Optical transparency of the film

The films sputtered at 150^0C and 120W is shown in figure 4.24. The high optical transparency is evident from the photograph and is consistent with the transmittance value (~80%) obtained from UV-Visible spectrum.

Figure 4.24 Actual photograph of SnO_2 film sputtered at 150^0C and 120W

4.6 Indium tin oxide (ITO)

In the earlier sections, we have investigated the characteristics of tin (IV) oxide thin films. High optical transparency and simultaneously high electrical conductivity cannot be attained in intrinsic stoichiometric materials and the only way this can be accomplished is by creating electron degeneracy in a wide band gap (Eg > 3eV or more) material by introducing non-stoichiometry or appropriate dopants. Indium oxide is yet another oxide belonging to the TCO phase space. This section describes the properties of tin doped indium oxide, generally known as indium tin oxide (ITO), which is a well known highly degenerate, *n*-type TCO with

wide band gap. In the class of TCOs, ITO becomes the most favoured, since it offers the highest available transmission for visible wavelengths, together with lowest possible electrical resistivity. It is one of the most generally used transparent conductive oxides in optoelectronic applications, since it offers unsurpassed performance in terms of conductivity and optical transmission. Excellent chemical stability, reproducibility in production, possibility to fabricate films with better surface morphology and ability to deposit high quality films even at room temperature makes them superior in the class of transparent conductors [16].

In solar cells, ITO is used as transparent conducting top layer which allows light into the cell and electricity to flow out, and hence the efficiency of a solar cell can be improved by modifying the properties of top ITO layer. Depending on the method of fabrication and various corresponding deposition parameters, ITO layers can be crystalline or amorphous which influences the opto-electronic properties of the films. Apart from solar cells, ITO layers find applications in window coatings, energy efficient buildings, liquid crystal displays and flat panel displays, since it effectively reflects wavelengths in the infra red part of the spectrum.

4.6.1 Electronic structure and transparent conducting properties

The electronic band structure of a material provides information regarding the interplay between optical absorption and conduction in TCOs. The significant characteristics of such materials can be satisfactorily explained on the basis of a reliable model of electronic band structure, proposed by Fan and Goodenough on the basis of electron spectroscopy for chemical analysis (ESCA) measurements [27].

ITO has cubic bixbyite structure which is also known as the *c*-type rare earth sesqui oxide structure and is regarded as an imperfect crystal of fluorite, by removing 16 oxygen atoms for 1 bixbyite unit cell. 32 cations occupy the 8*b* and 24*d* positions as in figure 4.25, and each cation resides at the centre of a distorted cube, with oxygen anions occupying the six corners. All 8*b* cations are coordinated to six oxygen anions and to two oxygen interstitial positions, which lie along the body diagonal of a cube. The 24*d* cations are coordinated to six oxygen anions and to 2

oxygen interstitial sites along a face diagonal of the cube. The 48 oxygen anions are coordinated to four cations.

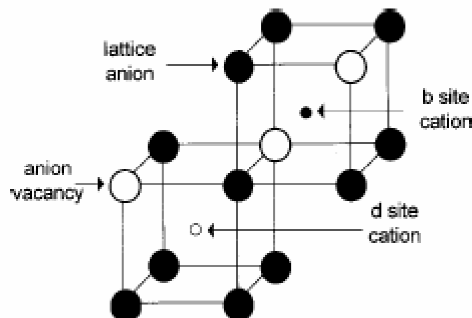

Figure 4.25 .Crystal structure of ITO

Indium tin oxide is created by substitutional doping of In_2O_3 with Sn^{4+}, which replaces the In^{3+} atoms from the bixbyite structure of indium oxide [27]. Tin exists as SnO or SnO_2 by forming an interstitial bond with oxygen with a valency of +2 or +4 respectively. The ultimate conductivity of ITO is influenced by this valency state. A net reduction in carrier density occurs at lower valence state, since a hole is created, which acts as a trap, thereby reducing the conductivity. At higher valency electrons are donated to the conduction band, thereby enhancing conductivity. Apart from this, oxygen vacancies contribute to the high conductivity in ITO films. When tin atoms are doped, the valence band gets shifted upwards and the conduction band downwards. Above the critical carrier density, the filling up of conduction band causes vacant sites in lower states and thereby an apparent widening of optical band gap.

4.7 Results and Discussion

In this work, RF magnetron sputtering technique was used to deposit thin films using an ITO target having an In_2O_3:SnO_2 composition of 90:10 percentage by weight. The yield of sputtering below 60 W was too low and above 200 W, the films were too thick. Hence, the sputter power during deposition was varied from 60W to 200W and the corresponding variations in the structural, electrical and optical features of the thin films were studied in detail. The rate of deposition of ITO films was optimised and the variations in yield of radio frequency magnetron

sputtering were studied for various ion energies. It follows the pattern as shown in figure 4.26. The sputtering parameters followed during deposition were as given in table 4.14.

Table 4.14 Experimental parameters of sputtering process

Target	ITO
Substrate	Quartz
Target–substrate distance	65 mm
Deposition (Ar) pressure	$4x10^{-2}$ m bar
Base pressure	$1x10^{-6}$ m bar
Deposition time	30 minutes
Substrate temperature	100^0C
RF power	60-200 W

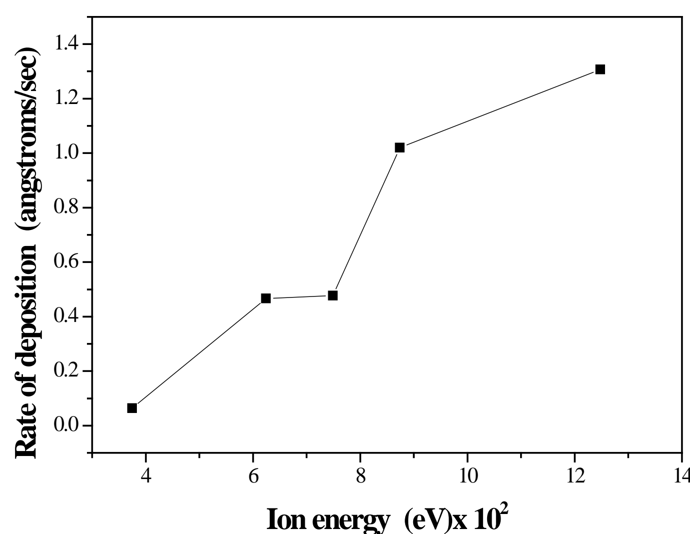

Figure 4.26 Yield of sputtering of ITO thin films

4.7.1 X-ray Diffraction

The Integrated Powder X-ray Diffraction software (PDXL) was used for the analysis of XRD pattern, complemented by International Centre for Diffraction Data (ICDD-2012) database. Figure 4.27 exhibits the room

temperature X-ray diffraction pattern of ITO films fabricated at substrate temperature of 100^0C with sputter powers ranging from 60-200W. The XRD plots were stacked by *y* offset intensities with respect to increasing sputter power.

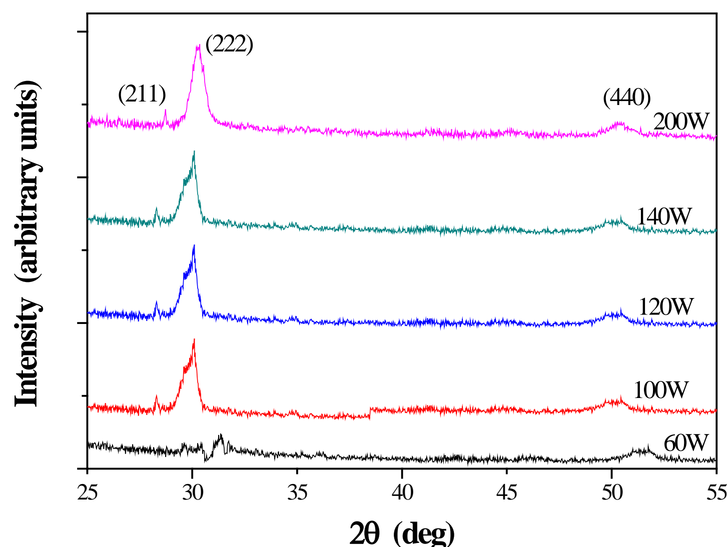

Figure 4.27 XRD pattern of ITO thin films

The XRD patterns of films sputtered at 60 W showed no intense peaks due to its lesser crystallinity and that at 200 W showed very sharp orientations in the (222) plane. The structure is found to be that of bixbyite indium tin oxide (JCPDS: 06-0416), belonging to space group Ia_3, with a lattice constant of 1.0117 nm. Even though the intensity of XRD peaks increases considerably with sputter power, all films exhibited the same reflecting planes.

Table 4.15 Crystallite size variations of ITO films with sputter power

Sputter power (W)	Crystallite size (nm)
60	-
100	17.8
120	23.2
140	28.7
200	31.7

The increase in peak intensity may be attributed to enhancement in crystallinity at higher sputtering power, since the sputter ions acquire sufficient energy to provide elevated translational kinetic energy to the ad-atoms, thereby causing surface diffusion, leading to growth of crystalline films [8]. The less intense peaks of the films sputtered at 60W made it impossible to calculate the crystallite size; all others were calculated and tabulated in table 4.15.

4.7.2 Scanning Electron Microscopy

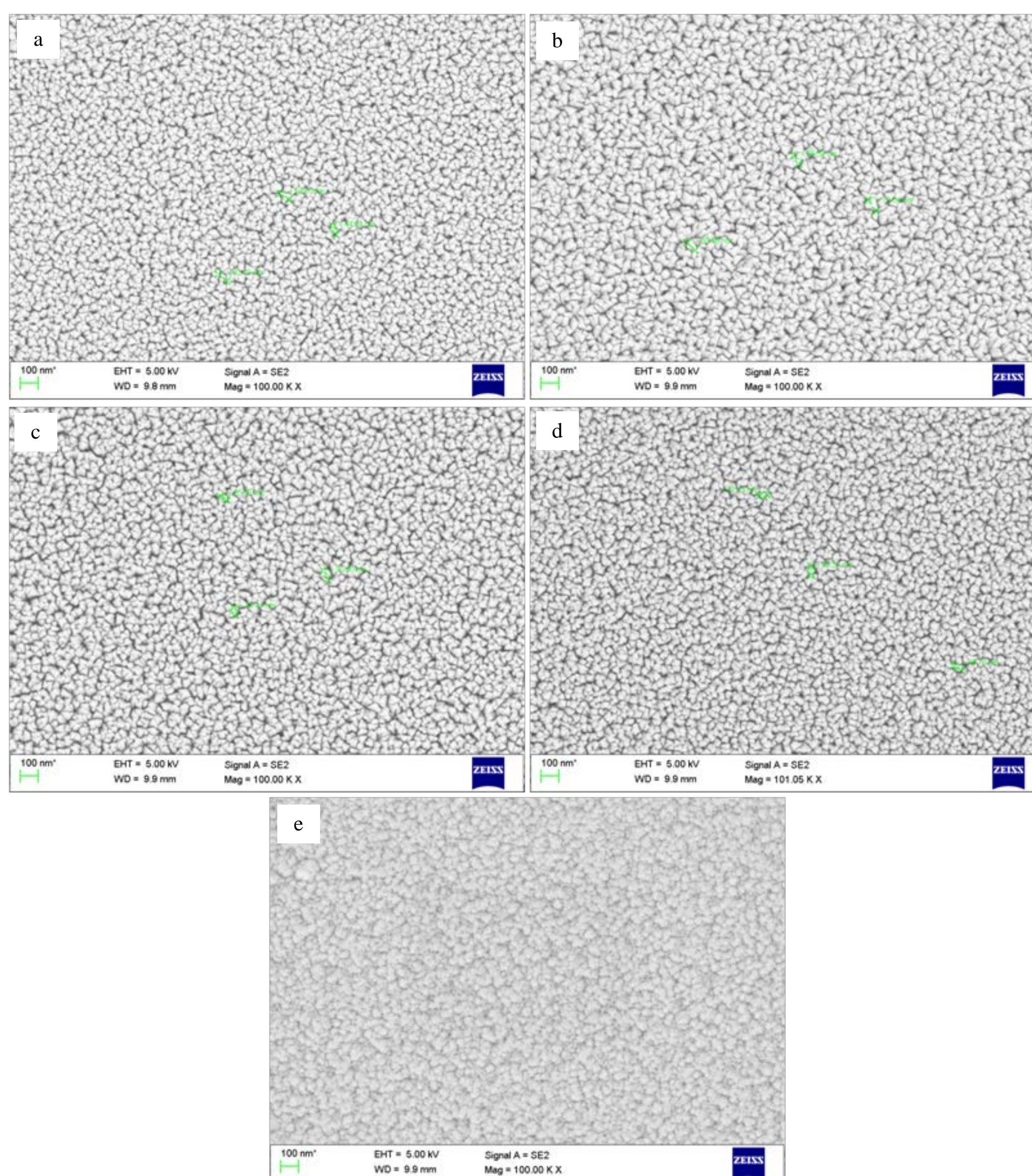

Figure 4.28 SEM images of ITO films sputtered at powers (a) 60 W, (b) 100 W, (c) 120 W, (d) 140 W and (e) 200 W

SEM images of the samples sputtered at different RF powers at substrate temperature of 100^{0}C are shown in figure 4.28, with same magnification. From these images, it can be inferred that as the sputter power is increased, there is slight increase in the crystallite size, which complement the results from diffraction pattern of corresponding samples. This can be attributed to the increased surface diffusion of ad-atoms due to larger mobility acquired from the generated plasma. The films sputtered at 120W and below showed definite crystallites uniformly distributed on the substrates, whereas above this value, the film surface showed the formation of large crystallites. This may be due to the non uniform scattering taking place at higher power, due to the very high energy of ionised plasma. In these films at higher powers, no definite particles were observable. Also, these may be conglomerates of many smaller sized grains in the samples that may be formed due to the greater energy imparted to the ions [21].

4.7.3 Energy dispersive spectra

Compositional analysis conducted using EDS proved the presence of indium, tin and oxygen in all samples. EDS spectra obtained for ITO films sputtered at 120W and 100^{0}C is shown in figure 4.29. Films grown at different sputter powers exhibited exactly similar spectra proving the absence of impurities and high quality of sputtered films.

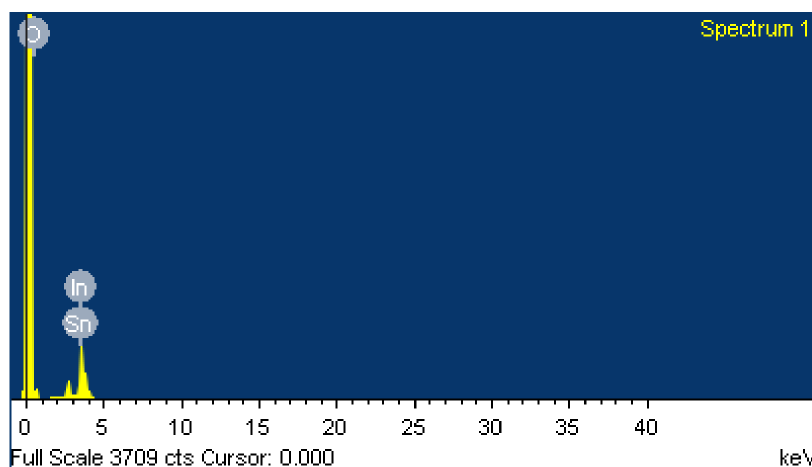

Figure 4.29 EDS spectra of the ITO film grown at 120W and 100^{0}C

4.7.4 Atomic Force Microscopy

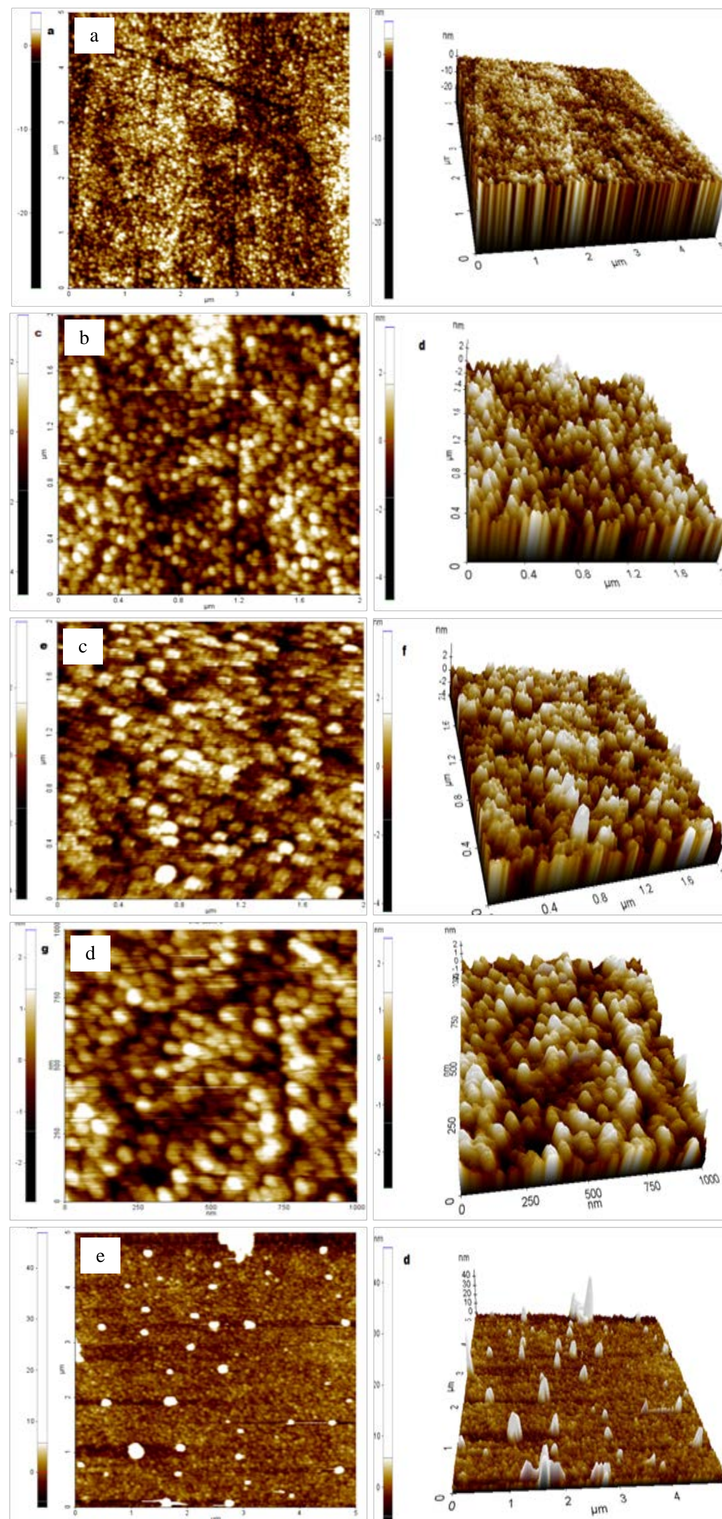

Figure 4.30 2 D and 3D AFM images of the films sputtered at (a) 60W , (b) 100W, (c)120W, (d) 140W and (e) 200W.

The surface morphologies of the samples deposited at various sputter powers were examined by Atomic Force Microscopy (AFM). The 2D and 3D surface topographies of the thin films deposited at various sputter powers at constant substrate temperature of 100^0C are shown in figure 4.30. The surface roughness calculated is tabulated in table 4.16.

The AFM images of samples coated on quartz substrates were taken at room temperature and ambient pressure conditions under non-contact mode. The intense growth of crystallites and uniform distribution of grains with increase in sputter power can be observed from these images. The surface mobility of ad-atoms increases with sputter power, which results in the formation of continuous and homogeneous films. Transfer of momentum takes place onto the substrate by the surface diffusion of ad-atoms and gets enhanced with sputtering power. For application in display systems and optoelectronic devices, one of the key parameters to be considered is the surface roughness of a TCO film, since it influences the carrier mobility and surface light scattering.

Table 4.16 Variation of RMS roughness with sputter power

Sputter Power (W)	RFM roughness (nm)
60	0.563
100	0.624
120	0.679
140	0.923
200	1.102

Four random areas over the surface were chosen and the root mean square (RMS) measurements were recorded to analyse the surface roughness of the sputtered thin films. RMS roughness increased with sputtering power as in table 4.16. For films deposited at a substrate temperature of 100^0C and 60 W, the lowest RMS value of surface roughness of 0.563 nm was observed and as the sputter power was increased to 200 W, the RMS value was 1.102 nm.

This trend of RMS roughness is related to crystallite size. At low sputtering power, the rate of deposition is lesser due to less energetic argon over the target species. This results in slow nucleation and growth of films onto the substrate surface.

4.7.5 Transmission electron microscopy

Figure 4.31 (a) is the TEM image of the ITO films sputtered at 120W and 100^0C at lower magnification.

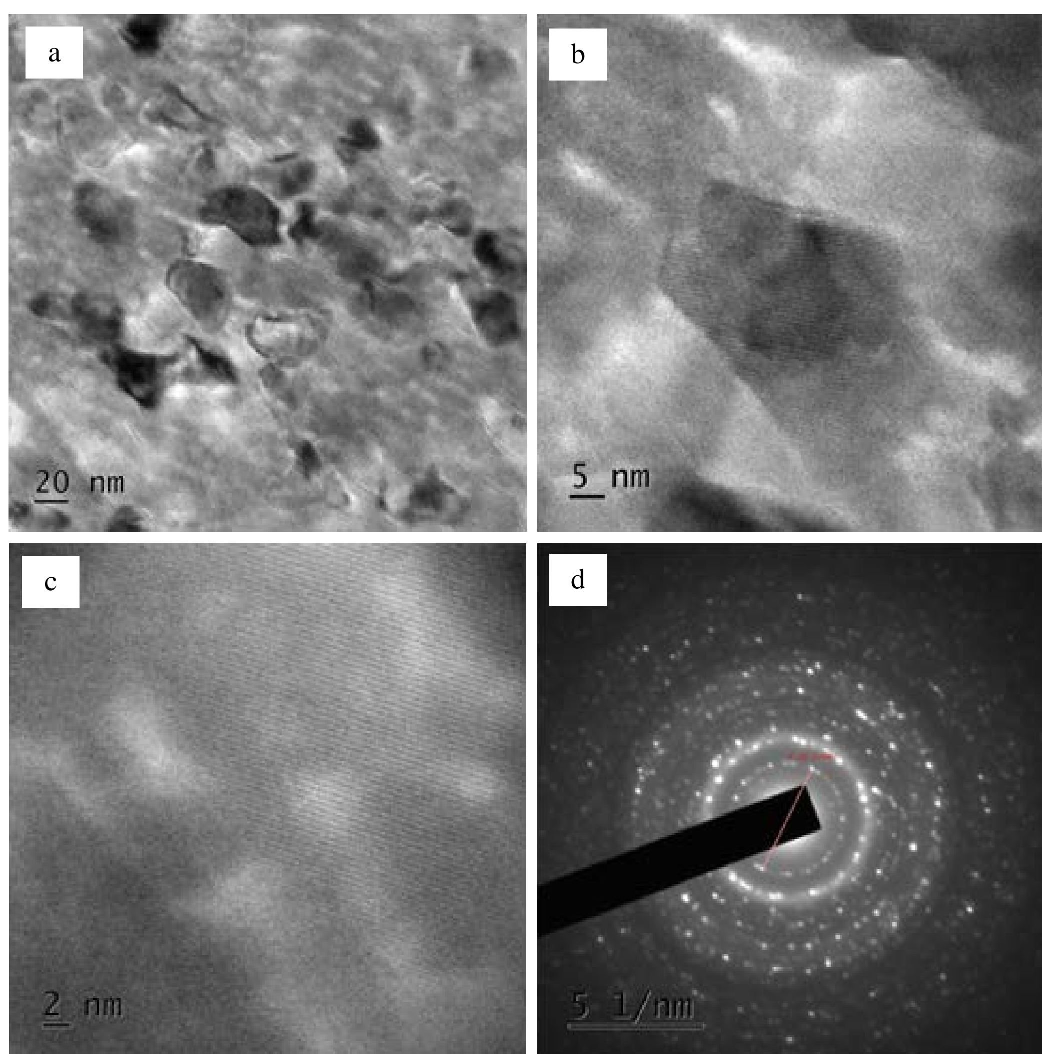

Figure 4.31 TEM images at (a)low resolution, (b) high resolution, (c) high resolution and (d) SAED pattern of ITO thin films sputtered at 120W and 100^0C

At higher magnification in figure 4.31 (b) and (c), the d- spacing of the lattice can be clearly observed, which confirms the crystalline arrangement of the atoms. Figure 4.31 (d) gives the SAED pattern of the same film, from which the diameter of one of the brightest ring was found and using that the d-spacing (table 4.17) of the lattice was found to be 0.488 nm, which is similar to that calculated from XRD pattern (0.423 nm).

Table 4.17 Comparison of d- spacing from TEM and XRD

Parameter	SAED	XRD
d spacing (222)	0.488 nm	0.423 nm

4.7.6 Optical profilometry

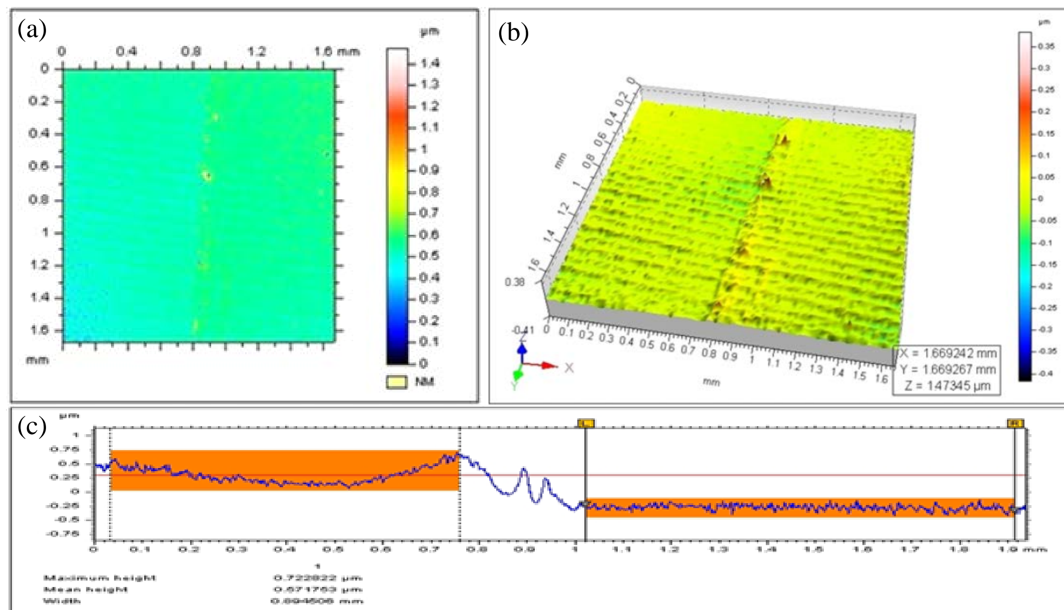

Figure 4.32 (a) 2D Optical profile, (b) 3D Optical profile and (c) line profile of the ITO film sputtered at 100^{0}C and 120W

Optical profilometry was used to study the surface topography of the films in two and three dimensions. A profile was made on the film by masking the substrate suitably by Kapton tape. Even and smooth nature of the surface can be observed in

figure 4.32 which is in agreement to the low RMS surface roughness obtained from AFM studies. The figure 4.32 (a) and (b) shows 2D and 3D optical profile of the ITO sputtered at 100^0C substrate temperature and sputter power of 120 W. From the line profile of the film in figure 4.32 (c), the thickness was found to be 571.75 nm being the average height of particle distribution and is found to be in accordance with the thickness measured by optical studies.

4.7.7 Hall measurements

The conductivity of sputtered thin films were analysed by Hall measurements. It is observed that the sputter power has a significant influence on the electrical properties. Table 4.18 and figure 4.33 (a) demonstrates the variations of charge carrier concentration and resistivity of thin films with respect to sputter power. It is observed that the carrier concentration increases almost linearly with the sputter power. At sputter power of 200 W, the film carrier concentration reaches 70.92 $x10^{18}/cm^3$, which is 2 orders higher than the value obtained for SnO_2 films sputtered at the same conditions, which was $3.113x10^{16}/cm^3$. At 60 W, the charge concentration is 4.313 $x10^{18}/cm^3$. The mobility of charge carriers follows an overall decreasing tendency with increase in sputter power as in figure 4.33 (b).

Table 4.18 Variation of electrical characteristics of ITO films with sputter power

Sputter Power (W)	Charge carrier concentration (electrons) ($/cm^3$)	Mobility (cm^2 / Vs)	Resistivity (Ω cm)
60	4.313 $x10^{18}$	15.70	9.217 $x10^{-2}$
100	2.55 $x10^{18}$	27.79	8.907 $x10^{-2}$
120	28.2 $x10^{18}$	8.643	2.561 $x10^{-2}$
140	31.13 $x10^{18}$	7.923	2.531 $x10^{-2}$
200	70.92 $x10^{18}$	4.251	2.071 $x10^{-2}$

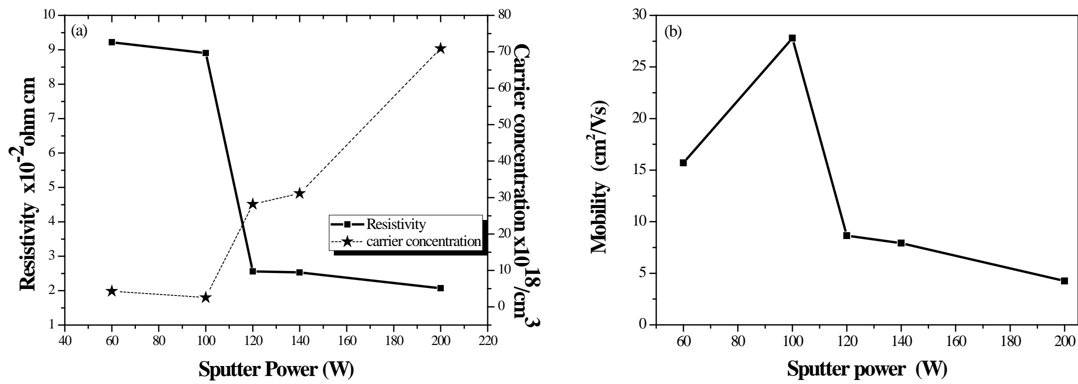

Figure 4.33 Variation of (a) resistivity and carrier concentration and (b) mobility with sputter power.

4.7.8 UV-Visible spectroscopy

The optical transmission spectra exhibited more than 3 maxima and minima of interference fringes which are indications of the highly uniform nature of film surface [24]. The average transmittance observed for the films is found to be above 80% in the visible range and much higher compared to SnO_2 films fabricated under similar experimental conditions. A strong absorption is observed in the UV range and the band gap energies are determined using Tauc plot as in the case of SnO_2 films [6]. Variation in optical transmission of the films with sputter power is shown in figure 4.34.

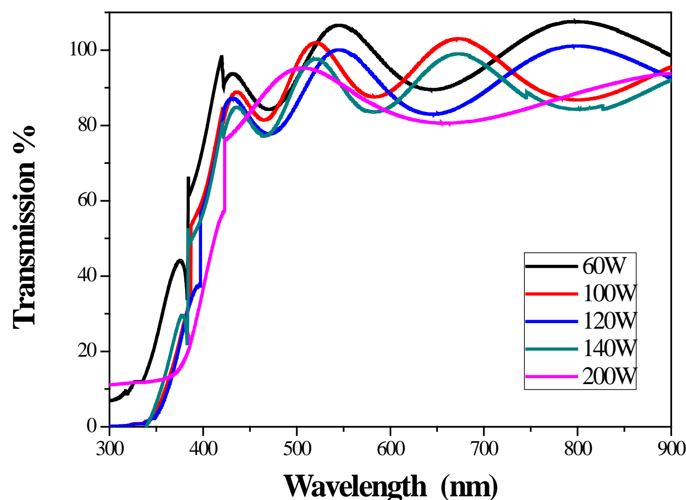

Figure 4.34 Optical transmission spectra of ITO films at different sputter powers

The reduction in transmittance with sputter power, as observed in the figure may be due to the enhancement in scattering of light at the surface, caused by an increase in the grain size [3, 29]. Also, since rate of deposition gets enhanced with power, thickness of film increases, resulting in lesser transmission.

Table 4.19 Variation of band gap energy with sputter power

Sputter power (W)	Bang gap energy (eV)
60	3. 469
100	3. 506
120	3.578
140	3. 614
200	3. 686

The band gap energies of samples deposited at different sputter powers are tabulated in table 4.19. It can be observed that the optical band gap energy increases from 3.469 to 3.686 eV, when the sputter power was varied from 60 W to 200 W. The Burstein-Moss effect can explain the broadening of band gap energy with the increasing carrier concentration [21]. The optical characteristics of the sputtered films substantiate the typical transparent conducting nature of the films by the absorption of photons at effective band gap in the near UV-region.

Table 4.20 Thickness variation with sputter power of ITO films

Sputter power (W)	Thickness of films (nm)
60	-
100	-
120	598.79
140	664.23
200	814.81

The value of film thickness obtained at different sputter powers are tabulated in table 4.20. The thickness of films at 60 W and 100 W could not be calculated as the number of fringes was lesser than required to calculate by this method. The band

gap of the films was estimated from the Tauc plot, as described earlier, given in figure 4.35.

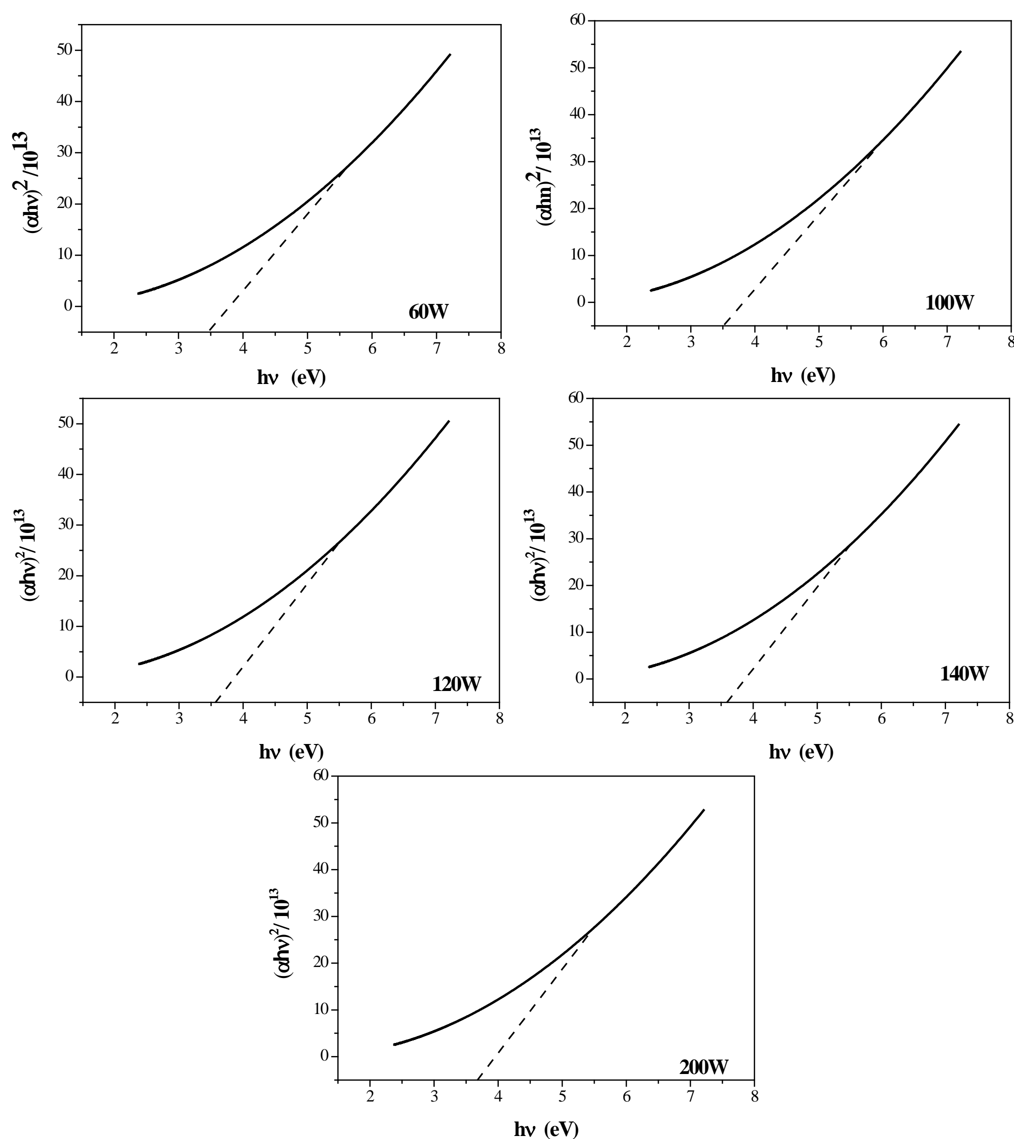

Figure 4.35 Tauc plot of ITO films at different sputter powers

4.7.9 X-ray Photoelectron Spectroscopy

The XPS of transparent conducting thin films of indium tin oxide grown at a sputter power of 120 W and substrate temperature of 100^0C was recorded similar to SnO_2 films described in the previous section. The scanning was performed for both survey of film surface for constituents and individual elements present. The spectrum of the film surface was calibrated by recording C*1s* core-level spectrum at

284.67 ± 0.1eV. Since the charging effect of the C*1s* calibration is standardized at 284.5eV in this report, the spectra of the elements will appear at an energy difference of 0.17eV. Figure 4.36 shows the calibrated spectra of carbon *1s*.

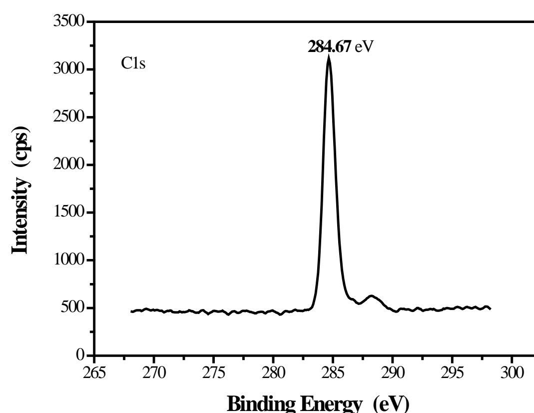

Figure 4.36 Carbon 1s spectra for XPS calibration of ITO spectra

Figure 4.37 shows narrow elemental scan of ITO thin films for In *3d* processed through CASA. The shape reveals no spectral asymmetry and the peaks were fitted with single Gaussian component. Analysis of XPS spectra shows the oxygen binding with indium in its +3 oxidation state on the film surface. In figure 4.37, In *3d* peak is composed of two different symmetrical curves located with a peak separation of 8.54 eV. The peaks are well known In $3d_{3/2}$ and In $3d_{5/2}$ peaks, from the *j-j* coupling of spins of electron with its angular momentum.

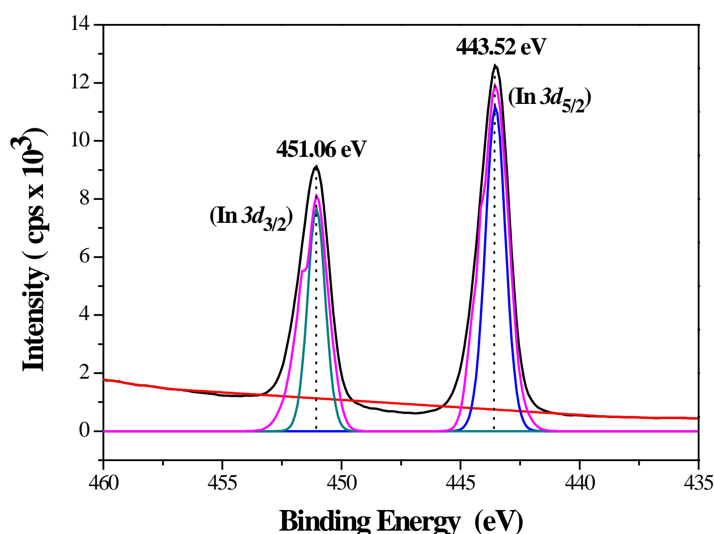

Figure 4.37 Narrow scan analysis of indium in sputtered ITO films

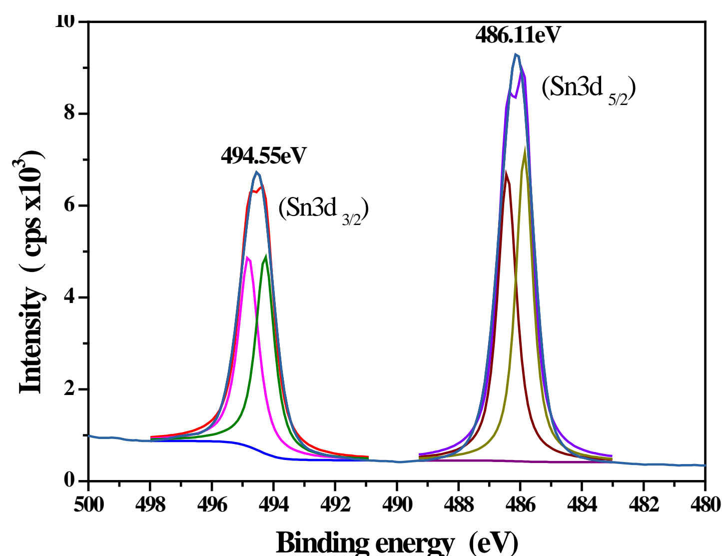

Figure 4.38 Narrow scan analysis of tin in sputtered ITO films

In figure 4.38, Sn *3d* peaks, found at binding energies of 486.11 eV and 494.55 eV is designated as the Sn $3d_{5/2}$, Sn $3d_{3/2}$ spin-orbit doublets accordingly. The raw data of Sn *3d* scan are also refined through CASA for further analysis and the Sn $3d_{3/2}$ and Sn $3d_{5/2}$ emissions are fitted with single Lorentzian-Gaussian component. This confirms the presence of $Sn4^{+}$ and the absence of defective SnO_2 or SnO on the surface of thin films.

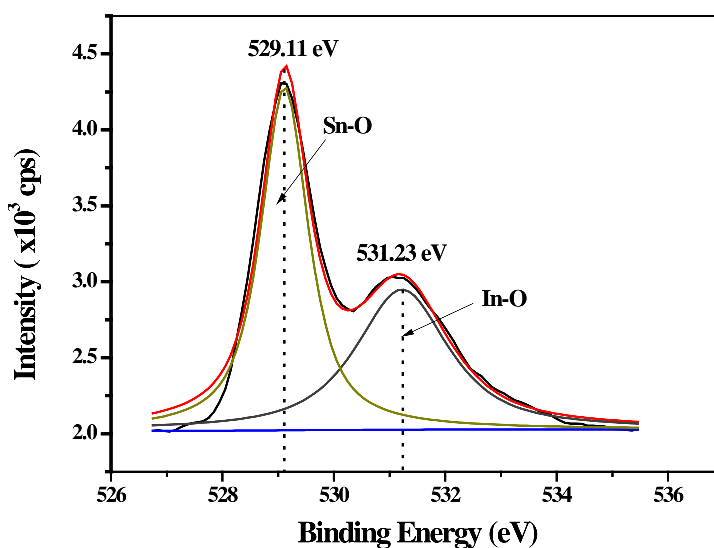

Figure 4.39 Narrow scan analysis of oxygen in sputtered ITO films

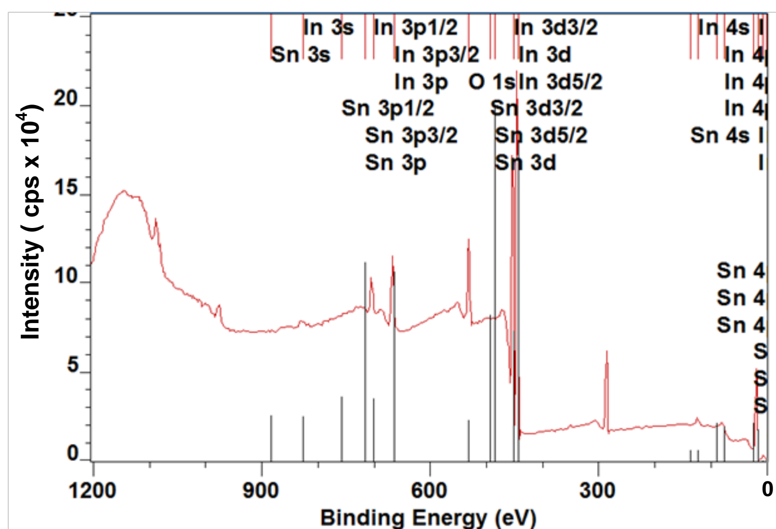

Figure 4.40 Survey scan spectrum of ITO films

The separation energy of XPS peaks is proportional to the *j-j* coupling constant dependent on the value of $1/r^3$ for a particular orbit (where r is its radius) [30]. The Sn-O bond in O *1s* spectra (figure 4.39) can be considered as a strong evidence for valence stability of Sn ions in ITO thin films. The O*1s* spectrum in figure 4.39 clearly indicates the presence of asymmetry related multiple oxidation states of oxygen with indium and tin in ITO films. The deconvolution of the O*1s* spectra is fitted perfectly below the chi square of 1 with two Lorentzian–Gaussian components centered at 529.11 eV and 531.23 eV, are attributed to the bonding of Sn^{4+}-O and In^{3+} -O in the film respectively. Figure 4.40 gives the wide scan spectrum of ITO thin films.

4.7.10 Optical transparency of the film

Figure 4.41 Actual photograph of ITO films sputtered at 120W and 100^0C

The photograph in figure 4.41 shows the high transparency of the ITO film sputtered at 120 W and 100^0C substrate temperature on quartz substrate. It is obvious that the optical transmittance is high for ITO films (~96%) compared to SnO_2 films (~80%) fabricated under similar conditions.

4.8 Conclusions

- Highly uniform and crack free *n*-type conducting thin films of tin (IV) oxide and tin doped indium oxide were fabricated on quartz substrates via radio frequency magnetron sputtering.
- The effects of sputter power and substrate temperature during the fabrication process on SnO_2 films were investigated.
- The influence of variation in sputter power during the fabrication of ITO films was also investigated.
- The detailed structural studies were conducted by X ray diffraction analysis and X ray photoelectron spectroscopy for all films.
- Compositional analysis was done using energy dispersive spectroscopy and thin film thickness was calculated using optical profilometer.
- Electrical behaviour was studied using Hall measurements and morphological studies by atomic force microscopy and scanning electron microscopy.
- The resistivity of ITO films was found to be less, along with a higher carrier concentration, compared to tin (IV) oxide films. Also optical studies reveal much higher transmittivity of above 90% in the visible range of electromagnetic spectra for the ITO films, compared to ~ 80% for the SnO_2 films under same experimental conditions.
- Taking all aspects of a good TCO into consideration and for the realisation of practical transparent electronic circuits, ITO was chosen for the rest of our studies.

References

[1] Henderson P. S., Kelly P. J., Arnell R. D., Backer H. and Bradley J. W., Surface and Coatings Technology, 174–175 (2003) 779.

[2] Savaloni H., Taherizadeh A. and Zendehnam A., Physica B: Condensed Matter, 349 (2004) 44.

[3] Noormariah Muslim, Y.W. Soon, C.M. Lim and N.Y. Voo, ARPN Journal of Engineering and Applied Sciences, 10 (2015) 7184.

[4] R. Wuhrer and W.Y. Yeung, Scripta Materialia, 49 (2003) 199.

[5] Prasonk Sricharoenchai, Nurot Panich, Patama Visuttipitukul and Panyawat Wangyao, Materials Transactions, 51 (2010) 246.

[6] Z. Ghorannevis, M. T. Hosseinnejad, M. Habibi and P. Golmahdi, Journal of Theoretical and Applied Physics, 9 (2015) 33.

[7] Kah-Yoong Chan and Bee-San Teo, Microelectronics Journal, 38 (2007) 60.

[8] C. H. Choi, W. I. Cho, B. W. Cho, H. S. Kim, Y. S. Yoon and Y. S. Tak , Electrochemical and Solid-State Letters, 5 (2002) A14.

[9] Kah-Yoong Chan and Bee-San Teo, Journal of Materials Science, 40 (2005) 5971.

[10] http://www.shinetsu.co.jp/en/products/pdf/garasu.pdf.

[11] http://www.ceramicindustry.com/articles/93165-sputtering-target-innovations

[12] Francis Boydens, Wouter Leroy, Rosita Persoons and Diederik Depla, Physica Status Solidi A, 209 (2012) 524.

[13] G. F. Iriarte, J. G. Rodriguez and F. Callen Microsystem Technologies, 17 (2011) 381.

[14] Z. Ghorannevis, M. T. Hosseinnejad, M. Habibi and P. Golmahdi, Journal of Theoretical and Applied Physics, 9 (2015) 33.

[15] M. Einollahzadeh-Samadi and R.S. Dariani, Applied Surface Science, 280 (2013) 263.

[16] A. Salehi, Thin Solid Films, 324 (1998) 214..

[17] J. L. Andujar, E. Bertran, A. Canillas, J. Campmany, and J. L. Morenza, Journal of Applied Physics, 69 (1991) 3757.

[18] H.A. McMaster, U.S. Patent 2, 429, 420 (1947).

[19] Clark I. Bright, 50 Years of Vacuum Coating Technology and the Growth of the Society of Vacuum Coaters, Society of Vacuum Coaters (2007).

[20] T. J. Coutts, D. L. Young and X. Li, MRS Bulletin, 25 (2000) 58.

[21] Antonio Facchetti and Tobin J. Marks, Transparent Electronics (2010) John Wiley & Sons Ltd.

[22] D. M. Bylander and L. Kleinman, Physica Review B, 41 (1990) 7868.

[23] Shi Junfei, Dong Chengyuan, Dai Wenjun, Wu Jie, Chen Yuting and Zhan Runze, Journal of Semiconductors, 34 (2013) 084003-1.

[24] W. L. Dang, Y. Q. Fu, J. K. Luo, A. J. Flewitt and W. I. Milne, Super lattices and microstructures, 42 (2007) 89.

[25] A. Ismail and M. J. Abdullah, Journal of King Saud University – Science, 25 (2013) 209.

[26] G. Anil Kumar, M. V. Raman Reddy and Katta Narasimha Reddy, IOP Conf. Series: Materials Science and Engineering, 73 (2015) 012133.

[27] C. C. Fan and J. B. Goodenough, Journal of Applied Physics, 48 (1977) 3524.

[28] David S Ginley, Handbook of Transparent conductors (2010) Springer New York.

[29] S. Schiller, G. Beister, W. Sieber, G. Schirmer and E. Hacker, Thin Solid Films, 82 (1981) 239.

[30] T. Yamashita and P. Hayes, Applied Surface Science, 254 (2008) 2441.

CHAPTER 5

STUDIES ON *p*-TYPE TRANSPARENT CONDUCTING OXIDES

5.1 Introduction

Highly transparent, *p*-type conducting crystalline thin films have recently gained remarkable attention in the field of active devices, especially in the optoelectronics technology, known as ‘‘Invisible Electronics" [1]. Even though TCOs have wide range of applications, very little work has been done on active device fabrication using TCOs. This is because TCOs currently used are largely *n*-type, but complementary *p*-type TCOs, essential for junction devices, is not much popular [2].

In 1997, Kawazoe et al. from Tokyo Institute of Technology, Japan, reported *p*-type conductivity in a highly transparent thin film of copper aluminium oxide ($CuAlO_2$) [3]. This has opened up a new field in optoelectronics device technology, the so-called *transparent* electronics or *invisible* electronics, where a combination of *n* and *p*-TCOs in the form of a junction could lead to a functional window, which transmits visible portion of solar radiation and simultaneously generates electricity by the absorption of UV radiation [4].

Semitransparent *p*-type conducting thin film of nickel oxide (NiO) was reported by Sato et al. [5] which had almost 40% transparency in the visible region. They also fabricated a TCO diode of the form *p*-NiO/i-NiO/i-ZnO/*n*-ZnO, but the transparency was very low; only about 20%. This was not favourable for device applications; nevertheless it was an important milestone in the development of TCOs and optoelectronics technology. The applications of TCOs are based on the fact that the material possesses a wide band gap, and hence visible photons cannot excite electrons from valence band to conduction band [6]. But they possess enough energy to excite electrons from donor level to conduction band (for *n*-type TCO) or holes from acceptor level to valence band (for *p*-type TCO). These acceptor or donor levels are created in TCOs by introducing non-stoichiometry or appropriate dopants.

Intense works are going on in this direction to fabricate new *p*-TCOs by various deposition techniques and for proper understanding of their structural, optical and electrical characteristics. Non-stoichiometric and doped versions of

many novel *p*-type transparent conducting oxides (*p*-TCO) with improved optical and electrical properties have been synthesized in the last few years.

In this work, we explore two different *p*-TCO films, for the fabrication of all-transparent active devices such as hetero junction diodes. We have selected copper (II) oxide or cupric oxide and indium doped copper oxide as *p*-type TCOs. This chapter deals with detailed structural, optical and electrical investigations on these two materials.

5.2 Copper oxide

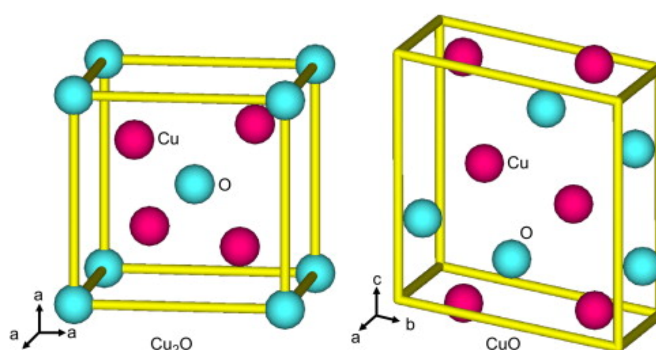

Figure 5.1 Crystal structure of CuO and Cu_2O

There exist two stable forms of copper oxide, namely, cupric oxide, CuO and cuprous oxide Cu_2O as in figure 5.1. Cupric oxide (CuO) has a preferred monoclinic tenorite structure, in which each copper atom is co-ordinated to four co-planar oxygen atoms at the corners of a parallelogram. It is a *p*-type transition metal oxide and the conductivity is mainly contributed by copper vacancies [7]. The direct band gap is in the range of 1.2 - 2.1 eV, depending on the deposition methods.

Cuprous oxide (Cu_2O) or cuprite has a cubic structure in which each oxygen atom is enclosed by a tetrahedron of copper atoms and each copper atom is coordinated to two oxygen atoms, forming linear units. It is a *p*-type conducting material with optical band gap ranging from 2.1-2.6 eV. It is usually difficult to obtain a single phase CuO, without mixtures of Cu, CuO and cuprous oxide (Cu_2O) phases [8]. Multi phased CuO crystalline thin films with atmospheric-pressure CVD and sol-gel-like methods were reported previously [9, 10]. Similarly multi phases

were obtained by reactive sputtering of copper target under different growth conditions [11].

In this work, we report the growth and characterizations of CuO thin films on quartz substrate by radio frequency (RF) magnetron sputtering method in two ways. The first is by using a CuO target under oxygen free environment and the second by using a metallic copper target under reactive sputtering in oxygen environment. Detailed investigations on the structural, optical and electrical properties of the deposited films were conducted.

5.2.1 Electronic structure and transparent conducting properties

Successful introduction of holes by substitutional doping or producing non-stoichiometry within a material causes strong localization of holes at oxygen *2p* levels or upper edge of the valence band due to the high electronegative nature of oxygen. This localization is due to the ionicity of metallic oxides. O *2p* levels lie far lower than the valence orbit of metallic atoms, leading to the formation of a deep acceptor level by the holes [12]. These holes have high probability to be localized around the oxygen atoms and hence they require high energy to overcome a large barrier height to migrate within the crystal lattice, resulting in poor conductivity and hole mobility. This can be resolved by making metal-oxygen bonds induce the formation of an extended valence band structure, i.e. modification of the valence band edge by mixing orbitals of appropriate counter cations with filled levels having energies comparable to the O *2p* level. This would reduce the strong coulombic force by oxygen ions thereby delocalizing the holes.

The unavailability of *p*-type TCOs are due to the difficulty in their design owing to their electronic band structures [13]. The valence band maximum should have a low effective mass to give shallow acceptor levels, which is hard to achieve in practice. The closed shell could be s^2 or p^6 system; the common being a p^6 system. The complexity is due to oxygen *2p* states which forms non-bonding levels at the top of the valence band. Non-bonding states always have a high effective mass and if the bond ionicity is large, they may possess larger mass [14]. This can be resolved by using a cation with closed shells and are degenerate with oxygen *2p* states.

Copper and silver compounds with delaffosite structures can be used as *p*-TCOs since they have appropriate d^{10} states. The metal states interact with some of the O *2p* states, pushing up a more dispersive band above the non-bonding O *2p* or Cu *3d* states. This band has a lower effective mass. Visible photons (2.1-3.1 eV) do not have enough energy to excite electrons from valence band to conduction band, but have enough energy to excite holes (for *p*-type) from acceptor level to valence band or electrons (for *n*-type) from donor level to conduction band.

5.3 Results and discussion

The sputter deposition of *p*-type conducting copper oxide films were performed as two separate experiments; one by varying the sputter power and second by varying the substrate temperature. Detailed structural, morphological, optical and electrical characterisations were performed and the results are discussed in the subsequent sections.

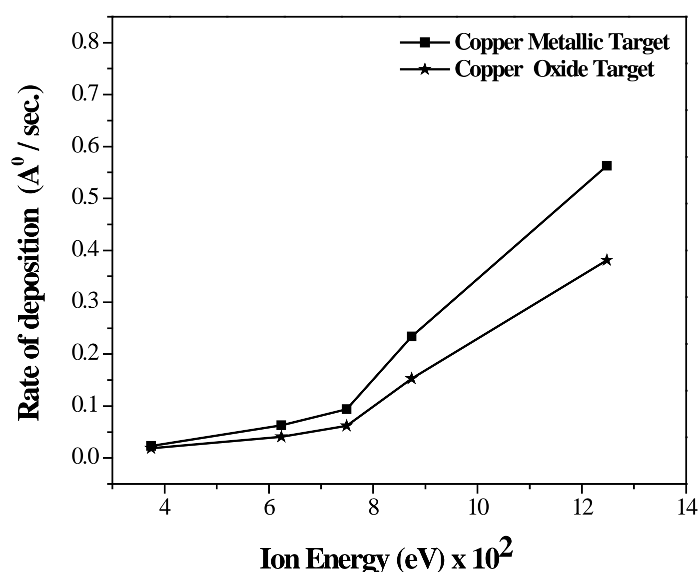

Figure 5.2 Yield of sputtering of CuO thin films

The rate of deposition have been studied for a wide range of sputter powers and optimised. Figure 5.2 shows the variations in yield of radio frequency magnetron sputtering at various ion energies. The optimum experimental parameters followed during deposition in our work is given in table 5.1

Table 5.1 Experimental parameter details used for sputtering process

Parameter	Details
Target	(i) CuO target in oxygen free atmosphere (ii) Cu metallic target in oxygen atmosphere
Substrate	Quartz
Target–substrate distance	70 mm
Deposition (Ar) pressure	4×10^{-2} m bar
Base pressure	1×10^{-6} m bar
Deposition time	30 minutes
RF power (W)	60-200 W
Substrate temperature	25^0C - 200^0C

5.3.1 X-ray Diffraction

XRD analysis was carried out using Integrated Powder X-ray Diffraction software (PDXL) complemented by the database, International Centre for Diffraction Data (ICDD-2012).

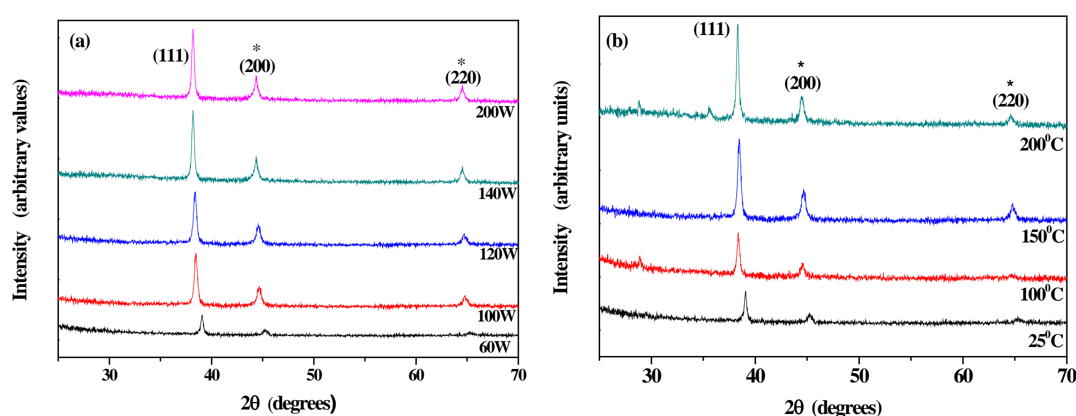

Figure 5.3 XRD pattern of CuO films with varying (a) sputter power and (b) substrate temperature using oxide target

Figure 5.3(a) exhibits the room temperature X-ray diffraction pattern of CuO thin films sputtered using oxide target at a substrate temperature of 150^0 C for 30 minutes at sputter powers ranging from 60-200W and figure 5.3(b) shows that sputtered at 140W for 30 minutes with varying substrate temperature. The resulting plots are stacked by *y*-offset intensities and it confirms the polycrystalline nature of thin films.

In XRD pattern, the reflections from (111) plane at 2θ value 38.61^0 corresponds to the most preferred orientation of CuO monoclinic structure with JCPDS card number 01-080-1916, space group Cc9. But smaller peaks can be observed (marked with *), which can be identified as reflections from the (200) and (220) planes of cubic Cu_2O structure with card number 05-0667. When oxide targets are used for sputtering in oxygen free environment, there are chances of forming Cu_2O along with CuO [15, 16]. The amount of oxygen may be lesser, leading to less favoured formation of CuO. However, formation of CuO have been observed from XRD and confirmed by XPS spectra.

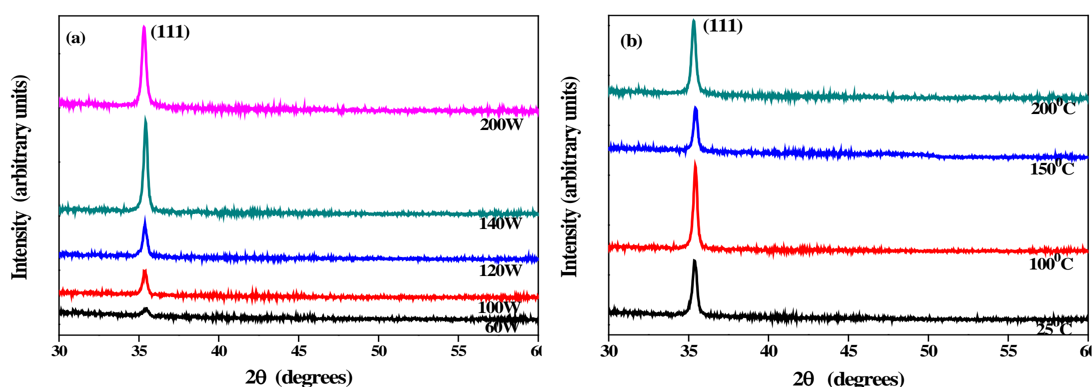

Figure 5.4 XRD pattern of CuO films with varying (a) sputter power and (b) substrate temperature using metallic target

In the XRD pattern of films sputtered using a metallic target in oxygen ambience (figure 5.4), the peaks corresponding to Cu_2O phase are absent, indicating the formation of phase pure CuO structure. The reflections from (111) plane is observed. In this case, since the reaction chamber is filled with oxygen, the Cu_2O formed must have oxidised to CuO as follows,

$$2Cu_2O + O_2 \rightarrow 4CuO \quad (5.1)$$

5.3.2 Scanning Electron Microscopy

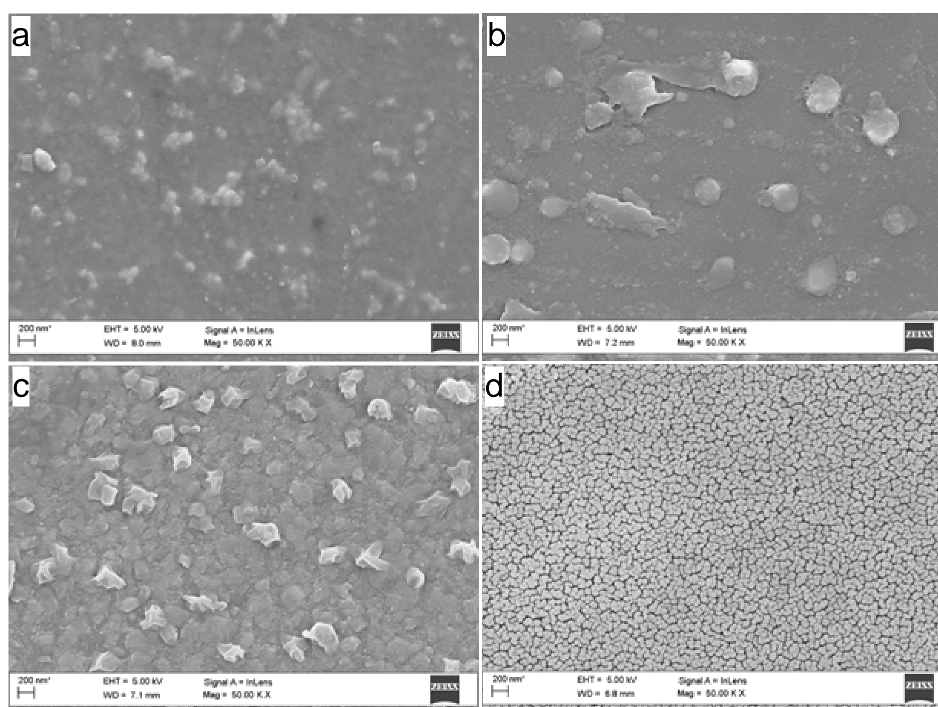

Figure 5.5 SEM images of CuO films sputtered using oxide target at powers (a) 60W, (b) 100W, (c) 140W and (d) 200W

SEM images of the samples sputtered using oxide target at various RF powers at a substrate temperature of 150^0C are shown in figure 5.5, under same magnification. As the sputter power is increased, there is increase in the crystallite size, homogeneity and uniformity of the thin films. This may be due to the amplified surface diffusion of ad-atoms owing to their higher mobility. Films sputtered at 140W and below showed large crystallites scattered on the substrates but, at 200W, they exhibit uniformly distributed grains. At higher powers, conglomerates of smaller grains can be observed, which may be the result of greater energy imparted to the ions [4].

Figure 5.6 shows the films sputtered using oxide target at different substrate temperatures and at a sputter power of 140 W. At room temperature (25^0C), the film appears non-homogeneous, probably due to less adhesion to the substrate, whereas, at higher temperatures, it shows good homogeneity and uniformly distributed grains. Using metallic target under oxygen ambience yields films that are more homogeneous, which is observed from the SEM images in figures 5.7 and 5.8. The

uniformity of films increases with increase in sputter power and substrate temperature.

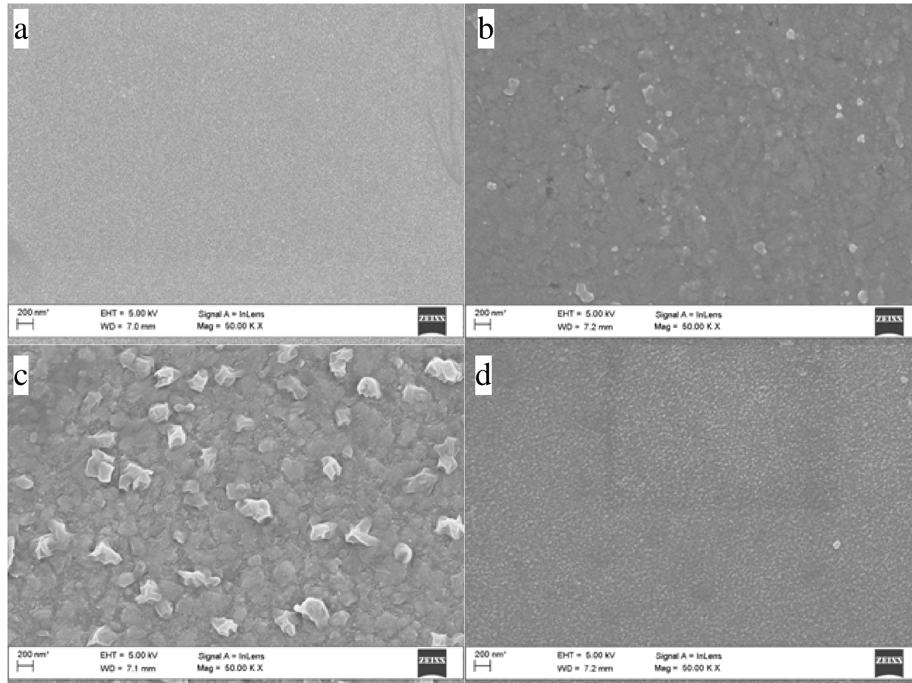

Figure 5.6 SEM images of CuO films sputtered using oxide target at substrate temperatures (a) 25^{0}C (b) 100^{0}C (c) 150^{0}C and (d) 200^{0}C

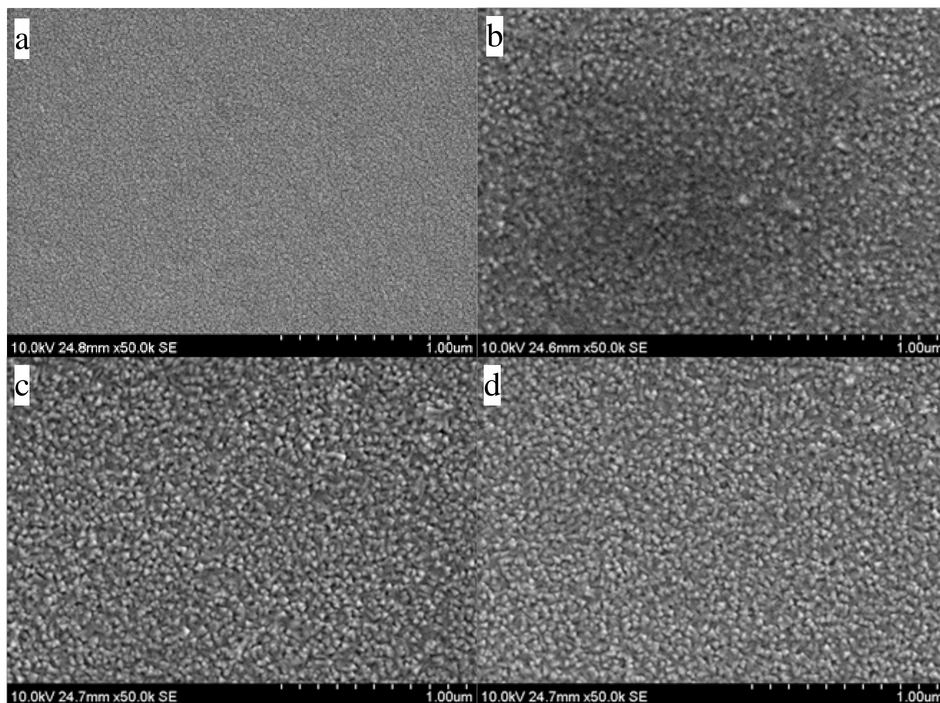

Figure 5.7 SEM images of CuO films sputtered using metallic target at a substrate temperature of 150^{0}C and powers (a) 60W, (b) 100W, (c) 140W and (d) 200W

At room temperature (25^0C) the crystallites are observed to be small when compared to that at higher temperatures. This may possibly be due to the enhancement in crystallinity at higher temperatures.

Comparing all the SEM images, it can be observed that the homogeneity of the thin film samples is much higher for those fabricated using metallic target in oxygen atmosphere. This may be due to the higher density of metal target used. For display applications, films with greater uniformity are preferred and hence, sputtering of metal target under oxygen atmosphere may be preferred.

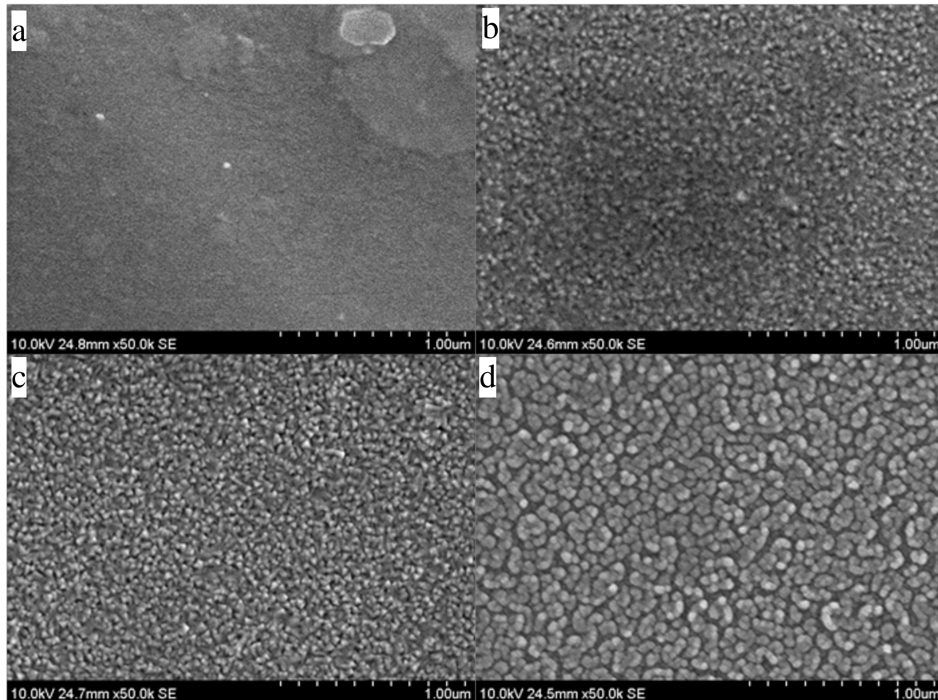

Figure 5.8 SEM images of CuO films sputtered using metallic target at 140 W sputter power and substrate temperatures (a) 25^0C (b)100^0C (c) 150^0C and (d)200^0C

5.3.3 Energy dispersive spectra

Figure 5.9 (a) and (b) shows the EDS spectra of CuO films sputtered at 150^0C and 140 W using oxide target and metallic target respectively. The EDS spectra confirm the presence of copper and oxygen in both the samples. The presence of trace amounts of carbon impurity can be identified in the EDS spectra of

samples using oxide target, whereas it is absent in films sputtered using metallic target.

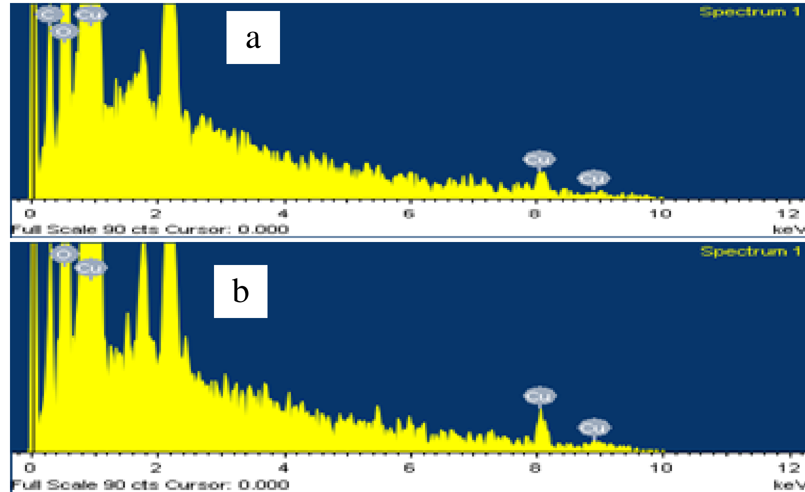

Figure 5.9 EDS spectra of the thin films sputtered using (a) oxide target and (b) metallic target

5.3.4 Atomic Force Microscopy

The 2D and 3D atomic force micrographs of films sputtered using oxide target and metallic target at substrate temperature of 150^0C and different sputter powers are given in figures 5.10 and 5.11. Micrographs of films sputtered at different substrate temperatures for both targets are not included in this thesis. However the RMS surface roughness calculated from the AFM are tabulated in table 5.2 and 5.3. The uniformity of films increased with sputter power and substrate temperature. However the surface roughness were found to be lower for the films sputtered using copper metallic target compared to oxide target fabricated under similar conditions. RMS surface roughness was computed as variations in height profile of the films. Similar to the previous reports, due to increase in thickness and surface energy of ad-atoms, surface roughness was found to increase with sputter power as well as substrate temperature in both cases. Also, the 3D AFM images confirm the homogenous distribution of grains and dense growth of crystallites with increase in sputter power and substrate temperature. Similar results were obtained using Scanning Electron Microscopy.

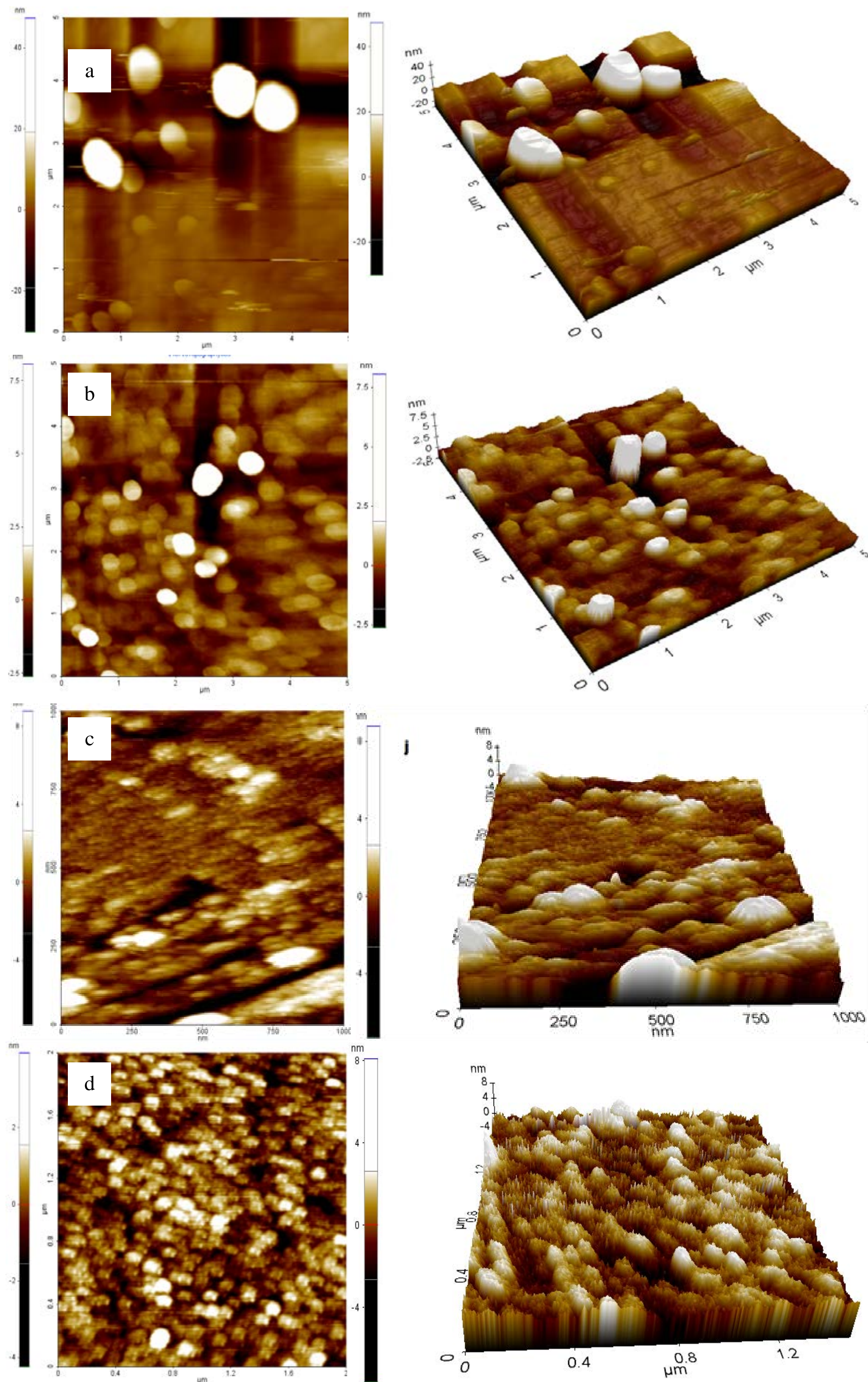

Figure 5.10 2D and 3D AFM images of CuO films using oxide target at powers (a) 60W, (b) 100W, (c) 140W and (d) 200W

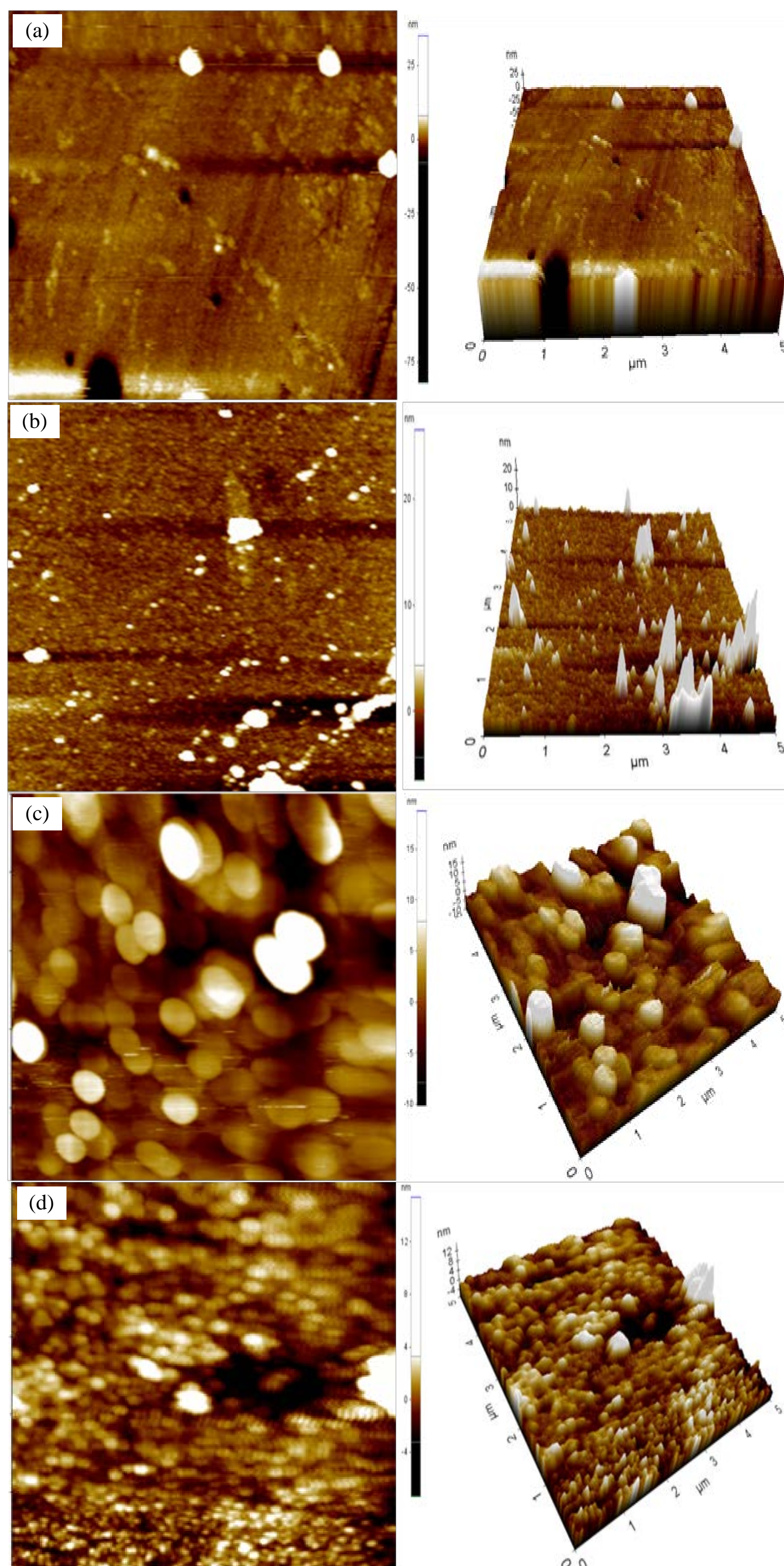

Figure 5.11 2D and 3D AFM images of CuO films using metallic target at (a) 60W, (b) 100W, (c) 140W and (d) 200W

Table 5.2 RMS roughness variations of films sputtered using oxide target with (a) sputter power and (b) substrate temperature

(a)

Sputter power (W)	RMS (nm)
60	2.422
100	2.555
140	2.609
200	2.725

(b)

Substrate temperature	RMS (nm)
25^0C	2.135
100^0C	2.555
150^0C	2.609
200^0C	2.694

Table 5.3 RMS roughness variations of films sputtered using metallic target with (a) sputter power and (b) substrate temperature

(a)

Sputter power (W)	RMS (nm)
60	1.042
100	1.154
140	1.264
200	1.731

(b)

Substrate temperature	RMS (nm)
25^0C	1.006
100^0C	1.163
150^0C	1.264
200^0C	1.412

5.3.5 Transmission Electron Microscopy

The TEM images of CuO film sputtered using metallic target in oxygen ambience at 150^0C substrate temperature at sputter power of 140W under different magnifications are shown in figure 5.12 (a), (b) and (c). This film was chosen in particular since these deposition parameters were found to be optimum for enhanced TCO properties. It shows the highly smooth surface, which is the cause for high optical transparency of the films. Figure 5.12 (d) gives the SAED pattern of the sputtered films. The bright rings indicate the polycrystalline nature of the films. The *d*-spacing of the most prominent peak from the (111) plane of the films computed using SAED pattern and that generated by XRD are tabulated in table 5.4.

Table 5.4 Comparison of d-spacing from TEM and XRD

Parameter	SAED	XRD
d-spacing (111) plane	0.218 nm	0.233 nm

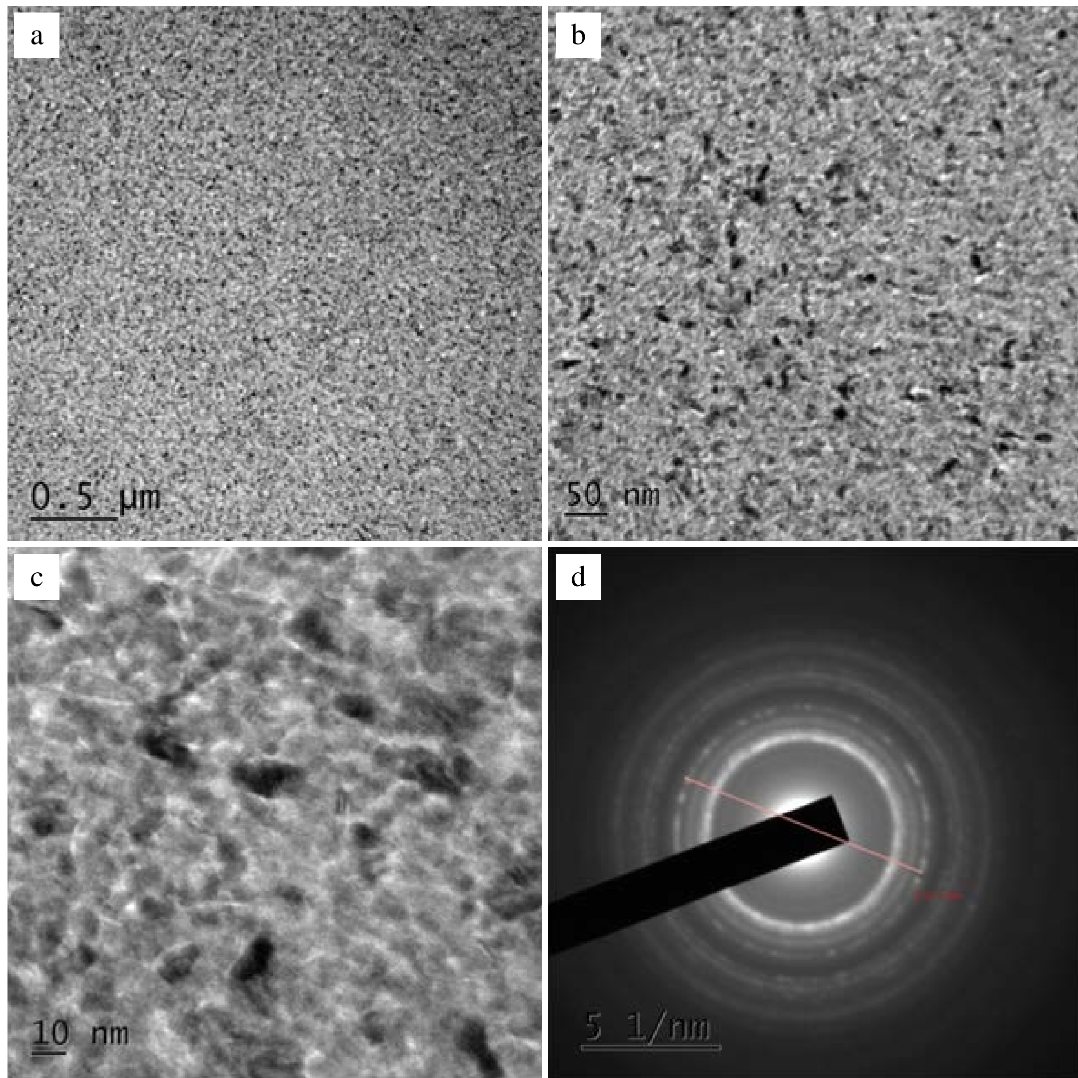

Figure 5.12 TEM images at (a) low resolution, (b) and (c) high resolution and (d) SAED pattern of CuO films

5.3.6 Optical Profilometry

The optical profile of the films was acquired by making a profile on the surface by masking during fabrication. Figure 5.13 (a) and (b) shows the 2D optical

profile and 3D optical profile of CuO film sputtered at 150^{0}C and 140 W using a metallic target. The line profile of the CuO films sputtered using metallic target is shown in figure 5.13 (c), which gives us the approximate thickness of the film as 0.214 µm. 2D and 3D optical profile of CuO film sputtered using oxide target at 150^{0}C and 140 W can be seen in figure 5.14 (a) and (b) respectively. Its line profile is also provided in figure 5.14 (c). We have obtained approximate thickness of the film as 0.8944 µm when sputtered using oxide target.

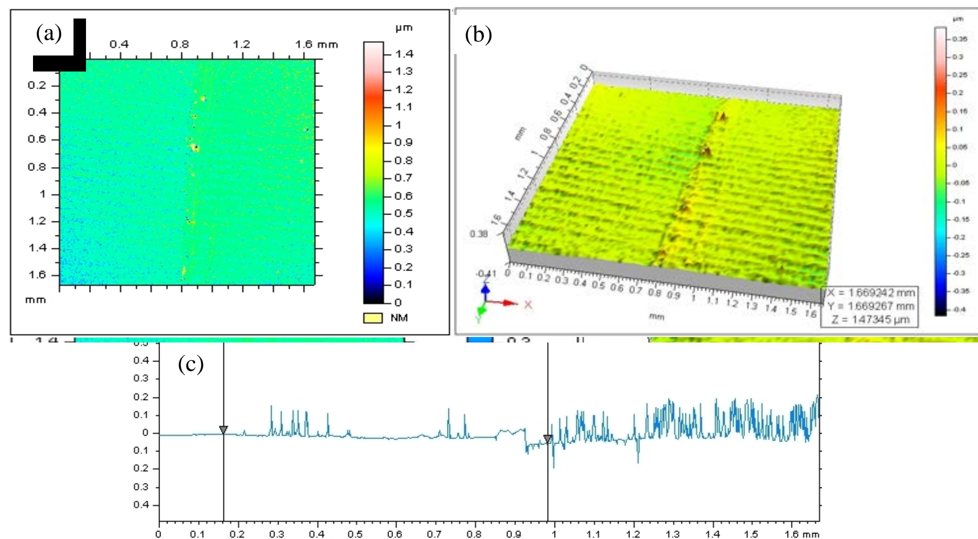

Figure 5.13 (a) 2D Optical profile, (b) 3D Optical profile and (c) line profile of CuO film sputtered at 150^{0}C and 140W using metallic target

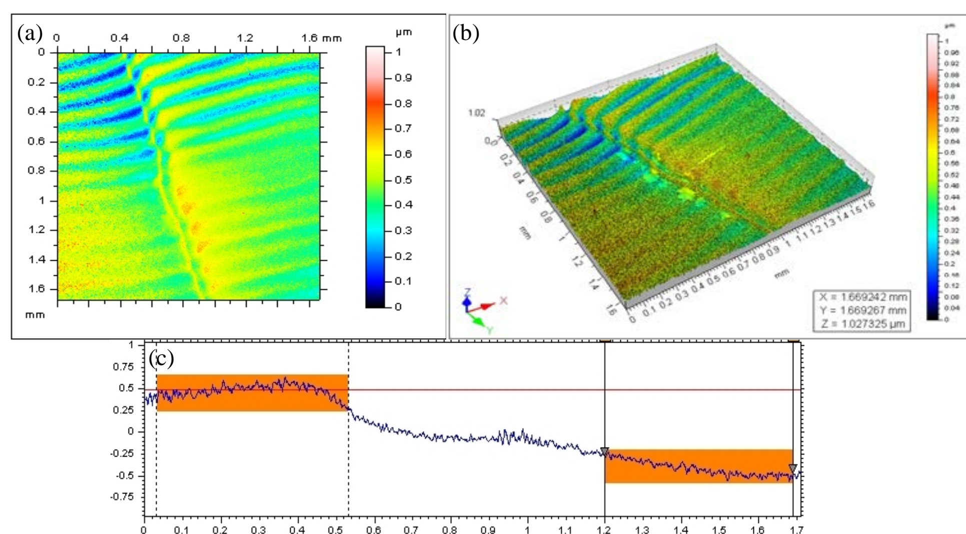

Figure 5.14 (a) 2D Optical profile, (b) 3D Optical profile and (c) line profile of CuO film sputtered at 150^{0}C and 140W using oxide target

The films formed by sputtering metallic targets were observed to be smoother compared to those from oxide targets. The results obtained were in agreement with SEM and AFM images.

5.3.7 Hall measurements

The conductivity of the sputtered thin films were analysed by Hall measurements. It is observed that the sputter power and substrate temperature during sputtering has a significant influence on the electrical properties.

Table 5.5 Variations of electrical characteristics with sputter power for the films sputtered using oxide target

Sputter power (W)	Charge carrier concentration (/cm^3)	Mobility (cm^2/Vs)	Resistivity (Ω cm)
60	1.358×10^{16}	12.89	35.66
100	3.01×10^{16}	7.662	27.07
120	2.44×10^{17}	1.511	16.93
140	3.286×10^{17}	1.318	14.41
200	9.038×10^{17}	4.68	1.48

Table 5.5 demonstrates the variations of charge carrier concentration, resistivity and mobility of CuO films with respect to sputter power (substrate temperature 150^0C). It is observed that the carrier concentration increases almost linearly with the sputter power and at 200W the film concentration reaches 9.038×10^{17}/cm^3, with a resistivity of 1.48 Ω cm while at 60W, it is only 1.358×10^{16}/cm^3 with a resistivity of 35.66 Ω cm.

As the concentration of charge carriers increase, there is a decrease in their mobility. Hence the mobility of charge carriers follows an inverse relation with sputter power as well as substrate temperature. The most important electrical property- the resistivity of thin films was found to have an inverse relation with sputter power. The possible factors that contribute to higher resistivity of films sputtered at lower powers are size effects and reduced diffusion due to lesser surface

mobility, as a result of lower energy of ad-atoms [17]. Lower surface mobility at lower sputter powers results in films with lesser crystallinity, as observed from XRD and this contributes to the increased film resistivity.

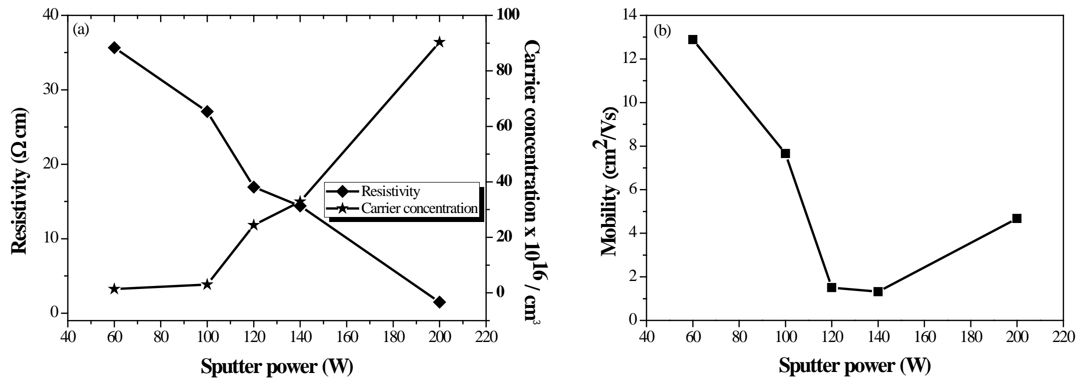

Figure 5.15 Variation of (a) carrier concentration and resistivity and (b) mobility of films sputtered using oxide target with sputter power

Figures 5.15 (a) and (b) show the carrier concentration, resistivity and mobility variations with sputter power obtained from the Hall measurements of the sputtered films. The decrease in resistivity with RF power largely results from the increase in carrier concentration. With higher RF power, sputtered target atoms with higher kinetic energy arrive at the substrate, leading to increased local bonding and consequently, these films acquire a more ordered microstructure with less defects, resulting in enhanced carrier concentration and lower resistivity.

Table 5.6 Variations of electrical characteristics with substrate temperature for the films sputtered using oxide target

Substrate temperature	Charge carrier concentration ($/cm^3$)	Mobility (cm^2/Vs)	Resistivity (Ω cm)
25^0C	$1.552x10^{16}$	32.98	42.20
100^0C	$8.90x10^{16}$	1.875	37.40
150^0C	$3.286x10^{17}$	1.318	14.41
200^0C	$3.309x10^{17}$	6.116	3.086

Table 5.6 shows the variations in charge carrier concentration, resistivity and mobility of CuO films sputtered using oxide target with substrate temperature (sputter power 140 W).

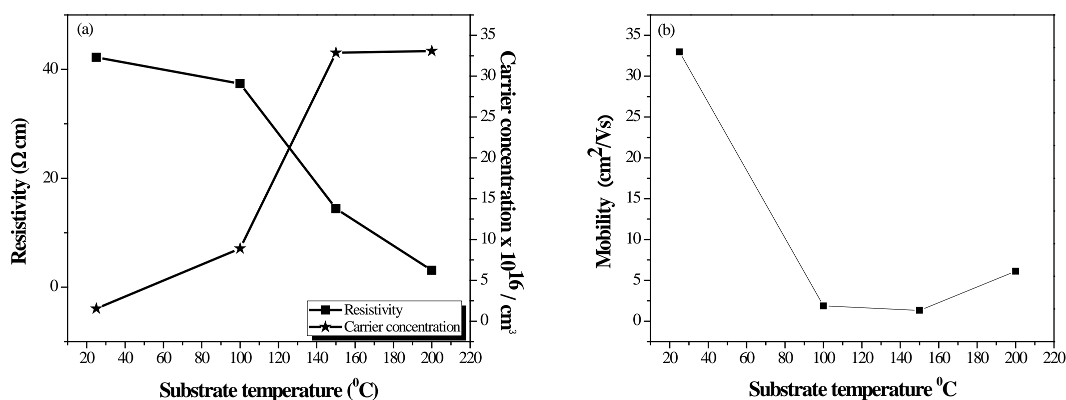

Figure 5.16 Variation of (a) carrier concentration and resistivity and (b) mobility of films sputtered using oxide target with substrate temperature

Figures 5.16 (a) and (b) show the carrier concentration, resistivity and mobility variations with substrate temperature obtained from the Hall measurements of the sputtered CuO films using oxide target.

Similar variations were observed for the films sputtered using copper metallic target. But the value of resistivity was found to be higher for these films compared to films sputtered using oxide target under similar conditions.

Table 5.7 Variations of electrical characteristics with sputter power for the films sputtered using metal target

Sputter power (W)	Charge carrier concentration ($/cm^3$)	Mobility (cm^2/Vs)	Resistivity (Ω cm)
60	1.902×10^{15}	10.008	325.6
100	4.394×10^{15}	4.522	314.2
120	1.34×10^{16}	7.56	61.6
140	1.811×10^{16}	18.08	19.06
200	2.974×10^{17}	1.662	12.63

The variations of carrier concentration and resistivity of these films with sputter power and substrate temperature have been tabulated in table 5.7 and 5.8 respectively. At highest sputter power of 200W, the resistivity was found to be 12.63

Ω cm using a metallic target. This may probably be due to the oxygen deficiencies created in the films during sputtering process.

Table 5.8 Variations of electrical characteristics with substrate temperature for the films sputtered using metal target

Substrate temperature	Charge carrier concentration (/cm^3)	Mobility (cm^2/Vs)	Resistivity (Ω cm)
25^{0}C	6.966x10^{14}	61.1	146.7
100^{0}C	7.662x10^{15}	26.1	31.21
150^{0}C	1.811x10^{16}	18.08	19.06
200^{0}C	7.11x10^{16}	2.597	13.80

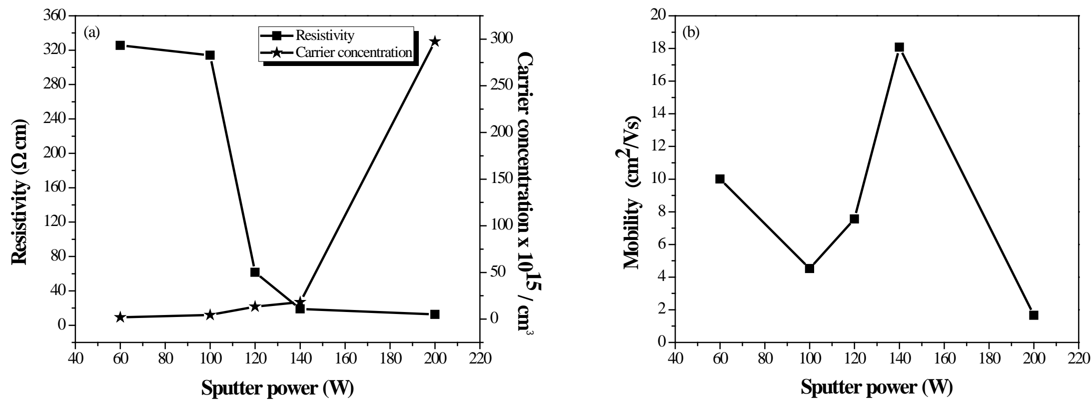

Figure 5.17 Variation of (a) carrier concentration and resistivity and (b) mobility of films sputtered using metal target with sputter power

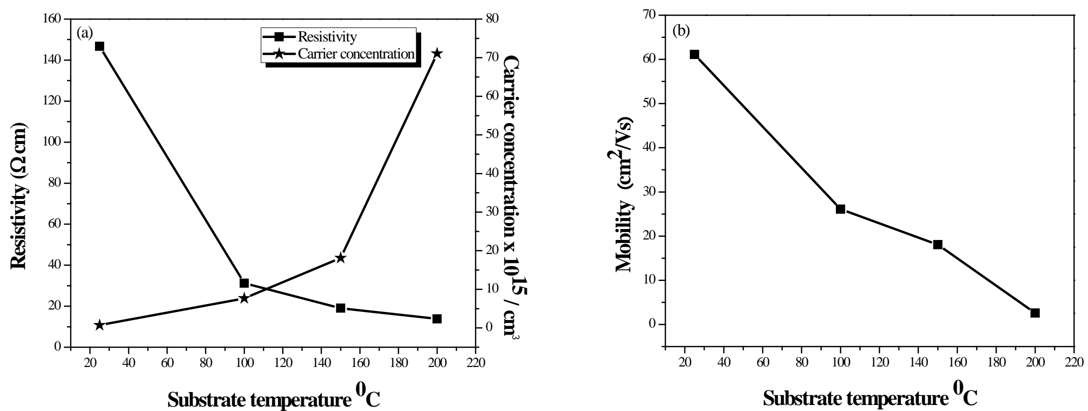

Figure 5.18 Variation of (a) carrier concentration and resistivity and (b) mobility of films sputtered using metal target with substrate temperature

The variation in carrier concentration and resistivity of CuO films sputtered using metal target with sputter power is shown in figure 5.17 (a). Figure 5.17 (b) depicts the variation in mobility with sputter power for these films. Figure 5.18 (a) and (b) illustrates the variation in charge carrier concentration, resistivity and mobility of CuO films sputtered using metal target with substrate temperature.

5.3.8 UV-Visible spectroscopy

All CuO films sputtered using oxide target exhibit an average transmittance over 70% in the visible region and a strong absorption in the UV region. The maximum average transmittance is observed for the films deposited at 60W using oxide target with transmittance above 85% and the film with maximum thickness, sputtered at 200W exhibited low transparency of ~ 65%. The absorption edge of thin films corresponds to electron transitions from valance band to conduction band.

The variations in optical transmission of the films using oxide target at substrate temperature 150^{0}C with sputter power is shown in figure 5.19 (a) and it exhibits an overall decrease, which may be caused by the increase in light scattering as the grain size increased and increase in thickness of films with sputter power. Figure 5.19 (b) shows the transmittance variation with increase in substrate temperature during deposition (at sputter power 140 W). The films deposited at 200^{0}C showed the least transmittance and films at 100^{0}C showed the maximum transparency in lower wavelengths.

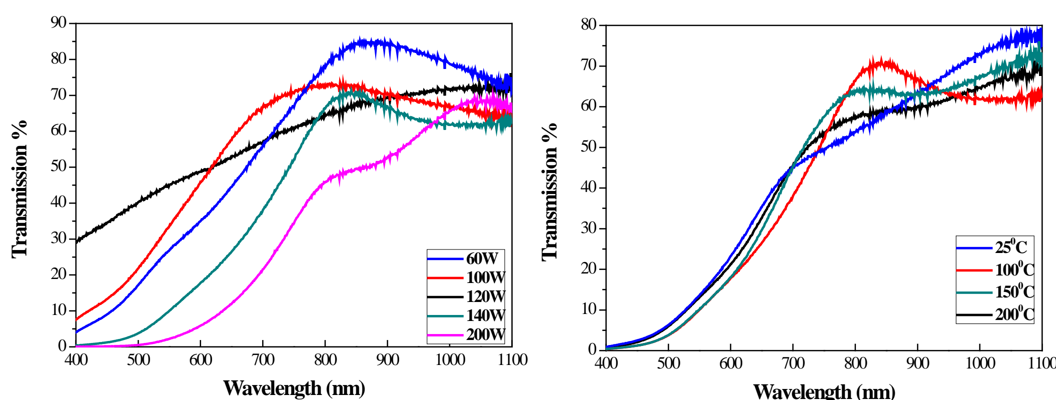

Figure 5.19 Optical transmission spectra of CuO films at different (a) sputter powers and (b) substrate temperatures using oxide target

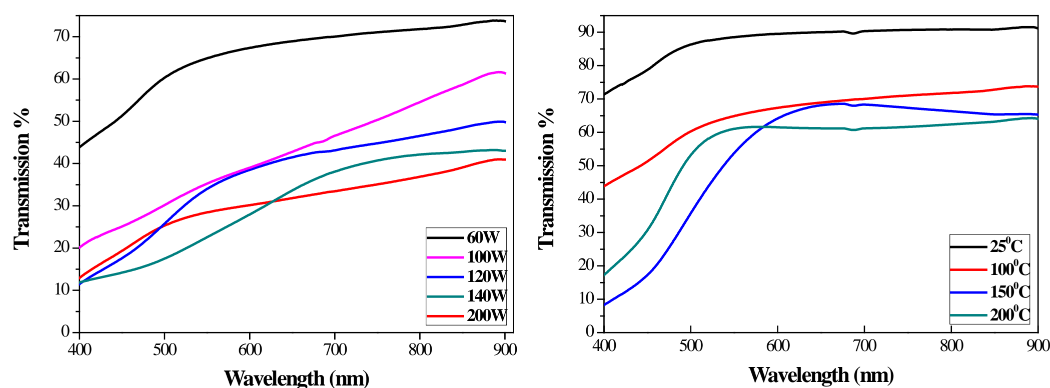

Figure 5.20 Optical transmission spectra of CuO films at different (a) sputter powers and (b) substrate temperatures using metallic target

Figure 5.20 shows the optical transmission variations with (a) sputter power and (b) substrate temperatures for the films sputtered using metallic targets under similar conditions. It also followed similar pattern to that observed in films sputtered using oxide target.

The band gap of the films was estimated from the Tauc plot (not included in this chapter), assuming parabolic band structure, as discussed in Chapter 3. It is observed that the band gap increases with RF power and substrate temperature, as tabulated in table 5.9 and 5.10. It can be seen from the Hall measurements that the carrier concentration increases correspondingly with power and temperature of substrate during deposition. The enhancement in band gap is due to the Burstein-Moss effect at high carrier concentrations.

Table 5.9 Variation in band gap with (a) sputter power and (b) substrate temperature for oxide target

(a) Sputter power (W)	Band gap (eV)
60	1.25
100	1.37
120	1.55
140	1.83
200	2.01

(b) Substrate temperature	Band gap (eV)
25^0C	1.68
100^0C	1.71
150^0C	1.83
200^0C	1.87

Table 5.10 Variation in band gap with (a) sputter power and (b) substrate temperature for metallic target

(a) Sputter power (W)	Band gap (eV)
60	1.82
100	1.86
120	1.95
140	2.06
200	2.23

(b) Substrate temperature	Band gap (eV)
25^0C	1.97
100^0C	2.04
150^0C	2.06
200^0C	2.21

The influence of band gaps on crystallization states as discussed earlier was verified by Tauc plot. Slightly enhanced band gap have been noted for films sputtered using metallic targets, as observed in table 5.10.

5.3.9 X ray Photoelectron Spectroscopy

The X-ray photo emission spectra of the CuO thin films are recorded in the same conditions described in the previous sessions. The films sputtered at 140 W and 150^0C using oxide target were chosen for the XPS studies. The surface analysis is crucial due to the unstable ionic state of copper (+1 and +2), and is significant since the electronic conduction mechanism can be revealed based on its

configurations with oxygen. The oxygen deficiency on the film surface contributes mainly to the conduction mechanism.

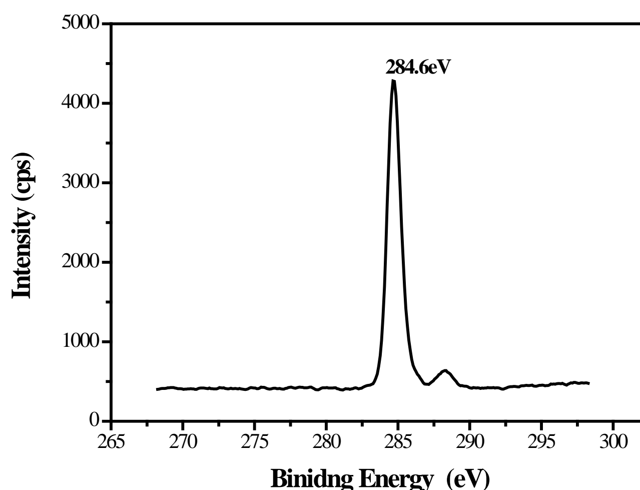

Figure 5.21 Carbon 1s spectra for XPS calibration of CuO spectra

In order to have a deep insight into this, the elemental spectra of Cu and O were recorded by narrow scanning and detailed wide spectra for tracing the presence of any other impurity contents. The spectra were calibrated by recording C*1s* core-level spectrum at 284.6 ± 0.1eV. Since the charging effect of C*1s* calibration is standardized at 284.5eV in this report, the spectra of all elements will appear apparently at an energy difference of -0.10eV. Figure 5.21 shows the calibrated spectra of C1s.

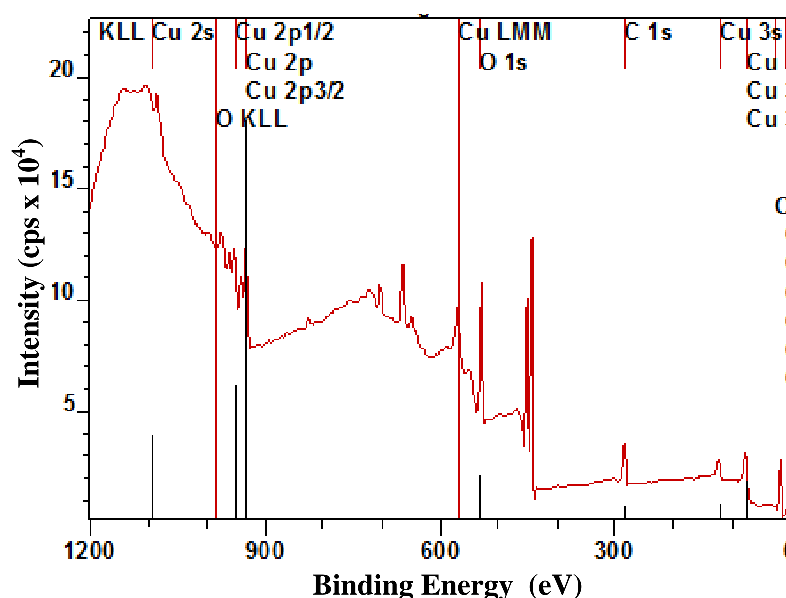

Figure 5.22 Survey scan spectrum of CuO films

Figure 5.22 indicates the detailed surface scan of the film. The spectrum is composed of intense peaks of elements copper and oxygen only. But trace of carbon was detected, but not predominant enough to exhibit any remarkable properties.

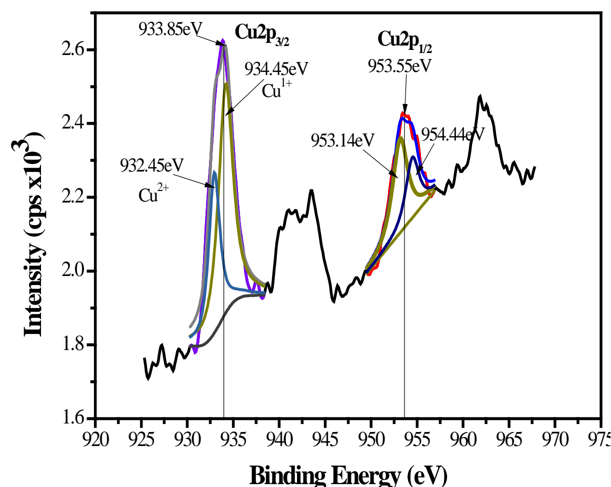

Figure 5.23 Narrow scan analysis of copper in sputtered CuO films

The Cu *2p* spectra in figure 5.23 appear complicated due to the shape of peaks and shake-ups in satellite peaks. Cu *2p* components were split into two Gaussian shapes indicative of multiple oxidation state. The spectra constitutes doublet lines centred at 933.85 eV and 953.55eV corresponding to Cu $2p_{3/2}$ and Cu $2p_{1/2}$, along with well-defined shake-up broad satellite lines observed between 6 and 10 eV distance apart from the asymmetric Cu $2p_{3/2}$ line. The peak at 933.85eV assigned as Cu $2p_{3/2}$ emission, constitutes multiple components because of its multiple ionic state with oxygen. Hence, the Cu $2p_{3/2}$ spectra is fitted into two components and as indicated, the spectral line with high core level intensity at 934.45eV is due to Cu (+1) state.

The XPS peak of Cu $2p_{1/2}$ core level is also deconvoluted into two binding energy curves at 953.14 eV and 954.44 eV, confirming the presence of CuO and Cu_2O states respectively. The presence of Cu in its dual state could certainly affect the conduction mechanism in transparent conducting thin films; the materials are likely to exhibit *p*-type conduction. This XPS spectrum is consistent with previous reports on copper oxide [18].

The major peaks are accompanied by strong shake up satellite peak present between 940 eV – 945 eV. This is regarded as a characteristic feature of the Cu (II) state. The low intensity spectral line at 932.45eV is due to the Cu (+2) on the surface. O *1s* peaks in figure 5.24; provide complementary information on different components. The spectrum constitutes three different spectral components at 529.62eV, 531.13eV and 531.87eV.

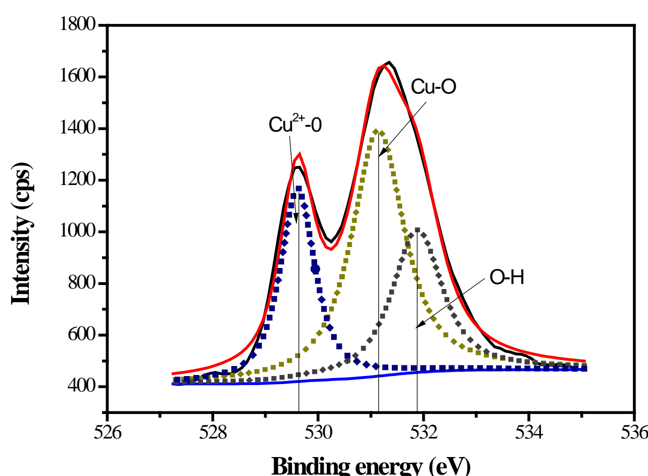

Figure 5.24 Narrow scan analysis of oxygen in sputtered CuO films

O *1s* spectra typically appear complex in shape due to its various ionic states and hydroxyls present on film surface. Figure 5.24 shows the O *1s* spectra of CuO thin films, fitted with multiple components showing Gaussian shapes related to Cu^{2+}-O binding, Cu^{1+}-O binding and hydroxyl species. The components are illustrated in figure, Cu^{2+}- O bonding appears first and large area is attributed for Cu^{1+}- O state, as expected there are O-H groups on the surface (indicated at 531.87 eV). The presence of relatively large amount of Cu^{1+} ions on the surface of thin films will enhance the *p*-type electrical conduction in thin films. The results of electrical studies authenticate these results [19].

5.3.10 Optical transparency of the film

Figure 5.25 shows the actual photograph of the sputtered CuO thin film at 150^0C and 140 W sputter power, showing the transparency of the films in normal

day light. It can be observed that sputtered films using both targets exhibit almost the same transparency.

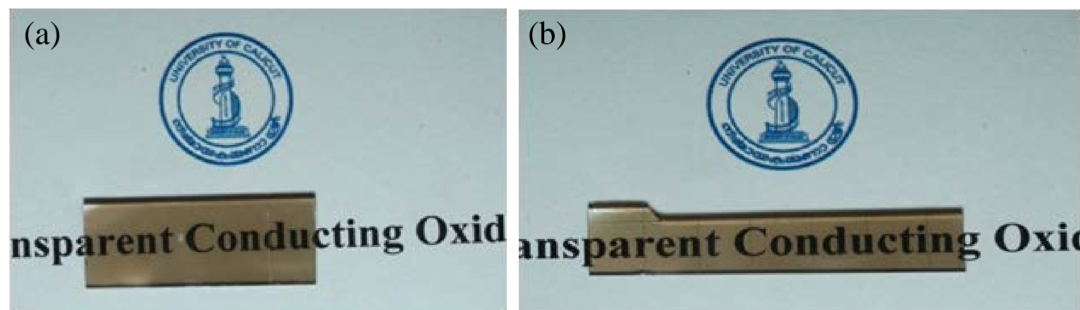

Figure 5.25 Actual photographs of CuO films sputtered at 150^{0}C and 140W using (a) oxide target and (b) metal target

5.4 Copper Indium oxide (CIO)

Copper oxides have been investigated by researchers as semiconducting materials for photovoltaic applications owing to their unique optical and electrical properties. But the complexity in regulating its electrical properties is the main limitation for use in realistic functions. By introducing cations at crystallographically identical sites of transition metal oxides, high conductivity can be achieved [20]. The substitution of Cu in CuO with lithium, forming defect structures and oxygen deficiencies and their influence on the transport properties have been studied [21, 22]. However, the effect of incorporating a group III element in CuO lattice needs to be studied in detail and in this work; we have chosen indium to be incorporated in CuO.

5.4.1 Electronic structure and transparent conducting properties

The complex relation between the electrical and optical properties and structure of a material should be known for increasing its conductivity and transparency. Copper based delaffosite structures are well known for their *p*-type conductivity [23]. Indium incorporated copper exhibits bi-polar dopability, i.e., it can be doped to achieve both *n* and *p*-type conductivity. The reason was explained as due to the low conduction band minimum and high valence band maximum in $CuInO_2$ [24]. Cu-In-O system can exist in two phases- $Cu_2In_2O_5$ [25] and $CuInO_2$.

Reaction enthalpy calculations of Cu_2O, In_2O_3 and $CuInO_2$, yield that the formation energy of $CuInO_2$ is 0.056 eV, much higher than Cu_2O and In_2O_3 [26]. Hence it is difficult to synthesise phase pure $CuInO_2$ by solid state reactions; it is likely to find residual Cu_2O and In_2O_3 in the compound. The enhancement of *p*-type conductivity by the incorporation of a III group element is unexpected, since it should result in reduction of net concentration of holes and hence a reduction in conductivity.

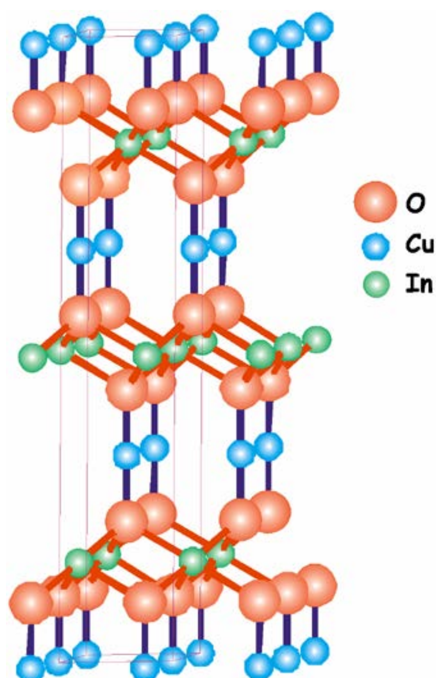

Figure 5.26 Crystal structure of Copper Indium Oxide

Figure 5.26 gives the delaffosite crystal structure of Cu-In-O system. Copper and indium are two significant elements having stable cations with (n-1) d_{10} n s_0 configuration in the periodic table. Materials with the delaffosite structure AMO_2 (where A is a mono valent ion, such as Cu^+ and Ag^+ and M is a trivalent ion, such as Al^{3+}, Ga^{3+}, In^{3+}, Cr^{3+}, Fe^{3+}, Co^{3+} etc.) have been investigated earlier as *p*-type conducting transparent conductors. The structure involves stacking of O–A–O dumbbell layer and a layer of edge sharing MO_6 octahedra alternately. The oxide ions form a "pseudo tetrahedral" arrangement as M_3-A-O, causing a decrease in the non-bonding nature of oxide ions and hole delocalisation at the valence band edge [27]. The layered structure involving the AO_2 dumbbell significantly cuts down the level of cross-linking of A-ions resulting in the rise of band gap [28].

5.5 Results and discussion

Transparent *p*-type conducting copper indium oxide (here after referred as CIO) thin films were deposited on quartz substrates using commercially available $CuInO_2$ metallic target (99.99% pure) with 3mm thickness and 4.8cm diameter. Detailed optical, electrical and morphological studies were conducted, as detailed below. The variations in their properties due to sputter power and substrate temperature are also explored and discussed.

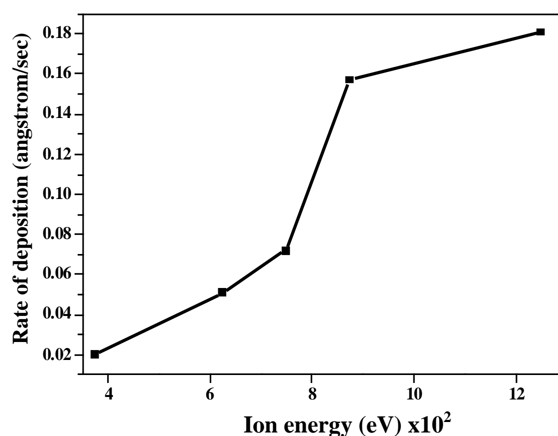

Figure 5.27 Yield of sputtering of CIO thin films

The films were fabricated by radio frequency magnetron sputtering and the yield obtained as a ratio of rate of deposition and the energy of ions is given in figure 5.27. It can be observed that as the ion energy increases, there is a sharp increase in the rate of deposition of the films. Table 5.11 gives the experimental parameter details used for sputtering process.

Table 5.11 Experimental parameter details used for sputtering process

Target	CIO target
Substrate	Quartz
Target–substrate distance	60 mm
Deposition (Ar) pressure	$4x10^{-2}$ m bar
Base pressure	$1x10^{-6}$ m bar
Deposition time	30 minutes
RF power (W)	60-200 W
Substrate temperature	25^0C - 200^0C

5.5.1 X-ray Diffraction

The indexed XRD spectra of the sputtered *p*-CIO thin films at various sputter powers and substrate temperature 100^0C are shown in figure 5.28 (a).

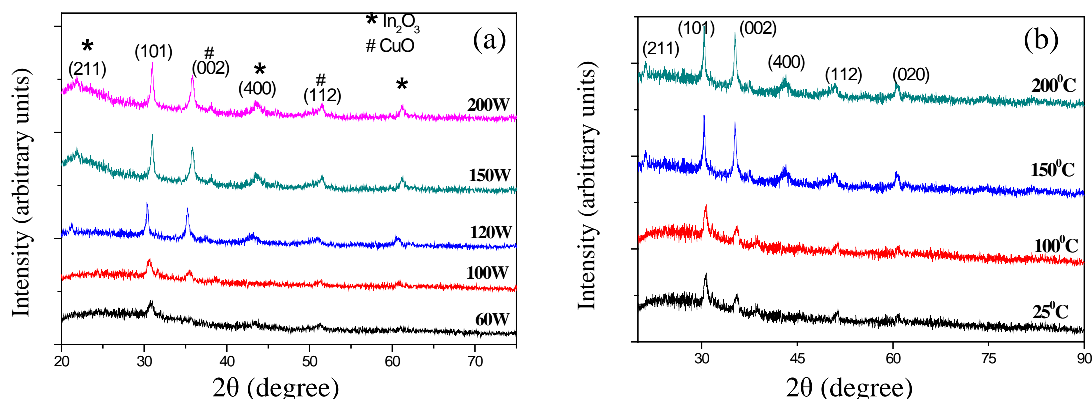

Figure 5.28 XRD pattern of CIO films with varying (a) sputter power and (b) substrate temperature

Sputtering at 60W resulted in less crystalline films, as can be seen from the XRD patterns. The intensity in peaks and therefore the crystallinity is found to increase with sputter power. The delaffosite structure characterized by 101 plane becomes more prominent at higher sputter powers. Also, the peaks at 2Θ values 21.28^0, $35.24\ ^0$ and 43.07^0 (marked by * in the figure) were not observed in the films sputtered at low power. At 200W, all the major peaks can be observed due to enhanced crystallinity. The film can be considered to be in a mixed phase of tenorite structured CuO and In_2O_3 and delaffosite $CuInO_2$. It is obvious that sputter power has a significant influence on the crystalline nature of the films. This can be attributed to the enhanced surface mobility of adsorbed target atoms (ad-atoms) with increase in sputter power. The energy of inert Ar ions from sputter gas increases, thereby providing more kinetic energy to the ad-atoms. These ad-atoms diffuse from the surface of the target towards the substrate, thus forming highly crystalline films. The rise in Ar ion energy also results in enhanced rate of deposition. Figure 5.28 (b) shows the XRD pattern of films sputtered at 150W and various substrate temperatures.

5.5.2 Scanning Electron Microscopy

SEM images of the sputtered CIO films at 100^0C show the uniform and homogeneous distribution (figure 5.29) at higher powers, similar to CuO films. The

increase in sputter power results in considerable variation in the packing and arrangement of particle on the surface of substrates. Variation of surface morphology with substrate temperature at constant sputter power of 150W is shown in figure 5.30.

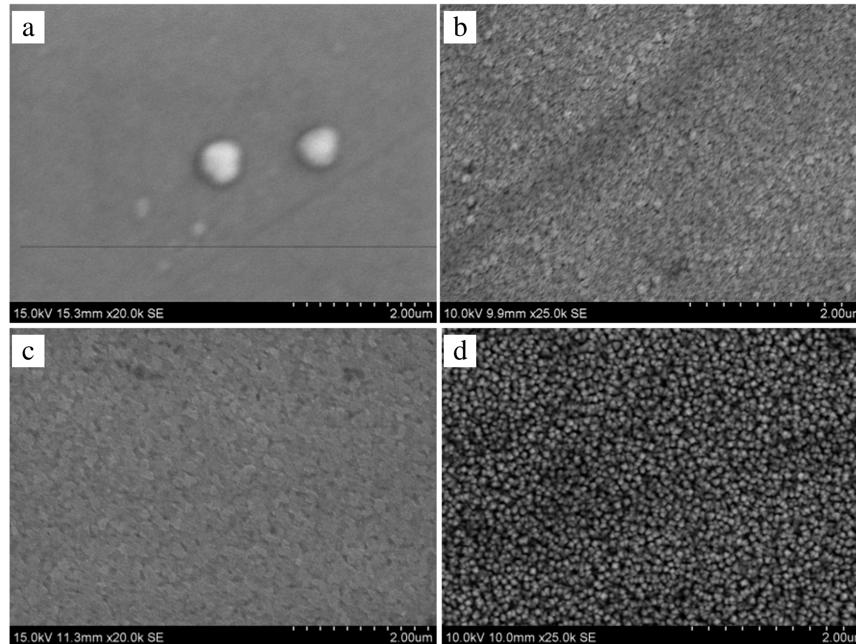

Figure 5.29 SEM images of CIO films sputtered at powers (a) 60 W, (b) 100 W, (c) 150 W and (d) 200 W

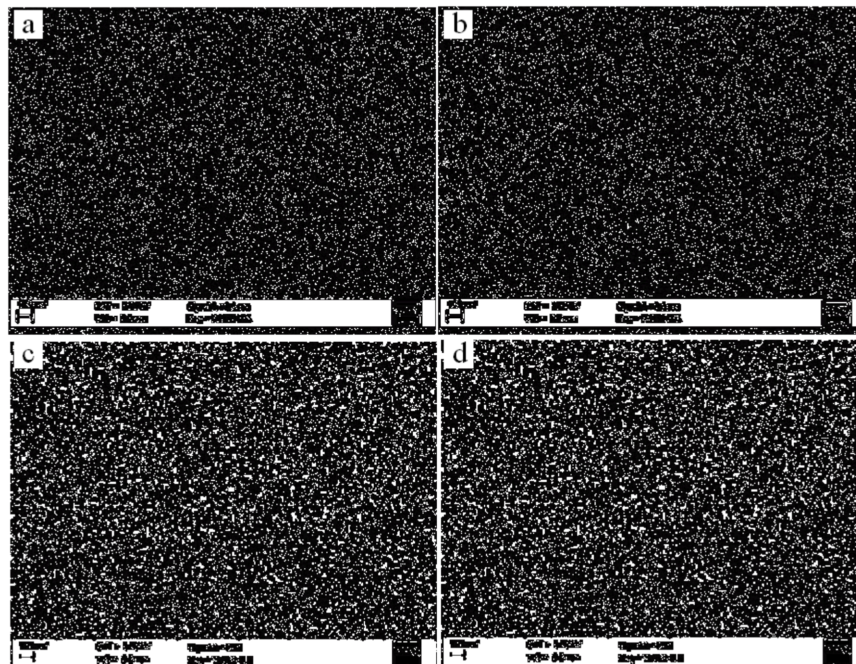

Figure 5.30 SEM images of CIO films sputtered at substrate temperatures (a) 25^{0}C, (b) 100^{0}C, (c) 150^{0}C and (d) 200^{0}C

5.5.3 Atomic Force Microscopy

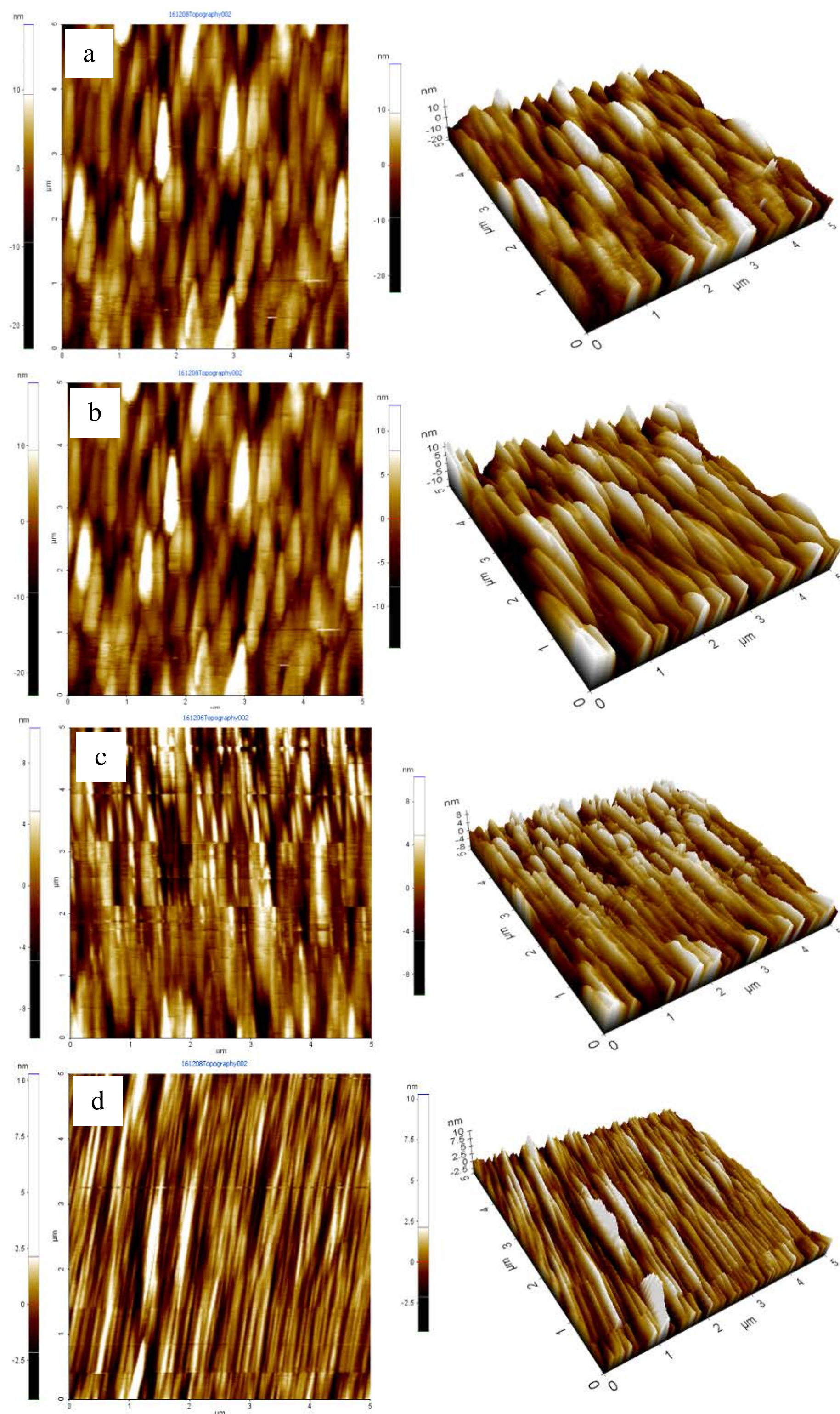

Figure 5.31 2D and 3D AFM images of CIO films at powers (a) 60W, (b) 100W, (c) 150W and (d) 200W

Figure 5.31 shows the atomic force micrographs of the samples. The degree of homogeneity and density of packing are seen to increase with sputter power, due to reasons discussed earlier. The substrate temperature was maintained constant at 100^{0}C. The RMS surface roughness of the films showed an increasing tendency with sputter power. The results obtained are tabulated in table 5.12 and it is found to be higher than that of CuO films.

Table 5.12 RMS roughness variations of CIO films with sputter power

Sputter power (W)	RMS (nm)
60	2.635
100	3.099
150	3.601
200	4.044

5.5.4 Optical Profilometry

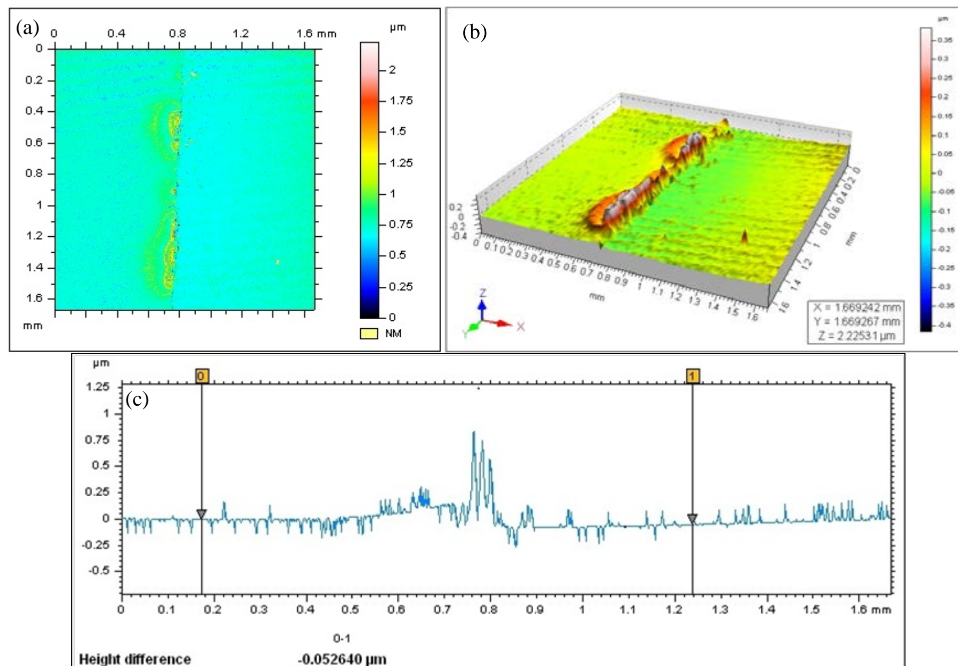

Figure 5.32 (a) 2D Optical profile, (b) 3D Optical profile and (c) line profile of the CIO film

The smoothness and uniform distribution of the coating can be observed in the optical profile of CIO thin films shown in figure 5.32. Thickness of the film sputtered at 100^0C and 150 W was found to be 52.64 nm from the line profile of the films. The results obtained were in agreement with the observed results of SEM and AFM.

5.5.5 Hall measurements

Hall measurements on the *p*-type CIO films revealed the carrier concentration, conductivity and mobility of charge carriers as shown in table 5.13.

Table 5.13 Variation of electrical properties with (a) sputter power and (b) substrate temperature

(a)

Sputter power (W)	Charge carrier concentration (/cm^3)	Mobility (cm^2/Vs)	Resistivity (Ω cm)
60	2.825×10^{17}	5.883	3.755
100	3.882×10^{19}	2.602	6.181×10^{-2}
150	1.225×10^{21}	5.819×10^{-2}	8.76×10^{-2}
200	1.332×10^{21}	0.3218	1.457×10^{-2}

(b)

Substrate temperature	Charge carrier concentration (/cm^3)	Mobility (cm^2/Vs)	Resistivity (Ω cm)
25^0C	7.088×10^{18}	0.2331	3.778
100^0C	1.225×10^{21}	5.819×10^{-2}	8.76×10^{-2}
150^0C	7.65×10^{21}	2.429	3.359×10^{-2}
200^0C	6.206×10^{23}	2.139×10^{-2}	4.703×10^{-3}

The main challenge in getting adequate conductivity in *p*-type TCOs is the reduction of localization behaviour of positive holes at the valence band edge of oxide materials. A hole introduced in the lattice localizes on a single oxygen atom, which becomes immobile within the crystal lattice, even under the application of external electric field, since the 2*p* energy levels of oxygen atoms are low compared to valence orbitals of metal atoms [27]. The possible solution to this phenomenon is

to make the uppermost closed shell energy level of metallic cation equivalent to 2*p* energy level of oxide ions. The closed shell energy level of Cu^{2+} ions is almost similar to that of 2*p* oxides and hence the superior conductivity of sputtered CuO and CIO films we obtained may be attributed to this phenomenon [28].

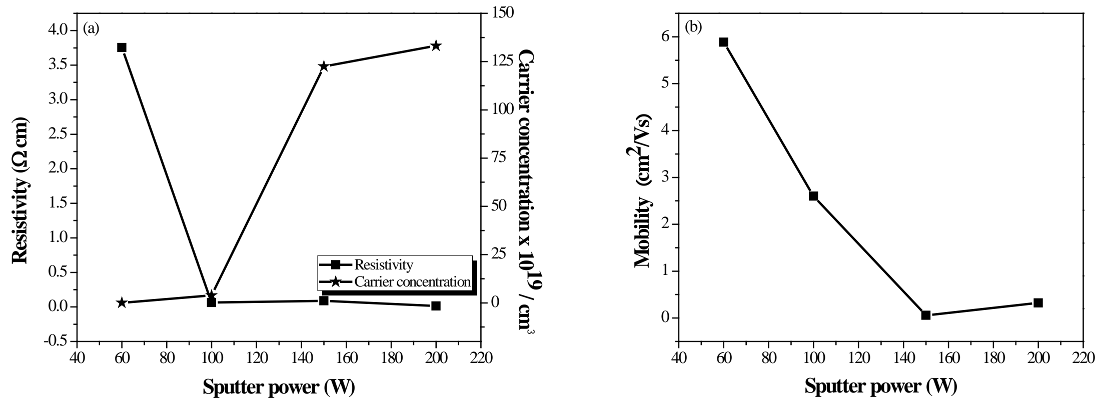

Figure 5.33 Variation of (a) carrier concentration and resistivity and (b) mobility of films with sputter power

Hall measurements confirmed the *p*-type conductivity of CIO films and showed the decrease in resistivity from 3.755 Ω cm to 1.457 × 10^{-2} Ω cm with increase in sputter power 60 W to 200 W during sputtering. Also the carrier concentration was found to be much higher than that obtained for CuO. Hence, the incorporation of In^{3+} has a significant influence on electrical properties of the films. Figure 5.33 (a) depicts the influence of sputter power variation on charge carrier concentration and resistivity for CIO films. Mobility variation with sputter power for the CIO films is depicted in figure 5.33 (b).

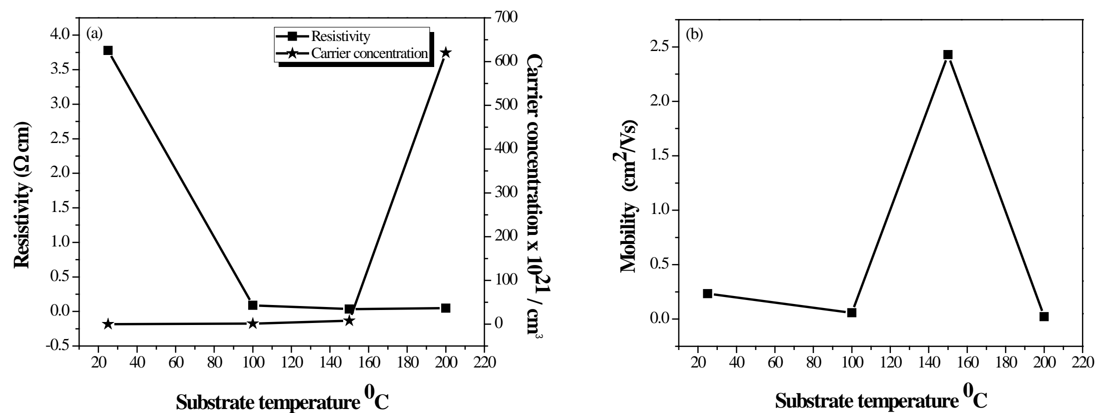

Figure 5.34 Variation of (a) carrier concentration and resistivity and (b) mobility of films with substrate temperature

Figure 5.34 (a) and (b) illustrates dependence of carrier concentration, resistivity and mobility of sputtered CIO films on substrate temperature.

5.5.6 UV-Visible Spectroscopy

The optical transmission spectrum shows a reasonably high transmission of visible light through the films. In the case of copper (II) oxide, the *d-d* transitions in Cu^{2+} ions obstruct optical transmittance in the visible range. But in In_2O_3 a transmission of >90% in visible range is usually observed [29]. Hence the CIO films showed a reasonably high transmission. Figure 5.35 (a) shows the optical transmission spectra of CIO films with varying sputter powers at a constant substrate temperature of 100^0C and the transmission was found to decrease with increase in film thickness. Films sputtered at 60 W and 100 W showed high transmission. As the transmission spectrum does not possess enough fringes it was not able to calculate thickness of films using Swanepoel's method. In figure 5.35 (b) the optical spectra with varying substrate temperatures (at constant power 150W) is shown, and the visible light transmission was found to decrease with temperature. Optical band gap of the films were determined using Tauc plot (not included here) and the band gap energies are tabulated in table 5.14.

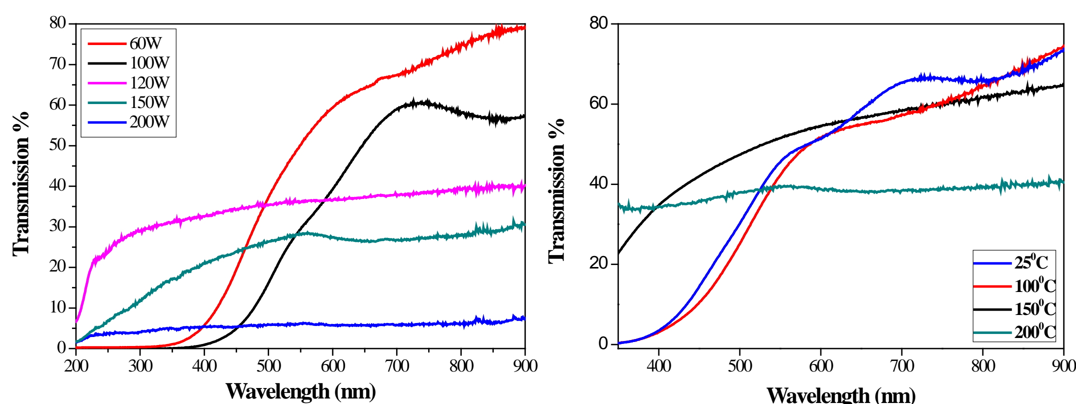

Figure 5.35 Optical transmission spectra of CIO films at different (a) sputter powers and (b) substrate temperatures

Table 5.14 Variation in band gap with (a) sputter power and (b) substrate temperature

(a) Sputter power (W)	Band gap (eV)
60	1.358
100	1.491
150	1.534
200	1.820

(b) Substrate temperature	Band gap (eV)
25^0C	1.412
100^0C	1.534
150^0C	1.791
200^0C	1.935

The sharp decrease in transmittance observed around 400 nm is due to the absorption edge. The UV-Visible transmission spectra of the films revealed good transparency in the visible range but less than that for the CuO films. The optical band gap thus calculated were found to be 1.358 eV, 1.491 eV, 1.534 eV and 1.82 eV for the films deposited at 60 W, 100 W, 150 W and 200 W respectively. The band gap was found to be larger than that of CuO, but less than the band gap of In_2O_3 [30, 31]. Also, since CuO and In_2O_3 have indirect band gaps, similar band gap is expected for the CIO system. As the RF power during growth is increased from 60W to 200W, band gap is found to be increased, which may be probably due to the positioning of atoms in more favourable or stable positions due to the increased RF power during sputtering, which in turn leads to better adhesion of the films.

5.5.7 X-ray Photoelectron Spectroscopy

The elemental scanning of the surface provide emissions from the Cu *2p*, In *3d* and O *1s* regions. The Cu *2p* spectra in figure 5.36 shows significant spectral asymmetry and shake ups indicating valance instability of copper on the film surface. It is composed of Cu $2p3_{/2}$ and Cu $2p_{1/2}$ components due to spin orbit coupling of 2*p* electrons. Two electronic charge contributions of copper with oxygen

from CuO (934.27 eV) and Cu_2O (932.25 eV) are observed, which confirms that they are composed of copper with multiple electronic states.

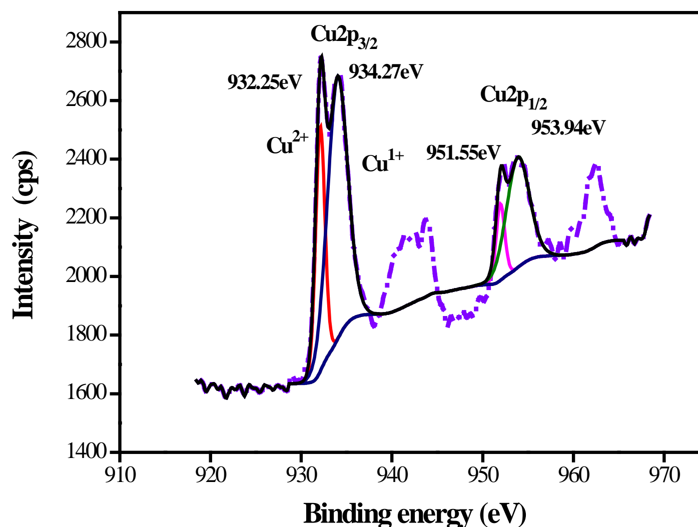

Figure 5.36 Narrow scan analysis of copper in sputtered CIO films

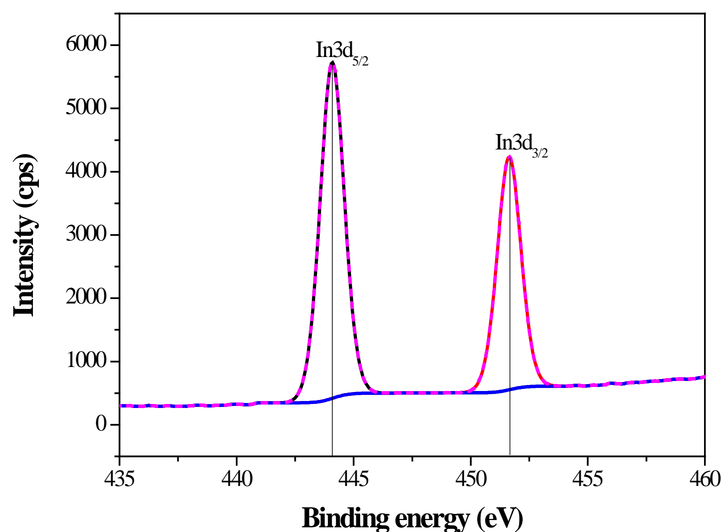

Figure 5.37 Narrow scan analysis of indium in sputtered CIO films

The narrow scan spectra of indium revealed that In 3*d* peak is composed of two symmetrical peaks (figure 5.37) that are assigned as In $3d_{3/2}$ and In $3d_{5/2}$ respectively at binding energy positions In $3d_{3/2}$ 451.67±1eV and In $3d_{5/2}$ at 444.09±1eV. This suggests that indium in the samples are in its most stable +3 oxidation state. The O *1s* peak in figure 5.38 is deconvoluted into two components related to the oxidation state of the cations on the film surface. Instead of showing

three components from the Cu^{1+}, Cu^{2+} and In^{3+} regions, the spectra shows only two curves when it is fitted. The absences of hydroxides are also noticed. This may be due to the overlapping of binding energy positions. The survey scan spectra of the sample sputtered at 100^{0}C and power 150W is shown in figure 5.39.

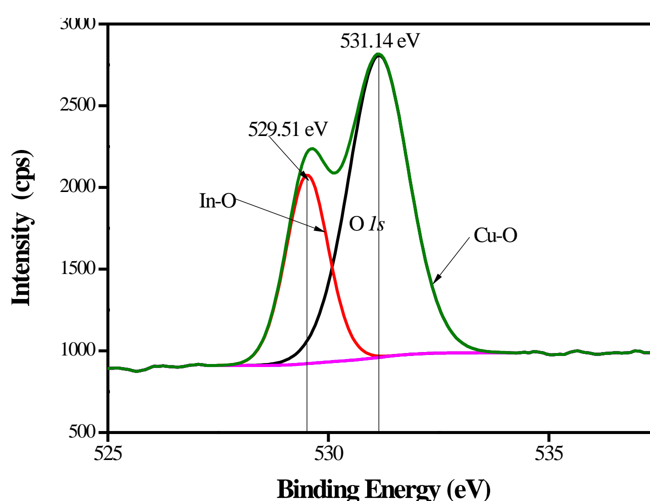

Figure 5.38 Narrow scan analysis of oxygen in sputtered CIO films

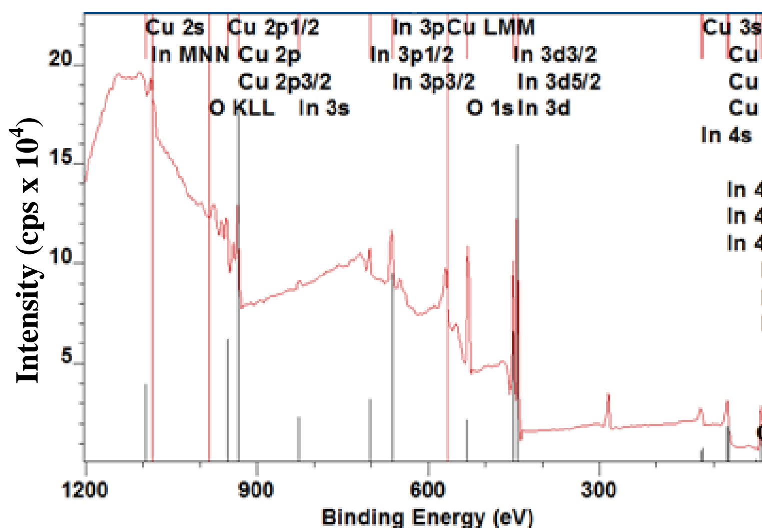

Figure 5.39 Survey scan spectrum of CIO films

5.5.8 Optical transparency of the film

The quantitative average transmittance of the films sputtered at 100^{0}C and 150W can be observed from figure 5.40. It was found to be less transparent compared to CuO films, as confirmed in the UV-Visible spectra.

Figure 5.40 Actual photograph of CIO films

5.6 Conclusions

- Highly uniform and crack free *p*-type conducting thin films of copper (II) oxide and copper indium oxide were fabricated on quartz substrate via radio frequency magnetron sputtering.
- The effects of sputter power and substrate temperature during the process on the fabricated thin films were investigated.
- The detailed structural studies were conducted by X ray diffraction analysis and X ray photoelectron spectroscopy.
- Compositional analysis was done using energy dispersive spectroscopy and surface features were studied by optical profilometer.
- Electrical characteristics were investigated by Hall measurements and morphological studies by atomic force microscopy and scanning electron microscopy.
- The resistivity of CIO films was found to be less, along with a higher carrier concentration, compared to copper oxide films. But, optical studies reveal lower transparency in the visible range for the CIO films, compared to CuO films.
- Taking all aspects of a good TCO into consideration, both CuO and CIO films were used for further studies and realisation of practical transparent electronic circuits.

References

[1] John F. Wager, Douglas A. Keszler and Rick E. Presley, Transparent Electronics (2007) Springer.

[2] Nasrin Sarmadian, Rolando Saniz, Bart Partoens and Dirk Lamoen, Scientific Reports, 6 (2016) 20446.

[3] Hiroshi Kawazoe, Masahiro Yasukawa, Hiroyuki Hyodo, Masaaki Kurita, Hiroshi Yanagi and Hideo Hosono, Nature, 389 (1997) 939.

[4] K. K. Chattopadhyay and A. N. Banerjee, Introduction to Nanoscience and Nanotechnology (2009) Prentice Hall, India.

[5] H. Sato, T. Minami, S. Takata and T. Yamada, Thin Solid Films, 236 (1993) 27.

[6] D. S. Ginley, Handbook of Transparent Condutors (2010) Springer Science.

[7] Chetoui Abdelmounaim, Zouaoui Amara, Ayat Maha and Djebbouri Mustapha, Materials Science in Semiconductor Processing, 43 (2016) 214.

[8] Oral, A.Y., Menşur, E., Aslan, M. H. and Başaran, E., Materials Chemistry and Physics, 83 (2004) 140.

[9] Pierson J.F., Thobor-Keck A. and Billard A, Applied Surface Science, 210 (2003) 359.

[10] Ray S.C., Solar Energy Materials and Solar Cells, 68 (2001) 307.

[11] Serin N., Serin T., Horzum S. and Celik Y., Semiconductor Science and Technology, 20 (2005) 398.

[12] Serin T., Yildiz A., Horzum Sahin S. and Serin N., Physica B: Condensed Matter, 406 (2011) 575.

[13] Shanid N. A. M. and Khadar M. A., Thin Solid Films, 516 (2008) 6245.

[14] Wu D., Zhang Q. and Tao M., Physical Review B, 73 (2006) 235206.

[15] P. Samarasekara, N. T. R. N. Kumara and N. U. S. Yapa, Journal of Physics: Condensed Matter, 18 (2006) 8.

[16] C. L. Azanza Ricardo, M. D'Incau, M. Leoni, C. Malerba, A. Mittiga, P. Scardi, Thin Solid Films, 520 (2011) 280.

[17] Cristina Besleaga, L. Ion and S. Antohe, Romanian Reports in Physics, 66 (2014) 993.

[18] S. Paulston, P. M. Parlett, P. Stone and M. Bowker, Surface and Interface Analysis, 24 (1996) 811.

[19] Balamurugan B. and Mehta B. R., Thin Solid Films, 396 (2001) 90.

[20] E. J. W. Verwey, P. W. Haaijman, F. C. Romeijin, and G. W. Oosterhout, Philips Research Reports, 5 (1950) 1734.

[21] Prakash Chand, Anurag Gaur and Umesh Kumar Gaur, Applied Surface Science, 307 (2014) 480.

[22] K. Suba, O. G. Singh, B. D. Padalia, Om Prakash, and D. Chandrasekharam, Materials Research Bulletin, 29 (1994) 443.

[23] Alan V. Chadwick, Aran N. Blacklocks, Aline Rougier and Cedric Yaicle, Journal of Physics: Conference Series, 249 (2010) 012045.

[24] Hiroshi Yanagi, Tomomi Hase, Shuntaro Ibuki, Kazushige Ueda and Hideo Hosono, Applied Physics Letters, 78 (2001) 1583.

[25] Chia-Ying Su, Chiu-Yen Chiu, Chih-Hui Chang and Jyh-Ming Ting, Thin Solid Films, 531 (2013) 42.

[26] Li Liu, "Towards a better understanding of the electrical properties of CuInO2, a delafossite TCO", Master's thesis, National University of Singapore, 2004.

[27] C. Yaicle, A. N. Blacklocks, A. V. Chadwick, J. Perriere and A. Rougier, Applied Surface Science, 254 (2007) 1343.

[28] Minami T., Kakumu T., Shimokawa K. and Takata S., Thin Solid Films, 317 (1998) 318.

[29] H. L. Hartnagel, A. L. Dawar, A. K Jain, and C. Jagadish, Semiconducting Transparent Thin Films, Institute of Physics (1995) Bristol and Philadelphia.

[30] J. Ghijsen, L. H. Tjeng, J. van Elp, H. Eskes, J. Westerink, G. A. Sawatzky and M.T. Czyzyk, Physical Review B, 38 (1988) 11322.

[31] F. Marabelli, G. B. Parravicini and F. Salghetti-Drioli, Physical Review B, 52 (1995) 1433.

CHAPTER 6

FABRICATION OF THIN FILM HETEROJUNCTIONS

6.1 Introduction

Recent researches in the field of semiconductors have led to the development of several devices making use of *p–n* junctions and Schottky junction diodes. These are fabricated using wide-gap semiconductors such as GaN, ZnSe, ZnS and diamond systems, for applications such as UV detectors and photovoltaic cells [1]. Transparent oxide conductors are more preferable as UV-detectors, since they are optically transparent in the visible range, environment friendly, non-toxic and thermally and chemically stable. *p–n* junction diodes made of silicon with a band gap of 1.1 eV are currently in wide use for such applications, but since the band gap of TCOs are greater than that of visible light, i.e., 3.1 eV, junctions based on these materials are potential candidates for such applications.

Transparent *p-n* hetero junction diode was first fabricated by Kudo et al. in 1999, which comprised of polycrystalline *p*-type $SrCu_2O_2$ and *n*-type ZnO, deposited on a glass substrate using pulsed laser deposition technique [2]. The junction exhibited nonlinear and rectifying *I–V* characteristics and a small leakage current observed in reverse bias. The forward to reverse current ratio was larger than 80 in the voltage range -1.5 to +1.5 V.

In 2001, *Hoffman* et al. reported *p–n* hetero junction diodes with *p*-type $CuYO_2$:Ca and *n*-type ZnO [3]. The interface between *p*-type and *n*-type semiconductors is significant, since crystallographic imperfections at the interface produce leakage currents, which will affect the current rectification behaviour of the diode. Amorphous *p–n* junction diodes with *p*-type ZnO-Rh_2O_3 and *n*-type In-Ga-ZnO layers was reported by Narushima et al. in 2003 [4]. Since the interface between layers was atomically flat, the *p-n* hetero junction diode exhibited good *I–V* characteristics. Transparent films of ZnO/NiO/ITO were grown onto a (111) YSZ substrate by PLD combined with solid-phase epitaxy (SPE) by Ohta et al. [5]. Rectifying *I–V* characteristics with a forward threshold voltage of 1 V and ideality factor of ~2 was observed.

In this work, we have fabricated transparent *p-n* hetero junctions using *p*-type materials copper oxide and copper indium oxide and *n*-type ITO. Thin films of these materials were deposited using radio frequency magnetron sputtering onto different substrates. After several trials, we optimised the deposition conditions and thermodynamic parameters of fabrication to control the charge carrier concentration and mobility of the sputtered thin films, so as to obtain good *I-V* characteristics for the hetero junctions formed.

6.2 Growth of *p-n* junctions by RFM sputtering

In normal semiconductors, when *n* and *p*-type are joined together to form a junction, interaction takes place at the junction between positive holes in one semiconductor and free electrons in the other. Free electrons in the *n*-type material diffuse the junction transversely and recombine with holes in the *p*-type material. Similarly, a few holes in the *p*-type material diffuse and recombine with electrons in the *n*-type semiconductor. This transfer of charge carriers leads to a space-charge region (depletion layer) at thermal equilibrium.

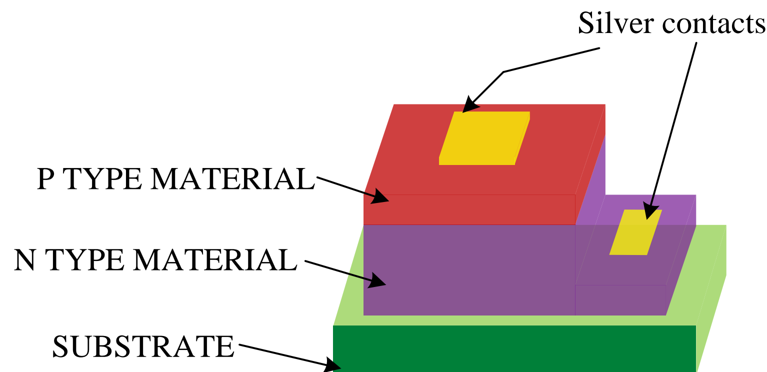

Figure 6.1 Schematic diagram of the transparent p-n hetero junction

A *p–n* hetero junction diode generally exhibits asymmetric current–voltage (*I–V*) characteristics. The current-voltage measurement of a normal silicon diode is performed in dark, whereas, those of transparent oxide semiconductor diodes can be performed under room light illumination, since they are basically insensitive to visible light. When a source of electric power is connected across a junction, the amount of current flow is influenced by the applied voltage polarity. When the

junction is forward biased, current increases rapidly when the applied voltage exceeds the built-in electric field, but when the junction is reverse biased, the current is very low. This current–voltage performance of *p–n* junctions are utilised for electric current rectification.

The growth of films and physical properties of the *n* and *p*-type transparent conducting layers, sputtered onto quartz substrates were described in Chapter 4 and 5. After several trials the sputtering conditions were optimised so as to obtain good *I-V* characteristics for the *p-n* hetero junctions. The experiment for the fabrication on hetero junctions was carried out as two sets. In the first set the *p*-type material used was copper oxide (CuO) and in the second, copper indium oxide (CIO) was the *p*-type material. The *n*-type material was indium tin oxide (ITO) for both set of experiments. After the growth of *n*-type material on a particular substrate, *p*-type layer was sputtered on to its surface in the required area by masking the film surface using Kapton tapes. Six *p-n* hetero junction diodes were fabricated on a 5x5cm^2 area of the substrate and their *I-V* characteristics studied. The formation of diodes in each set of experiments is explained in the next two sections.

6.3 Transparent *n*-ITO/ *p*-CuO hetero junctions

Bi-layered *n*-ITO/*p*-CuO transparent diode structures were fabricated by plasma vapour deposition using radio frequency (RF) magnetron sputtering. CuO layers were sputter deposited onto pre-sputtered ITO coatings. The *p-n* hetero junction diodes were highly transparent in the visible region and exhibits rectifying *I-V* characteristics with good ideality factor. The substrate temperature and sputter power during fabrication of *p*-layer CuO was found to have a profound influence on *I-V* characteristics.

6.3.1 *I-V* Characteristics

The deposition parameters of the *n*-layer ITO films and *p*-layer CuO films were discussed in previous chapters. The *n*-type ITO generally has a band gap of 3.5 to 4.3 eV and hence highly transparent in visible region. In the UV region, it is

opaque, with a non zero extinction co-efficient *k*, due to band-to-band absorption between conduction and valence band. In IR region also ITO is opaque due to absorption of free charge carriers. For ITO films, the lowest value for resistivity was obtained at a substrate temperature of 100^0C using a power of 200 W. Hence, for the fabrication of hetero junctions, the ITO coating was done by keeping these parameters and all other experimental details followed were similar as discussed earlier.

CuO having a band gap of 1.2-1.5 eV was used as *p*-type material in this hetero junction structure. The hetero junctions were fabricated for *p*-layer sputtered at different RF powers ranging from 60 W to 200 W at substrate temperatures of 100^0C and 200^0C. Based on the measured band gap of CuO and ITO, the energy band diagram for the equilibrium state of the *p-n* hetero junction is plotted as in figure 6.2 using Anderson model. This consideration neglects the vacuum level continuity and the effects of interfacial states and dipoles. The *n*-type and *p*-type materials have different values for electron affinities and their band gaps. This has resulted in higher value for valence band offset (ΔE_v = 2.546 eV) compared to conduction band offset (ΔE_c = 0.9 eV).

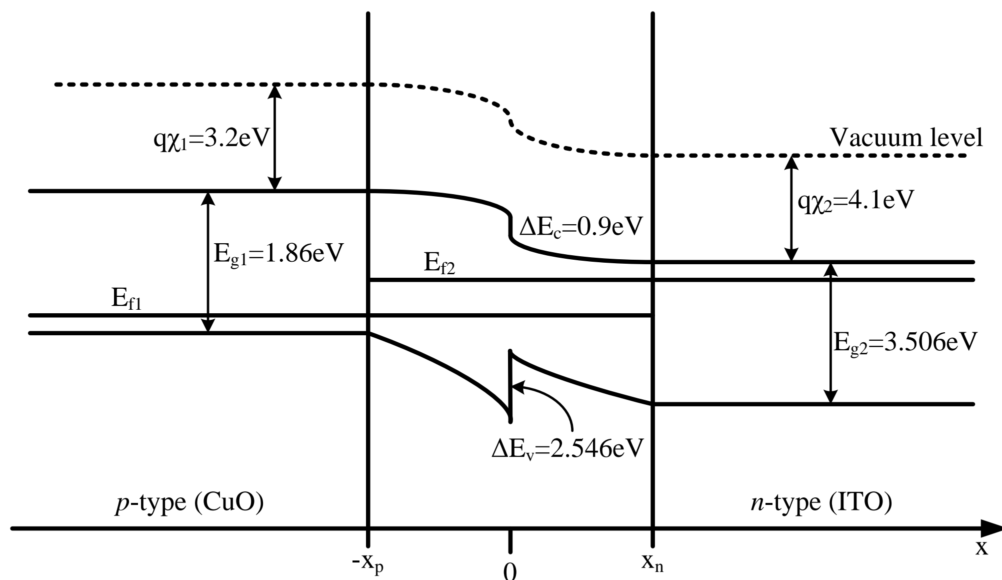

Figure 6.2 Equilibrium energy band diagram of the n-ITO/p-CuO hetero junction diode fabricated by RF sputtering.

The current-voltage plot of the films were obtained using a DC probe station and plotted in figure 6.3. They exhibited good *I-V* characteristics comparable to that of normal diodes and shows that the junction is rectifying. The maximum forward to reverse current ratio is about 60 at 1 V and the turn on voltage varies from 0.34 V to 0.78 V. For diodes with *p*-layer deposited at 60 W, the characteristics obtained were straight line, showing that no diode structure was formed. This may be due to the lack of recombination of holes and electrons at the junction depletion layer due to less concentration of charge carriers. With an increase in sputter power, the films exhibited good *I-V* characteristics with decrease in the turn on voltage as in figure 6.3 (a), (b) and (c). The films deposited at higher substrate temperature showed better diode characteristics as in figure 6.3 (d) and (e).

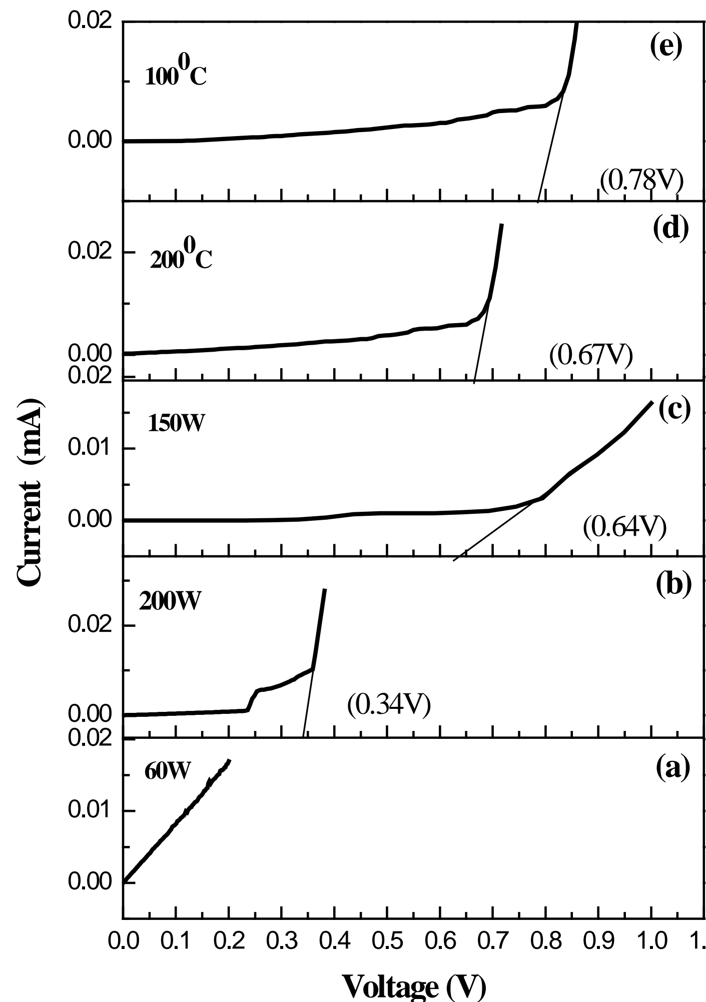

Figure 6.3 Typical current-voltage plots of the ITO/CuO transparent hetero junctions.

6.3.2 Ideality factor

The high value of ideality factor in any *p-n* junction can be attributed to poor interface and defects at the interface. The hetero junction diode can be modelled in different bias ranges by a series of diodes and resistances. The ideality factor of device is the sum of ideality factors of individual junctions and may lead to ideality factor much greater than two. The diode ideality factor was determined from the slope of the forward bias *ln* I vs V graph as in figure 6.4.

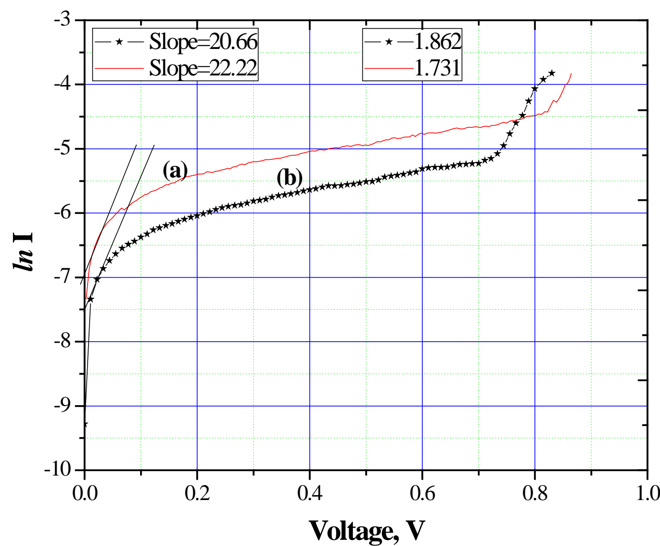

Figure 6.4 ln I vs Voltage graph of the hetero junction diodes with p-CuO layer sputtered at (a) 200 W and 100^{0}C and (b) 150 W and 200^{0}C.

The ideality factor obtained for the hetero junction thin film diodes with *p*-layer sputtered at 200 W and 100^{0}C substrate temperature was 1.731 and that sputtered at 150 W and 200^{0}C was 1.862. The carrier concentration of *n*-type ITO is large (70.92 x10^{18} /cm^3) and hence Fermi level will be closer to conduction band minimum while *p*-type CuO has large hole concentration (of the order of 10^{18} to 10^{21}/cm^3) and hence Fermi level closer to the valence band maximum. As the *p* and *n* materials are brought into contact, a constant Fermi level will be formed at equilibrium. The turn on voltage, is less than 1 V and can be attributed to the existence of large interface defect states. X-ray diffraction studies suggest that both ITO and CuO films are highly oriented.

6.4 Transparent *n*- ITO/ *p*-CIO hetero junctions

The diode structure fabricated was similar to that in figure 6.1, except that in this set of experiments, the *p*-type conducting layer used was copper indium oxide (CIO). In this set also, the RF power and substrate temperature maintained during sputtering of *p*-layer is found to have an influence on the diode characteristics of the hetero junction. Similar to the first set of experiments, RF power was varied in the range 60 W to 200 W and temperature of substrate from 100^0C to 230^0C. The final junctions formed were highly transparent in the visible spectrum and exhibits good rectifying *I-V* plots, characteristic to *p-n* hetero junction diodes.

6.4.1 *I-V* Characteristics

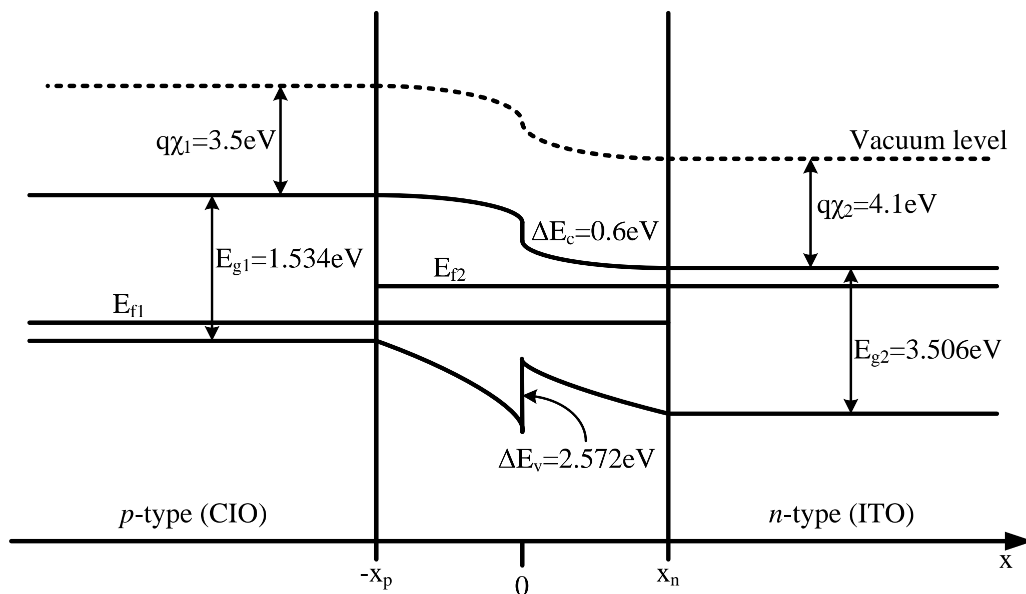

Figure 6.5 Equilibrium energy band diagram of the n-ITO/p-CIO hetero junction diode fabricated by RF sputtering.

The schematic band energy diagram of *n*-ITO/*p*-CIO hetero junction (figure 6.5) was constructed using Anderson model, similar to that explained in the earlier section. In this hetero junction also since the electron affinities and band gaps were dissimilar, the band energy diagram results in higher value for valence band offset (ΔE_v = 2.572 eV) compared to conduction band offset (ΔE_c = 0.6 eV). The maximum forward to reverse current ratio is above 80 at 1 V and the turn on voltage varies from 0.32 V to 0.79 V, depending on the deposition conditions of the *p*-layer. In

this case, even at a low RF power of 60 W, the diodes exhibited rectifying behaviour with a turn on voltage of 0.79 V. Good *I-V* characteristics with an increase in sputter power was obtained and decrease in the turn on voltage was observed as in figure 6.6 (a) and the films deposited at higher substrate temperature showed better diode characteristics as in figure 6.6(b).

From band diagram, it can be observed that majority carrier concentration in the region where the two materials form a junction (depletion region) is small. This is due to the dissimilarity in the Fermi level of the two bands. The turn on voltage, is less than 1 V in all cases and can be attributed to the existence of large interface defect states.

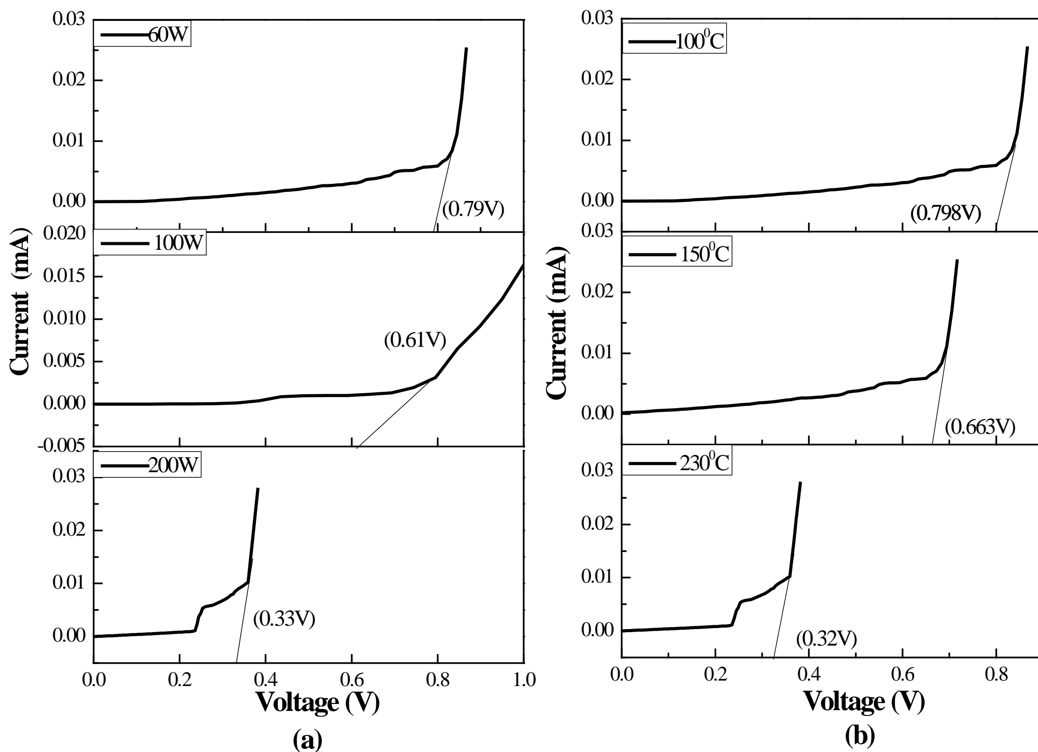

Figure 6.6 Typical current- voltage plots of the ITO/CIO transparent hetero junctions with (a) varying sputter powers and (b) varying substrate temperatures.

6.4.2 Ideality factor

The slope of graph between forward bias *ln* I vs V is used to determine the diode ideality factor as in figure 6.7. Table 6.2 gives the values obtained for ideality

factor and turn on voltage of ITO/CIO hetero junction with varying sputtering parameters during the fabrication of *p*-layer. The Fermi level of *n*-ITO will be close to the conduction band minimum due to high carrier concentration while the Fermi level of *p*-type CIO close to the valence band maximum, since it possess large hole concentration. As these *p* and *n*-type materials are connected, a constant Fermi level is formed at equilibrium. The diodes obtained by sputtering *p*-CIO layer on *n*-ITO layer at various sputter powers with constant substrate temperature 100^0C and various substrate temperatures at a constant sputter power of 150 W are used in this study.

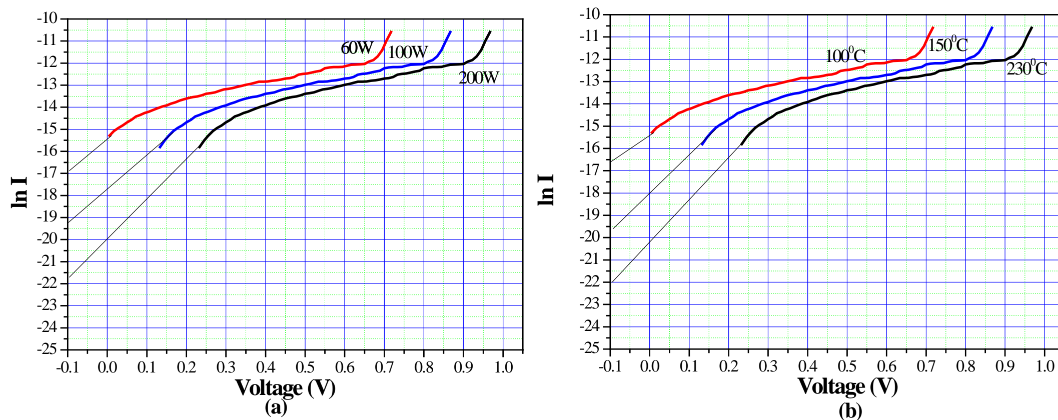

Figure 6.7. ln I Vs Voltage graph of the hetero junction diodes (a) for varying sputter powers and (b) substrate temperatures.

Table 6.1 Electrical property variations of p-n hetero junctions

Sputter Power (W)	Substrate temperature (^{0}C)	Turn on Voltage (V)	Diode Ideality factor
60	100	0.79	1.51
100	100	0.61	1.75
200	100	0.33	1.96
150	100	0.798	1.85
150	150	0.663	2.31
150	230	0.32	3.21

6.5 Conclusion

Transparent and crystalline ITO/CuO and ITO/CIO hetero junctions with average transparency above 60% in visible region were obtained by radio frequency magnetron sputtering. The electrical behaviour of the *p-n* hetero junctions were investigated in detail and the results show that the diodes with CIO as *p*-layer sputtered at RF power of 150 W and substrate temperature of 230^0C has the highest ideality factor of 3.21, which may be due to the presence of interface defect states. Band energy diagrams were used to explain the diode characteristics. The high forward to reverse current ratio confirm the low leakage current in the reverse direction, which suggests good rectifying capability of the diode, making it suitable for potential applications in optoelectronic devices.

References

[1] M. Asif Khan, J. N. Kuznia, D. T. Olson, J. M. Van Hove, M. Blasingame, and L. F. Reitz, Applied Physics Letters, 60 (1992) 2917.

[2] A. Kudo, H. Yanagi, K. Ueda, H. Hosono, H. Kawazoe, and Y. Yano, Applied Physics Letters, 75 (1999) 2851.

[3] R. L. Hoffman, J. F. Wager, M. K. Jayaraj, and J. Tate, Journal of Applied Physics, 90 (2001) 5763.

[4] S. Narushima, H. Mizoguchi, K. Shimizu, K. Ueda, H.Ohta, M. Hirano, T. Kamiya, and H. Hosono, Advanced Materials, 15 (2003) 1409.

[5] H. Ohta, M. Hirano, K. Nakahara, H. Maruta, T. Tanabe, M. Kamiya,, T. Kamiya and H. Hosono, Applied Physics Letters, 83 (2003) 1029.

CHAPTER 7

SUMMARY AND CONCLUSIONS

7.1 Summary and conclusions

Transparent electronics is an emerging research field which has opened up various novel and exciting device applications. Understanding the principles of transparent conductors provides a strong foundation for the search of novel materials and efficient carrier generation mechanisms to make them good conductors.

Currently, most of the TCOs applied in practical uses are of *n*-type. This is mainly because of the ease in doping and flexibility to alter their physical behaviour. Also the concentration of charge carriers in *n*-type materials can be enhanced easily by substitutional doping. But, for device applications the most important requirement is *p*-type TCOs, which are quite scarce in number at present. Hence the challenge is to find more and more materials achieving *p*-type conduction by methods such as doping, which facilitates control of stoichiometry as well as carrier concentration. Various copper delaffosites are known to exhibit *p*-type conduction and further research should be initiated in this area. The main hindrance to this fact is that wide band gap materials are difficult to be doped to *p*-type materials.

This thesis includes two parts: *i)* investigation of processing parameters on electrical, optical, micro structural and structural properties of *n*-type and *p*-type materials in thin film form by radio frequency magnetron sputtering and *ii)* fabrication of transparent *p-n* hetero junctions based on these films and investigation of their structural, optical, morphological and electrical performance appropriate for device applications.

7.1.1 Investigation of processing parameters on electrical, optical, micro structural and structural properties of *n*-type and *p*-type materials

Tin (IV) oxide and tin doped indium oxide (ITO) thin films were chosen as the *n*-type materials for investigation. Copper (II) oxide and copper indium oxide (CIO) were chosen as *p*-type materials for our study. The process parameters for fabrication of these films were explored as a function of substrate temperature and sputter power and optimum fabrication conditions were determined to get good TCO

properties. The main aim was to explore the deposition parameters that contribute to achieve the maximum electrical conductivity and optical transparency in these films. XRD results revealed that films sputtered at higher substrate temperatures results in thin films of comparatively high crystal quality in both *n* and *p*-type materials. The minimum resistivity and maximum optical transmittance was achieved for the films sputtered at higher RF power of above 150 W. The surface roughness and grain size were increased with increasing deposition substrate temperature in all films.

The electrical conductivity and carrier concentration of charge carriers were also found to have significant influence on the sputtering parameters. The thicknesses of the films were increased due to higher deposition rate at higher RF powers. The films obtained had good optical transparency, above 75% in the visible region. Both, crystallinity and electrical conductivity of thin films were improved by increasing sputter power during deposition. However, the optical transmittance was decreased slightly in this case, due to increased film thickness.

Uniformity and homogeneity of films increased with sputter power, as revealed by SEM investigations. This was further confirmed by AFM studies and optical profiler studies. The composition of thin films and purity of samples were confirmed by EDS and XPS studies, which also helped in determining the oxidation state of the constituents. Chapter 4 discusses in detail about the fabrication and properties of *n*-type materials and that of *p*-type materials were discussed in Chapter 5.

7.1.2 Fabrication of transparent *p-n* hetero junctions based on these films and investigation of their physical properties for device applications.

In the second part of the thesis (Chapter 6) transparent bi-layered *p-n* hetero junction diodes were fabricated using the above *p* and *n*-type materials and optimum conditions were determined in order to obtain diodes with high ideality factor. This was done by sputtering one layer over the other by appropriate masking and silver contacts were incorporated to take out leads for electrical characterisations. Two sets of samples were studied - one with copper (II) oxide and another with copper indium oxide as *p*-layer. Results show that the diodes with *p*-layer copper indium oxide exhibit much better characteristics compared to that with *p*-CuO layer. The diodes

having CIO as *p*-layer films sputtered at a maximum RF power of 150 W and substrate temperature of 230^0C has the highest ideality factor of 3.21. The high forward to reverse current ratio suggests low reverse leakage current which ensures good rectifying capability of the diode, making it suitable for potential applications in opto electronic devices [1, 2].

7.2 Scope for future studies

In this work, it has been demonstrated that sputter deposition can be used to fabricate *p-n* hetero junctions having above 70% transparency in visible range. Further study should focus on developing novel *p*-type materials with good conductivity, which is difficult to attain, while retaining good transparency [3, 4]. Sputter conditions should be optimised in order to fabricate them into thin film form. Further these films can be used to fabricate transparent *p-n* hetero junctions and research may be extended further for the fabrication of thin film transistors. Other fabrication methods such as CVD, electron beam evaporation and PLD may also be employed for the fabrication.

Deeper insights into the conductivity mechanisms may be achieved by investigating the intrinsic defect structures of these materials and their band structures. The electrical conductivity of materials can be altered to a large extend by introducing impurities into the crystal structure by doping. According to the "limiting rule for doping" by Zhang et al. [5], *p*-type doping of materials can be achieved if the work function is small and valence band maximum is high. Also, *n*-type doping is favourable if electron affinity is large and positive and the conduction band minimum is low. Hence such materials may be chosen for the fabrication of thin films.

The quest for novel materials as TCOs are based on experimental techniques and can at times be very cumbersome. In order to eliminate the trial and error method and ease the investigations, theoretical methods can be adopted. Ab-initio density functional band structure investigations are important in providing a thorough insight into the TCO basics. It also provides scope for predicting hidden capabilities of materials beyond those employed conventionally [6].

References

[1] D. S. Ginley, Handbook of Transparent conductors (2010) Springer Science.

[2] C. C. Huang, F. H. Wang, C. C. Wu, H. H. Huang and C. F. Yang, Nanoscale Research Letters, 8 (2013) 206.

[3] J. Robertson, P.W. Peacock, M.D. Towler and R. Needs, Thin Solid Films, 411 (2002) 96.

[4] Hosono, H., Ohta, H., Orita, M., Ueda, K. & Hirano, M. Vacuum, 66 (2002) 419.

[5] Sam Zhang, Deen Sun, Yongqing Fu and Hejun Du, Thin Solid Films, 447 (2004) 462.

[6] J. E. Medvedeva and C. L. Hettiarachchi, Physical Review B, 81 (2010) 125116.